

THE DYNAMICS OF COUPLED RESONANT SYSTEMS AND THEIR
APPLICATIONS IN SENSING

A Dissertation

Submitted to the Faculty

of

Purdue University

by

Conor S. Pyles

In Partial Fulfillment of the

Requirements for the Degree

of

Doctor of Philosophy

December 2020

Purdue University

West Lafayette, Indiana

**THE PURDUE UNIVERSITY GRADUATE SCHOOL
STATEMENT OF DISSERTATION APPROVAL**

Dr. Jeffrey F. Rhoads

School of Mechanical Engineering

Dr. Charles M. Krousgrill

School of Mechanical Engineering

Dr. Dana Weinstein

School of Electrical and Computer Engineering

Dr. Nikhil Bajaj

Swanson School of Engineering, University of Pittsburgh

Approved by:

Dr. Nicole L. Key

Associate Head for Graduate Studies, School of Mechanical Engineering

ACKNOWLEDGMENTS

This material is based upon work supported by the National Science Foundation under Grant No. 1537988 and by the National Science Foundation Graduate Research Fellowship Program under grant number DGE-1333468.

TABLE OF CONTENTS

| | Page |
|--|------|
| LIST OF TABLES | vii |
| LIST OF FIGURES | viii |
| ABSTRACT | xiii |
| 1. INTRODUCTION | 1 |
| 1.1 Large Coupled System Dynamics | 1 |
| 1.2 Sensing Applications | 3 |
| 1.3 Coupled Oscillator Networks | 4 |
| 1.4 Outline of This Work | 5 |
| 2. DESIGN OF A SCALABLE ELECTROMECHANICAL ARCHITECTURE FOR A NETWORK OF GLOBALLY COUPLED RESONATORS | 7 |
| 2.1 Motivation | 7 |
| 2.2 Design Overview | 7 |
| 2.3 Coupling Board Design | 9 |
| 2.3.1 Analog Circuitry | 9 |
| 2.3.2 Approximate Dynamic Model | 10 |
| 2.4 Resonator Board Design | 11 |
| 2.4.1 Analog Circuitry | 11 |
| 2.4.2 Approximate Dynamic Model | 12 |
| 2.5 Combined Equations of Motion | 13 |
| 2.6 Digital Circuitry | 14 |
| 2.7 Component Characterization | 14 |
| 2.7.1 Varactor Characterization | 18 |
| 2.7.2 Linearity Study | 18 |
| 2.8 Summary | 20 |
| 3. EXAMINATION OF THE DYNAMICS OF A LARGE COUPLED RESO- NANT SYSTEM WITH PRESCRIBED PARAMETER MISTUNING | 21 |
| 3.1 Introduction | 21 |
| 3.2 Derivation of the Continuum Representation of the System Equations | 21 |
| 3.3 Solution of the Continuum Equations | 22 |
| 3.4 Discrete System Solution | 25 |
| 3.5 Population Density Functions | 26 |
| 3.6 Convergence of the Discrete and Continuous Formulations | 28 |
| 3.7 Results and Discussion | 30 |

| | Page |
|-------|--|
| 3.7.1 | Nearly-Identical System 30 |
| 3.7.2 | Dissipative Coupling 31 |
| 3.7.3 | Constant Population Density 32 |
| 3.7.4 | Quadratic Population Density 38 |
| 3.8 | Conclusions 42 |
| 4. | A SINGLE-INPUT, SINGLE-OUTPUT MULTI-ANALYTE VAPOR SEN- SOR BASED UPON REACTIVELY COUPLED RESONANT ELEMENTS 43 |
| 4.1 | Introduction 43 |
| 4.2 | Methodology 44 |
| 4.2.1 | Electrical Overview 44 |
| 4.2.2 | System Interrogation 48 |
| 4.2.3 | Recovery of the Population Density Function 50 |
| 4.2.4 | Windowing Effects 53 |
| 4.2.5 | Noise Considerations 55 |
| 4.2.6 | Resonator Functionalization 57 |
| 4.2.7 | Experimental Apparatus 57 |
| 4.3 | Results and Discussion 58 |
| 4.3.1 | Resonator Selection 58 |
| 4.3.2 | Thermal Sensitivity 60 |
| 4.3.3 | Non-Thermal Drift 61 |
| 4.3.4 | VOC Exposure Results 62 |
| 4.3.5 | Sensitivity and Regression Model 64 |
| 4.4 | Conclusions 67 |
| 5. | COLOR RECOGNITION VIA A NETWORK OF COUPLED OSCILLATORS 70 |
| 5.1 | Motivation 70 |
| 5.2 | Background 72 |
| 5.2.1 | Colpitts Oscillators 72 |
| 5.3 | Analysis 73 |
| 5.3.1 | Equations of Motion 73 |
| 5.3.2 | Nondimensionalization 75 |
| 5.3.3 | Harmonic Analysis: Single Oscillator 78 |
| 5.3.4 | Limitations of This Model 86 |
| 5.3.5 | Parametric Study 87 |
| 5.3.6 | Variation in C_g 88 |
| 5.3.7 | Conclusions From the Analysis 91 |
| 5.4 | Experimental Methodology 92 |
| 5.4.1 | Design Overview 92 |
| 5.4.2 | Oscillator Board 92 |
| 5.4.3 | Illumination Source 95 |
| 5.4.4 | Component Characterization 95 |

| | Page |
|---|------|
| 5.5 Experimental Results | 100 |
| 5.5.1 Case One: Equally Spaced Oscillators | 100 |
| 5.5.2 Case Two: Asymmetrically-Spaced Oscillators | 103 |
| 5.6 Conclusions | 104 |
| 6. CONCLUSIONS AND RECOMMENDATIONS FOR FUTURE STUDY . | 105 |
| 6.1 Summary | 105 |
| 6.2 On Future Work for Mass Sensing | 105 |
| 6.3 On Future Work for Oscillator-Based Pattern Recognition | 106 |
| REFERENCES | 107 |

LIST OF TABLES

| Table | Page |
|-------|--|
| 2.1 | Extracted parameter values. 16 |
| 2.2 | Best-fit equivalent circuit parameters. 17 |
| 4.1 | Excitation signal parameters. 49 |
| 4.2 | Deviation between the peak of each distribution and the analytical value of each resonance frequency. 53 |
| 4.3 | Resonator groupings by functional material and solvent. Note: Group c was functionalized with 1 μL of single walled carbon nanotubes (SWCNTs) and 1 μL of hydroxylamine hydrochloride (HHC1). 58 |
| 4.4 | A list of the resonators which were retained post-functionalization. These resonators have a sufficiently high quality factor and frequency separation to be observable in the common node spectrum. 60 |
| 4.5 | The equation coefficients and correlation coefficients for the give ink groupings in which the group details can be located in Table 4.3. 66 |
| 5.1 | Nominal values of the circuit parameters shown in Figure 5.1. 74 |
| 5.2 | Nominal values of the nondimensional circuit parameters. Note that the arbitrary parameters ρ and v_j are left undefined. 77 |
| 5.3 | Solution of the system equations with no signal injection at the natural frequency. 84 |

LIST OF FIGURES

| Figure | Page |
|---|------|
| 1.1 A sample device based upon a set of 67 electrostatically coupled micro-cantilevers, which was presented by Buks and Roukes in [3]. © 2002 IEEE | 2 |
| 2.1 Circuit diagram of the system of interest. | 8 |
| 2.2 Physical realization of the coupling board. | 9 |
| 2.3 Physical realization of the resonator array. | 9 |
| 2.4 Coupling control board circuit diagram. | 10 |
| 2.5 Diagram of a single branch of the array board. | 11 |
| 2.6 Diagram of the Butterworth-Van Dyke equivalent circuit. | 12 |
| 2.7 Experimental response used for parasitic characterization. The system was found to resonate at 84.685 MHz. | 17 |
| 2.8 Predicted response for the nearly-identical, reactively coupled system for $N =$ (left) 1, (center) 8, and (right) 16 with the experimental peak locations overlaid with red markers. Each color represents the response at each value of C_c , with C_c decreasing as the distributions shift to the right. Note that the continuum approximation and discrete system response converge for an identical distribution of resonators. | 18 |
| 2.9 Experimentally obtained capacitance of a single varactor as a function of the bias voltage. | 19 |
| 2.10 Gain and frequency shift at resonance versus driving voltage. | 20 |
| 3.1 Population density functions for the constant and quadratic systems. . . . | 28 |
| 3.2 Comparison of the forcing-normalized coupling term for the (solid) discrete and (dashed) continuous solutions for each population density function with $C_c = 154$ pF and $R_c = 0 \Omega$ | 29 |
| 3.3 Experimental frequency response sweeps for a reactively coupled system for $N =$ (left) 1, (center) 8, and (right) 16. Each color represents an overlay of the responses of all of the resonators at varying values of C_c decreasing as the distributions shift to the right. | 31 |

| Figure | Page |
|---|------|
| 3.4 Predicted response from both the continuous and discrete models (which give identical results) with no added mistuning (i.e. C_{di} is shorted) for values of $R_c = 100 \Omega$ and (left) $C_c = 154$ pF and (right) $C_c = 11$ pF. . . . | 32 |
| 3.5 Experimental responses for a system with no added mistuning (i.e. C_{di} is shorted) for values of $R_c = 100 \Omega$ and (left) $C_c = 154$ pF and (right) $C_c = 11$ pF. Each curve represents the response of a single resonator. | 32 |
| 3.6 Predicted response for the continuum solution with a constant population density for values of (left) $C_c = 154$ pF, (center) $C_c = 67.8$ pF, and (right) $C_c = 11$ pF. Each curve represents the response of a single resonator evaluated at the values of x defined by the lumped population density function. | 33 |
| 3.7 Experimentally obtained response for each of the 16 resonators with a constant population density for values of (left) $C_c = 154$ pF, (center) $C_c = 67.8$ pF, and (right) $C_c = 11$ pF. Each curve represents the response of a single resonator. | 34 |
| 3.8 Predicted response for the continuum solution with a constant population density for values of $R_c = 50 \Omega$ and (left) $C_c = 154$ pF, (center) $C_c = 67.8$ pF, and (right) $C_c = 11$ pF. | 36 |
| 3.9 Predicted response for the continuum solution with a constant population density for values of $R_c = 100 \Omega$ and (left) $C_c = 154$ pF, (center) $C_c = 67.8$ pF, and (right) $C_c = 11$ pF. | 36 |
| 3.10 Experimentally obtained response with a constant population density for values of $R_c = 50 \Omega$ and (left) $C_c = 154$ pF, (center) $C_c = 67.8$ pF, and (right) $C_c = 11$ pF. | 37 |
| 3.11 Experimentally obtained response with a constant population density for values of $R_c = 100 \Omega$ and (left) $C_c = 154$ pF, (center) $C_c = 67.8$ pF, and (right) $C_c = 11$ pF. | 37 |
| 3.12 Predicted response for the continuum solution with a quadratic population density for values of (left) $C_c = 154$ pF, (center) $C_c = 67.8$ pF, and (right) $C_c = 11$ pF. | 38 |
| 3.13 Experimentally obtained response for each of the 16 resonators with a quadratic population density for values of (left) $C_c = 154$ pF, (center) $C_c = 67.8$ pF, and (right) $C_c = 11$ pF. | 39 |
| 3.14 Predicted response of the continuum solution with a quadratic population density for values of $R_c = 50 \Omega$ and (left) $C_c = 154$ pF, (center) $C_c = 67.8$ pF, and (right) $C_c = 11$ pF. | 40 |

| Figure | Page |
|---|------|
| 3.15 Predicted response for the continuum solution with a quadratic population density for values of $R_c = 100 \Omega$ and (left) $C_c = 154$ pF, (center) $C_c = 67.8$ pF, and (right) $C_c = 11$ pF. | 40 |
| 3.16 Experimentally obtained response with a quadratic population density for values of $R_c = 50 \Omega$ and (left) $C_c = 154$ pF, (center) $C_c = 67.8$ pF, and (right) $C_c = 11$ pF. | 41 |
| 3.17 Experimentally obtained response with a quadratic population density for values of $R_c = 100 \Omega$ and (left) $C_c = 154$ pF, (center) $C_c = 67.8$ pF, and (right) $C_c = 11$ pF. | 41 |
| 4.1 Circuit diagram showing the layout of the circuit. The dashed boxes separate the components which are on separate circuit boards. | 45 |
| 4.2 Physical realization of the coupling/instrumentation board. The top image shows the coupling/instrumentation board, while the bottom row shows the resonator board with its 4x4 grid of crystal resonators. | 46 |
| 4.3 Diagram showing the Butterworth-Van Dyke equivalent circuit for a crystal resonator. | 46 |
| 4.4 Amplitude spectrum of the excitation signal. The relatively flat, narrow region of high excitation is centered on the carrier frequency (15.995 MHz) and spans a 10 kHz band. | 50 |
| 4.5 Simulated frequency response of the system. The dashed lines show the actual frequencies of the resonators in the simulation. | 51 |
| 4.6 Comparison between peak locations between the deconvolved solution, $Re[\rho(f)]$, the calculated admittance, $\beta(f)$, and the spectral output, $\frac{V_f(f)}{V_0(f)}$ | 54 |
| 4.7 Comparison between varying acquisition periods showing the distortion due to truncating the system response to the input. | 55 |
| 4.8 Layout of the chemical and electrical components of the experimental setup. Solid lines represent gas/vapor connections, and dashed lines represent electrical connections. | 59 |
| 4.9 The change in resonator frequency and temperature over a period of 48 hr. | 61 |
| 4.10 The change in resonator frequency over a period of 48 hr after varying exposure times to the plasma wand. | 63 |
| 4.11 A sample output spectrum showing the distribution of resonator responses in a 10 kHz window. Each of the 7 antiresonances in the amplitude plot (and their associated peaks in the phase plot) correlate to the dynamics of a single resonator affecting the spectral response at the common node. | 64 |

| Figure | Page |
|--|------|
| 4.12 Derived population density function for the measured spectrum shown in Figure 4.11. The red dashed lines indicate the locations of the peaks in frequency. | 65 |
| 4.13 Frequency shift in resonators 1-3 over time. The topmost plot shows the concentration of the analytes in the chamber over the same time period, and the bottom plot shows the drift in the reference channel. The vertical grid lines separate the 20-min periods corresponding to pulses in analyte concentration. | 68 |
| 4.14 Frequency shift in resonators 4-6 over time. The topmost plot shows the concentration of the analytes in the chamber over the same time period, and the bottom plot shows the drift in the reference channel. The vertical grid lines separate the 20-min periods corresponding to pulses in analyte concentration. | 69 |
| 5.1 Circuit diagram for a single Colpitts oscillator. | 72 |
| 5.2 Magnitude of the inverse of the transfer function $G(s)$. Normalized by the magnitude at the fundamental frequency. | 81 |
| 5.3 Comparison in the time domain between the model solution and an experimentally measured response. | 85 |
| 5.4 Change in the locking range and steady-state solution values with variation in v_j | 88 |
| 5.5 Change in the locking range and steady-state solution values with variation in C_g | 89 |
| 5.6 Change in the locking range and steady-state solution values with variation in ρ | 90 |
| 5.7 Change in the locking range and steady-state solution values with variation in quality factor. | 91 |
| 5.8 High-level diagram of the experimental setup. | 93 |
| 5.9 Diagram of the oscillator board layout showing the geometry, oscillator/photocell locations, and filter locations. Each oscillator (labeled R, G, and B after their associated color filter) consists of a single Colpitts oscillator of the type described in Section 4.2.1. | 94 |
| 5.10 Diagram illustrating the frequency separation between the two versions of the system examined in this work. | 94 |
| 5.11 Diagram showing the measured irradiance on each photocell for each combination of light and filter color. | 96 |

| Figure | Page |
|--|------|
| 5.12 Diagram of a CdSe photocell. | 97 |
| 5.13 Equivalent Circuit of a CdSe photocell. | 97 |
| 5.14 Experimental characterization of the photocell with 625 nm light using the model given by Figure 5.13. (Upper-Left) Effective series resistance. (Upper-Right) Effective series inductance. (Lower-Left) Effective shunt capacitance. (Lower-Right) Mean squared error between the best fit of the model and the measured impedance of the photocell. | 99 |
| 5.15 Experimental characterization of the frequency shift in a varactor-mistuned Colpitts oscillator. | 101 |
| 5.16 Comparison of four identifiable locking states under various illumination conditions. These spectra were measured at [R,G,B] power coordinates, in Wm^{-2} , of: (Upper-Left) [0, 0, 0], (Upper-Right) [0, 6, 60], (Lower-Left) [1.4, 1, 0], and (Lower-Right) [1.4, 6, 60]. | 102 |
| 5.17 State map for a system with the oscillators spaced approximately evenly in frequency. | 103 |
| 5.18 State map for a system with the red- and green-linked oscillators close in frequency. | 104 |

ABSTRACT

Pyles, Conor S. Ph.D., Purdue University, December 2020. The Dynamics of Coupled Resonant Systems and Their Applications in Sensing. Major Professor: Jeffrey F. Rhoads, School of Mechanical Engineering.

The field of coupled resonant systems is a rich research area with enumerable real-world applications, including the fields of neural computing and pattern recognition, energy harvesting, and even modeling the behavior of certain types of biological systems. This work is primarily focused on the study of the behaviors of two subsets of this field: large networks of globally coupled resonators (which, in this work, refers to passive, damped resonant elements which require external stimulus) and smaller networks of oscillators (referring to active devices capable of self-sustained motion), which are coupled through a network of light-sensitive resistive elements. In the case of the former, we begin by developing an analytical and experimental framework to examine the behaviors of this system under various conditions, such as different coupling modalities and element-level parametric mistunings. Once a proper understanding of the dynamics of these systems has been established, we go on to develop the system into a single-input, single-output, multi-analyte volatile organic compound sensor. For the study of oscillator networks, we begin by building a device which utilizes a network of Colpitts oscillators, coupled through a series of color-filtered CdSe photocells. We then establish that through the analysis of particular emergent behaviors (most notably, frequency locking within the network), this type of system may show promise as a threshold color sensor. By exploiting these behaviors, this type of system may find applications in neuromorphic computing (particularly in optical pattern recognition).

1. INTRODUCTION

With advances in micro- and nano-scale fabrication processes providing for scalable, low-power, and high quality platforms, research interest in resonant systems has increased significantly over the past several decades. Because of this, these types of devices have found extensive use in the scientific, industrial, and commercial sectors in numerous applications, such as signal processing [1–9], energy harvesting [10–13], resonant mass sensing [14–19], and many others [20–29].

While single-degree-of-freedom systems alone have proven to be quite versatile in their application space, the massive parallelization afforded by modern micro-fabrication processes has accelerated research into resonant systems with significantly higher degrees-of-freedom. In particular, the exploitation of emergent behaviors in *coupled* resonant systems has significant potential, offering benefits such as element-level redundancy and potentially overcoming the throughput limitations imposed by the simple parallelization of discrete devices. In this work, we largely focus on two embodiments of this research: the study of large, coupled networks of resonators, with an emphasis on resonant mass sensing applications, and the study of the behaviors of coupled oscillator networks, with an emphasis on applications in neuromorphic computing. While the terms “resonator” and “oscillator” are often used interchangeably in many contexts, within this work it should be noted that the term “resonator” refers to passive, damped devices that require external stimulation and “oscillator” refers to active devices capable of self-sustained motion.

1.1 Large Coupled System Dynamics

While a great deal of research has been dedicated to examining the dynamics of smaller systems [30], of particular interest to this work are the emergent behaviors

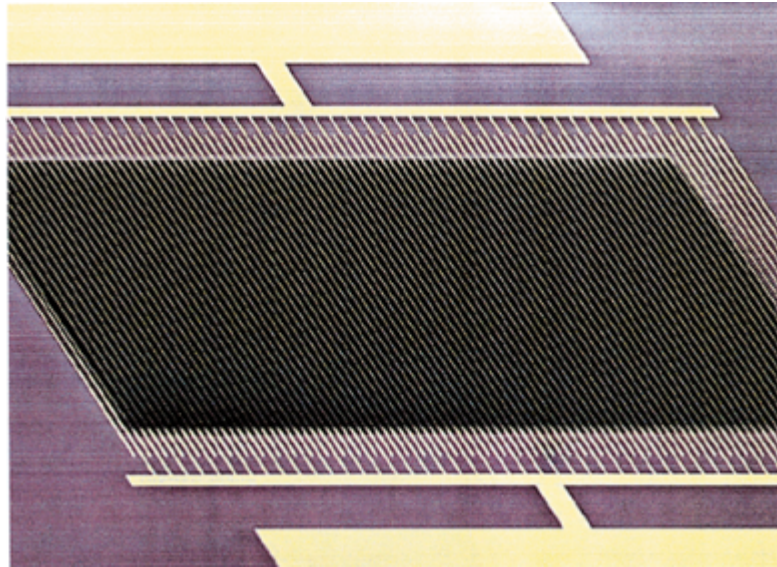


Figure 1.1. A sample device based upon a set of 67 electrostatically coupled microcantilevers, which was presented by Buks and Roukes in [3]. © 2002 IEEE

which are prevalent in larger, more complex coupled systems, such as localization and synchronization. These behaviors have been well documented and utilized in a variety of contexts [3, 31–36], and exploiting these emergent dynamics may have a number of attractive qualities, such as element-level redundancy, or, in the context of sensing devices, increased measurement throughput [14]. Much of the prior work related to these types of systems comes from research on the dynamics of micro- and nano-electromechanical systems (MEMS/NEMS). Among the earlier experimental works in this field was the work of Buks and Roukes in 2002 [3]. In this work, the authors examined the dynamics a system of 67 coupled microbeam resonators and discussed the potential of the system to be used for the spectral analysis of electrical signals. An image of their device is shown in Figure 1.1. Since then, a variety of works have been published examining systems featuring nonlinear dynamics [37, 38], nearest-neighbor [2, 5, 33] and global [39] coupling schemes, systems with element-level mistunings [6, 40], as well as a number of analytical tools designed to facilitate the analysis of these systems [41, 42].

Of particular relevance to this work is the notion of introducing intentional, controlled parametric mistunings into a medium- to large-scale coupled system and exploring the resulting emergent dynamics in the system's response. Prior works have demonstrated that such mistunings may give rise to complex behaviors such as spatially localized modes of motion [6, 43]. Unfortunately, analytically modeling these behaviors in many applications can be a non-trivial task, particularly if the system contains significant nonlinear elements. These systems are often analyzed via reduction to phase-only models, or, if doing so is not possible, perturbation analysis of the system equations [44, 45] or direct numerical simulation. A somewhat more tractable method is to approximate the discrete, high degree-of-freedom system as a continuum of resonators, resulting in a single integro-differential equation representing the system dynamics [41, 42]. In this work, we will utilize the latter method to examine the response of such a system (albeit in a linear context), and demonstrate how the response can be manipulated by varying certain global properties of the system.

1.2 Sensing Applications

Resonant systems have also been used extensively in sensing applications, both as threshold sensors [15, 16, 26, 46, 47] and for true analog measurements [14, 17, 23, 24, 48, 49]. In the case of the former, one technique is to construct a system which exhibits bistability and drive it into a regime near a bifurcation point in which a particular perturbation will trigger a transition between states. The advantage to such a device is that this transition is often easily observable, i.e. by a rapid change in amplitude in the case of a Duffing-like resonator, and the system can be configured to require an exceedingly small perturbation. Because of this, these types of devices are typically used in applications which require a very high sensitivity, such as resonant mass sensors [15, 16, 46, 50]. The downside to this technique, however, is that this type of sensor typically offers a binary output and cannot offer accurate information beyond the crossing of the aforementioned threshold.

Devices which offer analog outputs typically do so by measuring changes in vibration amplitude [51] or frequency [52], with the latter being more common for MEMS-based resonant mass sensors due to the device sensitivity scaling with size and frequency. These types of mass sensors are frequently used in bio-sensing applications [53–57] and chemical analyte detection [58–62]. One method of approach for these systems is to deposit some amount of a chemically selective sorbent on the surface of an electromechanical resonator and measuring the change in its frequency response as the analyte interacts with surface. Unfortunately, such methods tend to lack selectivity; the device can usually only detect the presence of a class of chemicals collectively, rather than differentiating between individual analytes. A solution to this problem can be found by having multiple devices operating in parallel; however, doing so can quickly become a problem of throughput (i.e. how many devices can realistically be measured simultaneously?). By exploiting certain emergent behaviors in a system of coupled resonators; however, it may become possible to measure multiple devices simultaneously via a single measurement point. An example of this was reported in [14], in which the authors demonstrate a set of four micro-cantilevers coupled through a common shuttle mass. Each cantilever was chemically functionalized to adsorb methanol or toluene vapor to varying degrees, shifting the frequencies of the localized modes as mass is added. The authors were able to demonstrate the detection of both vapors from single-point measurements of the motion of a common shuttle mass.

1.3 Coupled Oscillator Networks

In addition to coupled resonant systems, networks of coupled oscillators have also been the subject of considerable contemporary study. Of particular interest to this work are the tendencies in these types of networks for the individual elements to interact via frequency pulling and phase locking [63–66]. A number of models exist which describe these behaviors under various conditions, with some notable models

being the Adler equation [67, 68], which models the phase response of the oscillator to weak external forcing, and the Kuramoto model [69], which models the phase-only dynamics of large ensembles of coupled oscillators.

The interactions between individual oscillators within a network can be made to emulate the behavior of neurons in neuromorphic computing applications [70, 71]. A relatively early work in this subject area was presented by Hoppensteadt and Izhikevich in 2001 [72], in which they discuss the use of phase-synchronization in MEMS oscillators to create associative memory circuits. Since then, the field has expanded to include works such as those by Nikonov et al. [73, 74] which incorporate these types of systems into pattern recognition and image filtering applications. Advancements in materials science and MEMS/NEMS technologies have also helped to drive the development of this field, allowing for lower profile devices which may begin to rival digitally emulated neural networks in terms of power consumption and speed [75–78].

1.4 Outline of This Work

With this work, we seek to expand the application space of coupled resonant systems, with particular emphasis on exploiting the emergent dynamics within these systems to overcome some of the limitations found in traditional sensing applications. To that end, we will begin in Chapter 2 with the development of a modular experimental platform consisting of an array of globally coupled crystal resonators. This system is designed to support reconfigurable reactive and dissipative coupling, and to facilitate element-level mistuning and measurement. This platform is intended to serve as a basis for subsequent chapters to study and utilize the emergent dynamics within the system. In Chapter 3, the dynamics of this type of system are examined in detail, particularly with regards to configurations involving non-uniform element-level mistuning.

In Chapter 4, the culmination of the work described in Chapters 2 and 3 is presented, which utilizes a variant of the platform described in Chapter 2 to provide

a multi-analyte resonant mass sensing platform. This platform essentially amounts to an “artificial nose” which is capable of distinguishing between multiple chemical analytes simultaneously, overcoming one of the principle limitations of traditional resonant mass-based volatile organic compound detection. Additionally, the dynamics caused by the coupling configuration allow the state of multiple resonant elements within the system to be measured via a single output measurement, overcoming the throughput problem presented by simple parallelization of multiple isolated sensors.

In Chapter 5, we shift focus from the study of resonator arrays and VOC sensing to the study of coupled oscillator networks. In particular, a system of 3 coupled, mistuned Colpitts oscillators is examined in which the strength of the coupling paths is controlled by the color content of incident light. This system exhibits features such as strong nonlinear terms and amplitude dynamics which make traditional analysis difficult and necessitate a more empirical approach. By measuring the spectral content at a single node, the frequency locking dynamics in the network can be observed. Because this locking state is determined primarily by the strength of the coupling, this allows the system to act as a single-output, threshold color sensor.

2. DESIGN OF A SCALABLE ELECTROMECHANICAL ARCHITECTURE FOR A NETWORK OF GLOBALLY COUPLED RESONATORS

2.1 Motivation

In this chapter we develop an analytical and experimental framework to examine the behaviors of an array of 16 mistuned electromechanical crystal resonators linked via reactive and dissipative global coupling elements. This framework is designed to be easily expandable to larger arrays and is amiable to the introduction of more complex behaviors, such as element-level nonlinearities and more complex coupling modalities. Once this framework is established, we then proceed to identify key behaviors in the system, such as variations in effective quality factor and the emergence of additional resonances and antiresonances at both the element and system-wide levels. These behaviors are shown to be generated by the global properties of the system, such as the strength and type of coupling, as well as the precise nature of the mistuning across the distribution of resonators. In future works, this type of system will be evaluated for use in practical applications, such as sensing and energy harvesting. For example, given that these global behaviors are sensitive to properties such as the pattern of mistuning across the array of resonators, it may be worthwhile to construct devices in which these mistunings respond to some external factor with varying sensitivities for the individual resonators. Such a device could potentially have a number of attractive qualities, such as element-level redundancy or increased throughput, if these changes can be detected by examining changes in the global behavior of the system [14].

2.2 Design Overview

Figure 2.1 shows an overview of the system of interest, which consists of a parallel array of 16 thickness-shear mode quartz resonators coupled through an adjustable

capacitive element C_c and resistive element R_c . Because the selected resonators are nominally identical, additional adjustable capacitances are also included in series with each resonator branch to facilitate reconfigurable element-level detuning. Additional parasitic elements C_{0p} and L_{0p} are included in order to model the effects of the shunt capacitance across the resonator network and the inductance of the input line and coupling circuit.

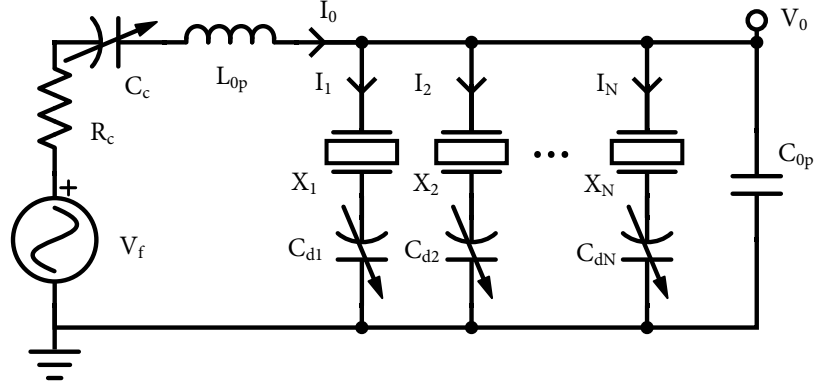


Figure 2.1. Circuit diagram of the system of interest.

The physical implementation of this system consists of two circuit boards: one which generates the forcing voltage and includes the coupling elements, and another which consists of the resonator array and the hardware necessary to measure the current passing through each resonator branch. These two boards connect electrically via a set of standard pin headers, and can essentially be “stacked” together. The system was designed to be modular, allowing additional resonator modules to be added in parallel to expand the array further, if desired. Figures 2.2 and 2.3 show the physical realizations of these designs.

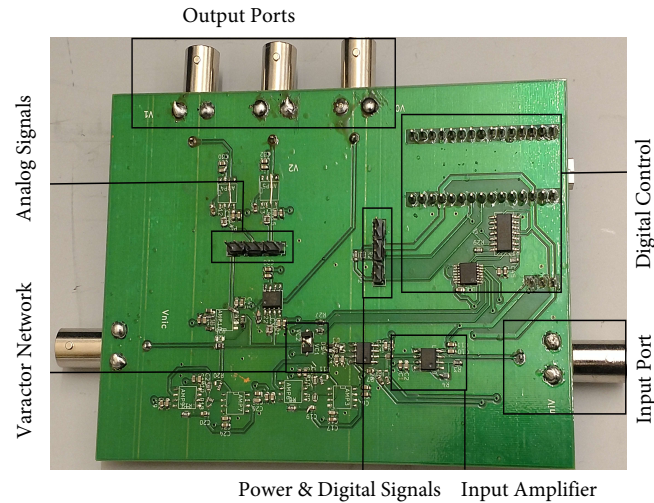


Figure 2.2. Physical realization of the coupling board.

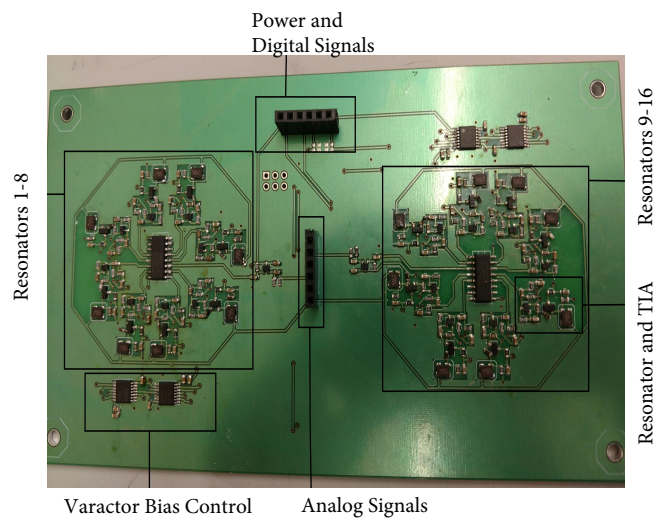


Figure 2.3. Physical realization of the resonator array.

2.3 Coupling Board Design

2.3.1 Analog Circuitry

Figure 2.4 shows a high-level diagram of the analog circuitry for the coupling board. The board consists of an input port which connects the output of the lock-in

amplifier to an op-amp based inverting amplifier. The amplifier then takes the place of an AC voltage source to drive the resonator network. The generated signal then passes through a network of varactor pairs, which provide a variable capacitance to serve as the reactive coupling element, and finally through a resistor to serve as a dissipative coupling element before being passed to the resonator board via a pin header.

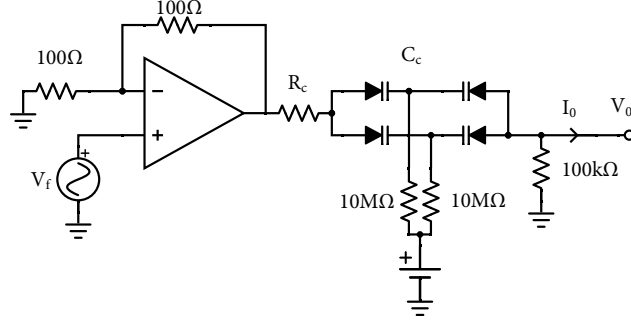


Figure 2.4. Coupling control board circuit diagram.

A lock-in amplifier was used both to generate the input voltage and measure the response of the system. To ensure that the crystals were operated under their maximum drive level of $100 \mu\text{W}$, the input voltage was set to $10 \text{ mV}_{\text{pp}}$. Assuming the nominal value of 80Ω for the series resistance for the crystals, this would give a peak power of $1.25 \mu\text{W}$ if driving a single resonator.

2.3.2 Approximate Dynamic Model

Assuming the op-amp dynamics are close to ideal (which is valid based on the specifications for the LMH6609 used in this work), and that the pull-down resistances are large enough that their dynamics may be neglected, the equations of motion for the analog components of the coupling board are given by:

$$2\dot{V}_f - \dot{V}_0 = R_c \dot{I}_0 + \frac{1}{C_c} I_0. \quad (2.1)$$

Because of the physical size of the common node, it is necessary to include additional parasitic elements caused by the line inductance and shunt capacitance of the trace. Incorporating these dynamics into Equation 2.1 gives the full equations of motion for the coupling board:

$$2\dot{V}_f - \dot{V}_0 = \frac{C_{0p}}{C_c}\ddot{V}_0 + \frac{C_{0p}}{C_c}\dot{V}_0 + R_c\dot{I}_0 + \frac{1}{C_c}I_0. \quad (2.2)$$

2.4 Resonator Board Design

2.4.1 Analog Circuitry

The resonator board receives the common-node excitation from the coupling board, which drives a set of up to 16 resonator branches, though the modular nature of the design allows this to be expanded to an arbitrary number by adding more resonator boards to the stack at the cost of increasing the power required from the input and parasitic parameters. Each branch consists of a single crystal resonator, a series varactor pair for detuning the crystal, and a bipolar-transistor based transimpedance amplifier with a gain of 100Ω . The transimpedance amplifier measures the response of each resonator branch by converting the branch current into a measurable voltage. The output of the amplifiers are connected to one of two 8-channel analog multiplexers which connect the chosen channel to a non-inverting amplifier with a gain of 2. Figure 2.5 shows the circuit diagram for a single resonator branch.

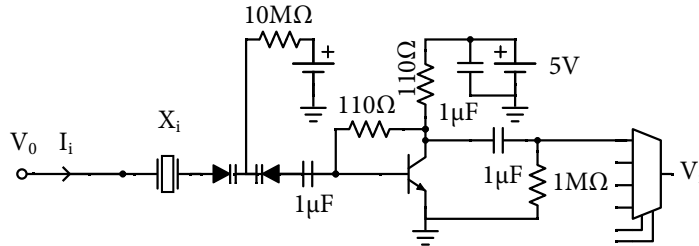


Figure 2.5. Diagram of a single branch of the array board.

2.4.2 Approximate Dynamic Model

A standard model for the dynamics of a piezoelectric crystal is the Butterworth-Van Dyke equivalent circuit, shown in Figure 2.6. This circuit consists of a “motional” branch with a series-RLC circuit in parallel with a shunt capacitance. This model results in two notable frequency-domain characteristics: a typical RLC resonance caused by the motional branch, followed by an antiresonance at a higher frequency which shifts upward to infinity as the shunt capacitance is decreased to zero. For the crystals in this work, the antiresonance frequency was measured to be approximately 18 kHz higher than the resonance. Because this work is focused on the system dynamics in an approximately 6 kHz window near the resonance frequency, and because the dynamics of the shunt capacitance only become significant well outside this band, it was determined that they could be neglected entirely, and it is therefore assumed throughout the remainder of this work that $C_0 \approx 0$.

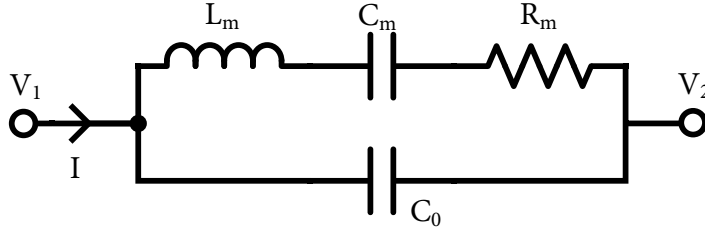


Figure 2.6. Diagram of the Butterworth-Van Dyke equivalent circuit.

Based on this model, the equation of motion for a single crystal is given by:

$$\dot{V} = L_m \ddot{I} + R_m \dot{I} + \frac{1}{C_m} I. \quad (2.3)$$

The crystals used in this work were considered to be nominally identical, however intentional mistuning can be introduced by adding an additional capacitance C_d in series with the crystal. This has the effect of directly adding stiffness to the RLC-equivalent circuit:

$$\dot{V} = L_m \ddot{I} + R_m \dot{I} + \left(\frac{1}{C_m} + \frac{1}{C_d} \right) I. \quad (2.4)$$

Because the resonator board consists of an array of these crystal branches connected in parallel from the common node to ground, we denote the current through each branch i by I_i , the detuning capacitance by C_{di} , and relate each branch's equations of motion to the variables at the common node by:

$$\dot{V}_0 = L_m \ddot{I}_i + R_m \dot{I}_i + \left(\frac{1}{C_m} + \frac{1}{C_d} \right) I_i. \quad (2.5)$$

2.5 Combined Equations of Motion

Combining the circuit equations given by Equations 2.2 and 2.5 yields the full equations of motion for the system:

$$\begin{aligned} \dot{V}_f = & \left(1 + \frac{C_{0p}}{C_c} \right) \left[L_m \ddot{I}_i + R_m \dot{I}_i + \left(\frac{1}{C_m} + \frac{1}{C_{di}} \right) I_i \right] \\ & + R_c C_{0p} \left[L_m \ddot{I}_i + R_m \dot{I}_i + \left(\frac{1}{C_m} + \frac{1}{C_{di}} \right) \dot{I}_i \right] \\ & + L_{0p} C_{0p} \left[L_m I_i^{iv} + R_m \ddot{I}_i + \left(\frac{1}{C_m} + \frac{1}{C_{di}} \right) \dot{I}_i \right] \\ & + \frac{1}{C_c} \sum_{j=1}^N I_j + R_c \sum_{j=1}^N \dot{I}_j + L_{0p} \sum_{j=1}^N \ddot{I}_j. \end{aligned} \quad (2.6)$$

Due largely to the parasitic elements present in the circuit, the system equations are significantly more complex than a typical set of coupled second-order systems, including features such as third- and fourth-order dynamics; reactive, dissipative, and inductive coupling terms; as well as terms which attenuate the normal second-order response of the resonators as the coupling strength is increased. The exact effects of these features will be discussed in the next chapter.

2.6 Digital Circuitry

The digital components of the system consist of an Arduino Nano mounted on the coupling board, which controls (via I²C) a set of five 12-bit, 4-channel digital-analog converters (DACs). Four of these DACs are mounted to the resonator board (connected to the I²C bus on the Arduino via pin header) to control the DC-bias on the detuning varactors, while the fifth is mounted to the coupling board and controls the coupling varactors. The output of each DAC channel is fed through a large resistor to the common cathode of each diode pair.

2.7 Component Characterization

In order to facilitate a proper comparison between the model and experimental results, the values of the unknown circuit parameters must be obtained. For the purposes of this section, the detuning capacitances and coupling resistance R_c were bypassed, leaving an array of nearly-identical reactively coupled resonators. The characterization of the resulting system was performed by comparing the relationship between peak amplitude and resonant frequencies for varying values of C_c and N and performing a linear least-squares fit to determine the values of the unknown parameters. First, it will be shown that for this model, the peak amplitude for the resonators may be expressed exclusively as a function of the array size N , detuned resonant frequency ω_r , and the unknown circuit parameters. We begin with Equation 2.6 in the Laplace domain, substituting the definition of $\alpha(s)$ below for simplicity, setting $R_c = 0$, and simplifying the coupling terms by assuming that the resonators' responses are identical. The latter approximation is valid because the chosen resonators are well matched, which will later be verified in Chapter 3 by the experimental results for the nearly-identical system shown in Figure 3.3. It should also be noted that this fit will be valid for both the discrete and continuous models, as the two yield identical results in a system with well-matched resonators. The simplified equations of motion are given by:

$$sV_f(s) = \alpha(s) \left[L_m I(s) s^2 + R_m I(s) s + \frac{1}{C_m} I(s) \right] + \frac{N}{C_c} I(s) + N L_{0p} I(s) s^2, \quad (2.7)$$

where

$$\alpha(s) = 1 + \frac{C_{0p}}{C_c} + C_{0p} R_c s + L_{0p} C_{0p} s^2. \quad (2.8)$$

Solving for $I(s)$ gives:

$$I(s) = \frac{\frac{s}{\alpha(s)} V_f(s)}{\left[L_m + \frac{N L_{0p}}{\alpha(s)} \right] s^2 + R_m s + \frac{1}{C_m} + \frac{N}{\alpha(s) C_c}}. \quad (2.9)$$

Because the resonators used in this system are very weakly damped ($Q \approx 1.01 \times 10^5$), the peak frequency and natural resonance frequency are nearly equal (an estimated difference on the order of 10^{-4} Hz). Therefore, it is valid to consider them equal for the purposes of this section. By inspection, the system will resonate at an angular frequency of:

$$\omega_r^2 = \frac{\frac{1}{C_m} + \frac{N}{C_c \alpha(s)}}{L_m + \frac{L_{0p} N}{\alpha(s)}}, \quad (2.10)$$

and will have a peak amplitude of:

$$I_p = \frac{V_f}{\alpha(s) R_m}. \quad (2.11)$$

Combining these results with Equation 2.8 and setting $s^2 = -\omega_r^2$ to eliminate C_c and $\alpha(s)$ gives the peak amplitude as a function of ω_r and N :

$$\frac{I_p}{V_f} = \frac{1}{R_m} + \frac{C_{0p}}{C_m R_m} \frac{1}{N} - \frac{C_{0p} L_m \omega_r^2}{R_m N}. \quad (2.12)$$

Given a 2-dimensional data set of peak amplitude versus resonant frequency and N , the parameters $\frac{1}{R_m}$, $\frac{C_{0p}}{C_m R_m}$, and $\frac{C_{0p} L_m}{R_m}$ may be estimated by solving the resulting 3-term linear least-squares problem. In order to generate the required data for the fit, the value of C_c was varied across its full range of values for three different

circuit configurations which contained of 1, 8, and 16 resonator branches, respectively. The resulting amplitudes and resonant frequencies were then recorded and the least-squares problem was solved to give the parameter values shown in Table 2.1.

Table 2.1. Extracted parameter values.

| Parameter | Value |
|--------------------------|---|
| $\frac{1}{R_m}$ | $0.01343 \Omega^{-1}$ |
| $\frac{C_{0p}}{C_m R_m}$ | $463.1 \Omega^{-1}$ |
| $\frac{C_{0p} L_m}{R_m}$ | $4.583 \times 10^{-14} \text{ s}^2 \Omega^{-1}$ |

The value of $L_{0p}C_{0p}$ was obtained by disconnecting the resonators from the board and measuring the resonance frequency of the resulting RLC system. Figure 2.7 shows the voltage of the system measured at a midpoint along the coupling line. As can be seen, the system resonates at a frequency of 84.685 MHz. Additionally, a second-order zero is visible at 124.62 MHz, which is a consequence of measuring the response midway along the parasitic inductance. From the resonance frequency, it can be determined that the value of $L_{0p}C_{0p} = \frac{1}{\omega_r^2} = 3.5321 \times 10^{-18} \text{ s}^2$.

In order to find the values of the circuit parameters, we use the three parameters obtained from the fit, the value of $L_{0p}C_{0p}$, and an additional constraint on the uncoupled quality factor of the resonators (which was measured from the crystals' uncoupled responses on a separate board to be 1.017×10^5). This set of equations was then solved, yielding the parameter set shown in Table 2.

While the parameters L_m and C_m are generally not given in the datasheet for the crystals, the calculated value of R_m very nearly matches the rated value of 80Ω . Figure 2.8 shows the predicted frequency response of the model for a system of nominally identical resonators for varying values of C_c ranging from 154 pF to 11 pF with the experimentally obtained peaks overlaid with red markers. Note that while the trends in peak amplitude versus frequency are very well matched in every case, the

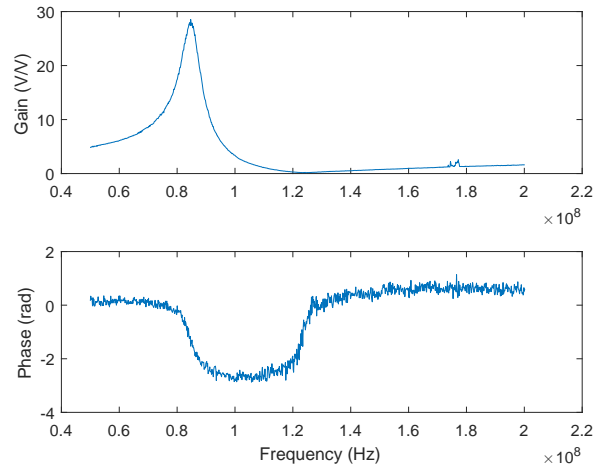


Figure 2.7. Experimental response used for parasitic characterization. The system was found to resonate at 84.685 MHz.

Table 2.2. Best-fit equivalent circuit parameters.

| Parameter | Value |
|-----------|----------------|
| L_m | 75.312 mH |
| R_m | 74.44 Ω |
| C_m | 1.3140 fF |
| C_{0p} | 45.30 pF |
| L_{0p} | 77.98 nH |

experimental measurements showed a more significant degree of mistuning in response to increased coupling. This may be caused by the impedance of the physical resonators diverging from that of the assumed Butterworth-Van Dyke equivalent circuit at off-resonance frequencies, which becomes more visible as the capacitive mistuning is increased. For additional comparison, Figure 3.3 shows the full experimental response at the same values of C_c . These results will be discussed in more detail in the next section.

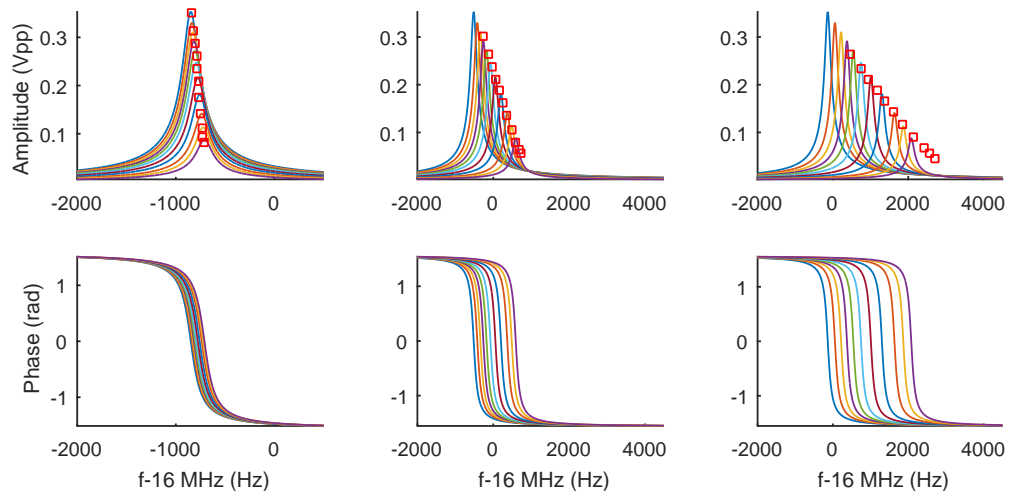


Figure 2.8. Predicted response for the nearly-identical, reactively coupled system for $N =$ (left) 1, (center) 8, and (right) 16 with the experimental peak locations overlaid with red markers. Each color represents the response at each value of C_c , with C_c decreasing as the distributions shift to the right. Note that the continuum approximation and discrete system response converge for an identical distribution of resonators.

2.7.1 Varactor Characterization

In order to generate predictable capacitance values using the varactors, it was necessary to characterize their capacitance vs. DC bias curves experimentally. This was done offline using a precision LCR meter and DC voltage source. Figure 2.9 shows the results of this characterization.

2.7.2 Linearity Study

Because the model assumes that the crystals will have linear responses, it is necessary to quantify an acceptable operating range for the driving voltage which will avoid nonlinear behavior. For the linear models previously derived, the gain and resonant frequencies of the response should remain constant with variations in the

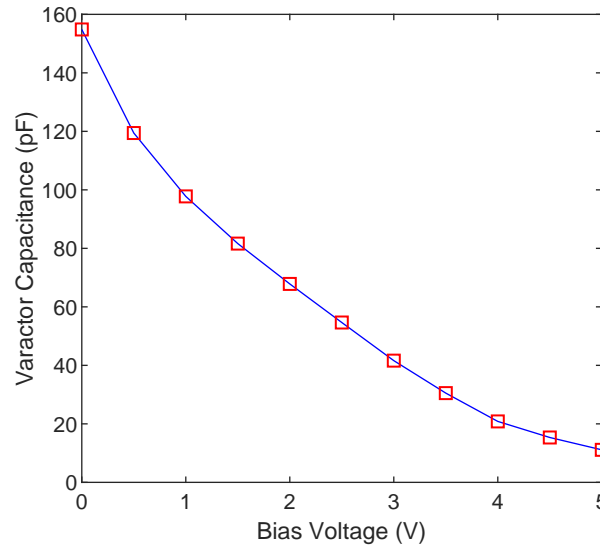


Figure 2.9. Experimentally obtained capacitance of a single varactor as a function of the bias voltage.

driving voltage. Thus, one way to identify the onset of nonlinear behavior is by observing the shift in these values as the driving voltage increases. Figure 2.10 shows the gain and frequency shift versus input voltage. The nonlinearity in the crystals was found to become significant after approximately $120 \text{ mV}_{\text{pp}}$, which corresponds to a decline of approximately 2% in gain and a shift of approximately 4 Hz in resonant frequency. After this point, both the gain and resonant frequency begin to shift in an approximately linear fashion with the driving voltage. With this in mind, an input amplitude of $10 \text{ mV}_{\text{pp}}$ was used in the characterization experiments to ensure linear behavior.

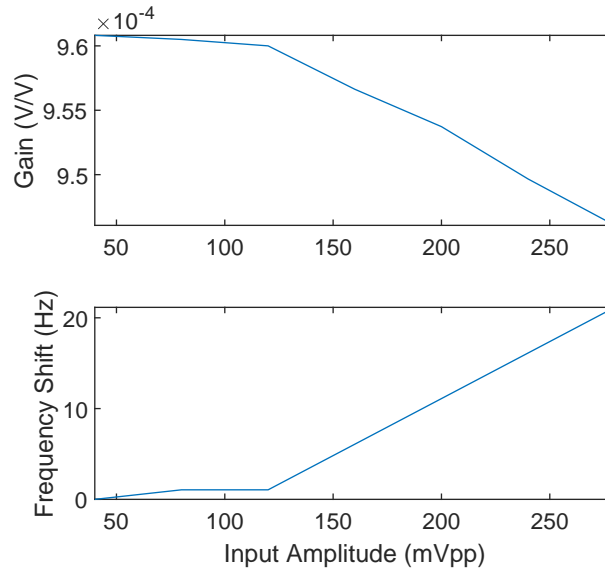


Figure 2.10. Gain and frequency shift at resonance versus driving voltage.

2.8 Summary

In this chapter, an experimental platform consisting of a set of 16 coupled crystal resonators was designed and characterized experimentally. The system was built to be easily reconfigurable at the element-level, and has a modular design allowing it to be expanded to a larger network as desired. Reconfigurable mistuning, as well as coupling, was facilitated by means of a network of varactor diodes, the biases of which were controlled using a set of onboard digital-to-analog converters controlled via a common I²C bus. In the next chapter, the dynamics will be examined analytically, and this analytical model will be validated against experimental measurements for varying configurations of this system.

3. EXAMINATION OF THE DYNAMICS OF A LARGE COUPLED RESONANT SYSTEM WITH PRESCRIBED PARAMETER MISTUNING

3.1 Introduction

In this chapter, we take the circuit model derived in Chapter 2 and establish an analytical technique for describing its behavior. We then proceed to describe the salient dynamics of the system under various conditions, including variations in the coupling modalities and distributional element-level parameter variations. We conclude by comparing the results of the model predictions with measurements taken from the experimental system and discuss the similarities and differences therein.

3.2 Derivation of the Continuum Representation of the System Equations

If we assume a sufficiently large resonator network (i.e. $N \rightarrow \infty$), the equations of motion given by Equation 2.6 may be solved by approximating the set of resonators as a spectrum, the parameters of which vary with an arbitrary index variable x . By doing this, we obtain a single integro-differential equation in t and x which fully describes the dynamics of the system. The benefit of this approach over the discrete is that the computational complexity associated with directly solving the discrete set of equations grows rapidly as the size of the system increases, while the continuum solution implicitly assumes an infinite number of resonators and thus its complexity is the same regardless of the size of the physical system being modeled.

The continuum form of these equations is shown in Equation 3.1 and was derived by redefining C_{di} and I_i as functions of x . Additionally, the summations have been replaced with integrals in x and normalized to retain their scaling with N . A population density function $\rho(x)$ has also been introduced which controls the relative density in the resonator count associated with a given value of x . A similar analytical technique

was also used in a prior work [42] to examine the dynamics of a similarly coupled system, though with the inclusion of element-level nonlinearities and exclusion of the parasitic elements.

$$\begin{aligned}
\dot{V}_f = & \left(1 + \frac{C_{0p}}{C_c}\right) \left[L_m \ddot{I}(x; t) + R_m \dot{I}(x; t) + \left(\frac{1}{C_m} + \frac{1}{C_d(x)}\right) I(x; t) \right] \\
& + R_c C_{0p} \left[L_m \ddot{I}(x; t) + R_m \dot{I}(x; t) + \left(\frac{1}{C_m} + \frac{1}{C_{di}}\right) I(x; t) \right] \\
& + L_{0p} C_{0p} \left[L_m I^{iv}(x; t) + R_m \ddot{I}(x; t) + \left(\frac{1}{C_m} + \frac{1}{C_d(x)}\right) \dot{I}(x; t) \right] \\
& + \frac{N}{C_c} \int_{-\infty}^{\infty} I(n; t) \rho(n) dn + N R_c \int_{-\infty}^{\infty} \dot{I}(n; t) \rho(n) dn + N L_{0p} \int_{-\infty}^{\infty} \ddot{I}(n; t) \rho(n) dn.
\end{aligned} \tag{3.1}$$

3.3 Solution of the Continuum Equations

A key advantage to the continuum representation of the system equations is the ability to derive a closed-form analytical solution in the frequency domain. One can begin by taking the Laplace transform and rearranging:

$$\begin{aligned}
sV_f(s) = & \left(1 + \frac{C_{0p}}{C_c} + C_{0p}R_c s + L_{0p}C_{0p}s^2\right) \left[L_m s^2 + R_m s + \left(\frac{1}{C_m} + \frac{1}{C_d(x)}\right) \right] I(x; s) \\
& + N \left(\frac{1}{C_c} + R_c s + L_{0p}s^2\right) \int_{-\infty}^{\infty} I(n; s) \rho(n) dn.
\end{aligned} \tag{3.2}$$

Next, let

$$\alpha(s) = 1 + \frac{C_{0p}}{C_c} + C_{0p}R_c s + L_{0p}C_{0p}s^2, \tag{3.3}$$

$$\lambda(s) = N \left(\frac{1}{C_c} + R_c s + L_{0p}s^2\right), \tag{3.4}$$

$$A(x; s) = \frac{1}{\alpha(s) \left[L_m s^2 + R_m s + \left(\frac{1}{C_m} + \frac{1}{C_d(x)}\right) \right]}, \tag{3.5}$$

$$K(x, n; s) = \frac{\rho(n)}{\alpha(s) \left[L_m s^2 + R_m s + \left(\frac{1}{C_m} + \frac{1}{C_d(x)} \right) \right]} = A(x; s) \rho(n), \quad (3.6)$$

and

$$F(x; s) = \frac{sV_f(s)}{\alpha(s) \left[L_m s^2 + R_m s + \left(\frac{1}{C_m} + \frac{1}{C_d(x)} \right) \right]} = sV_f(s)A(x; s). \quad (3.7)$$

Substituting into Equation 3.2 gives

$$I(x; s) + \lambda(s) \int_{-\infty}^{\infty} K(x, n; s) I(n; s) dn = F(x, s). \quad (3.8)$$

This takes the form of a Fredholm integral equation of the second kind, which has a well-known solution — the Liouville-Neumann series, which expresses the result as a series over an integral sequence in terms of K , λ , and F [79]:

$$I(x; s) = \sum_{n=0}^{\infty} (-\lambda(s))^n \Phi_n(x, s), \quad (3.9)$$

where

$$\Phi_j(x; s) = \int K_j(x, n; s) F(n, s) dn, \quad (3.10)$$

and

$$K_j(x, n; s) = \int \int \cdots \int K(x, y_1; s) K(y_1, y_2; s) \cdots K(y_{j-1}, n; s) dy_1 dy_2 \cdots dy_{j-1}. \quad (3.11)$$

For this system in particular, the kernel is separable as $K(x, n; s) = A(x; s)\rho(n)$ which allows the integral sequence to reduce to a geometric sequence:

$$K_j(x, n; s) = \int \int \cdots \int [A(x; s)p(y_1)][A(y_1; s)p(y_2)] \cdots [A(y_{j-1}; s)p(n)] dy_1 \cdots dy_{j-1},$$

$$K_j(x, n; s) = [A(x; s)p(n)] \int \int \cdots \int [A(y_1; s)p(y_1)] \cdots [A(y_{j-1}; s)p(y_{j-1})] dy_1 \cdots dy_{j-1},$$

and

$$K_j(x, n; s) = A(x; s)p(n) \prod_{i=1}^j B(s) = A(x; s)p(n)B(s)^{j-1}, \quad (3.12)$$

where

$$B(s) = \int_{-\infty}^{\infty} A(x; s)\rho(n)dn. \quad (3.13)$$

From here, the Liouville-Neumann series reduces to a simple geometric series in terms of $\lambda(s)B(s)$, ultimately giving the final result:

$$I(x; s) = \frac{sV_f(s)}{[L_m s^2 + R_m s + (\frac{1}{C_m} + \frac{1}{C_d(x)})][\alpha(s) + \lambda(s)\beta(s)]}, \quad (3.14)$$

where

$$\beta(s) = \int_{-\infty}^{\infty} \frac{1}{L_m s^2 + R_m s + (\frac{1}{C_m} + \frac{1}{C_d(n)})} \rho(n)dn. \quad (3.15)$$

The conditions for convergence of the series can be found by applying the standard ratio test:

$$\lim_{n \rightarrow \infty} \left| \frac{\lambda(s)^{n+1} \Phi_{n+1}(x; s)}{\lambda(s)^n \Phi_n(x; s)} \right| = \lim_{n \rightarrow \infty} \left| \frac{\lambda(s)^{n+1} B(s)^{n+1}}{\lambda(s)^n B(s)^n} \right| = \left| \frac{\lambda(s)\beta(s)}{\alpha(s)} \right| < 1. \quad (3.16)$$

Thus Equation 3.14 is valid for sufficiently small $\lambda(s)$ or $\beta(s)$, or sufficiently large $\alpha(s)$, corresponding to the assumption made in the derivation of the Liouville-Neumann series that the integral term of Equation 3.8 is small [79]. Divergence of the series outside of this region, however, does not imply that no solution exists, it is

merely an inconclusive result. In fact, it can be shown that Equation 3.14 is valid in the region $\left| \frac{\lambda(s)\beta(s)}{\alpha(s)} \right| > 1$ as well, either by rederiving it using a variant of the solution method presented in [79] which is compatible with this assumption or, more simply, by assuming a solution in the form of Equation 3.14, substituting it directly into Equation 3.8, and validating the resulting equation without condition:

$$\begin{aligned} \frac{F(x; s)}{\left(1 + \frac{\lambda(s)\beta(s)}{\alpha(s)}\right)} + \lambda(s) \int_{-\infty}^{\infty} K(x, n; s) \frac{F(n; s)}{\left(1 + \frac{\lambda(s)\beta(s)}{\alpha(s)}\right)} dn &= F(x, s), \\ F(x; s) + \lambda(s) \int_{-\infty}^{\infty} K(x, n; s) F(n; s) dn &= \left(1 + \frac{\lambda(s)\beta(s)}{\alpha(s)}\right) F(x, s), \\ F(x; s) + \lambda(s) \int_{-\infty}^{\infty} [A(x; s)\rho(n)][sV_f(s)A(n; s)] dn &= \left(1 + \frac{\lambda(s)\beta(s)}{\alpha(s)}\right) F(x, s), \\ F(x; s) + sV_f(s)A(x; s)\lambda(s) \int_{-\infty}^{\infty} A(n; s)\rho(n) dn &= \left(1 + \frac{\lambda(s)\beta(s)}{\alpha(s)}\right) F(x, s), \end{aligned}$$

thus

$$F(x; s) + F(x; s) \frac{\lambda(s)\beta(s)}{\alpha(s)} = \left(1 + \frac{\lambda(s)\beta(s)}{\alpha(s)}\right) F(x, s). \quad (3.17)$$

Therefore, Equation 3.14 is a valid solution in general. Note, however, that a singularity exists throughout this derivation in the case of $\frac{\lambda(s)\beta(s)}{\alpha(s)} = -1$. This singularity is physical in that it corresponds to a state in which the total impedance of the network is zero, giving infinite current as a result.

3.4 Discrete System Solution

Based on the results of the continuum system analysis, it is possible to recover the solution to the discrete system by setting:

$$\rho(x) = \frac{1}{N} \sum_{i=1}^N \delta(x_i - x). \quad (3.18)$$

and evaluating $I(x; s)$ at $x = x_i$, where x_i are the x -values corresponding to each resonator in the array and $\delta(x)$ is the Dirac delta function. Doing this for the $\beta(s)$ equation yields:

$$\beta(s) = \sum_{j=1}^N \frac{1}{L_m s^2 + R_m s + \left(\frac{1}{C_m} + \frac{1}{C_{di}}\right)} = \frac{\sum_{j=1}^N \prod_{k \neq j}^N L_m s^2 + R_m s + \left(\frac{1}{C_m} + \frac{1}{C_{dk}}\right)}{\prod_{j=1}^N L_m s^2 + R_m s + \left(\frac{1}{C_m} + \frac{1}{C_{di}}\right)}. \quad (3.19)$$

Substituting this formulation of $\beta(s)$ into the solution for resonator i and rearranging to achieve a rational function in s gives:

$$I_i(s) = \frac{sV_f(s) \prod_{j \neq i} [L_m s^2 + R_m s + \left(\frac{1}{C_m} + \frac{1}{C_{dj}}\right)]}{\alpha(s) \prod_{j=1}^N [L_m s^2 + R_m s + \left(\frac{1}{C_m} + \frac{1}{C_{di}}\right)] + \lambda(s) \sum_{j=1}^N \prod_{k \neq j} [L_m s^2 + R_m s + \left(\frac{1}{C_m} + \frac{1}{C_{dk}}\right)]}. \quad (3.20)$$

A quick check of the polynomial order in the denominator shows that the addition of the coupling elements has increased the system order from the original $2N$ by two (two from the $\alpha(s)$ term and $2N$ from the product). This implies that an additional resonance will be present in the system caused by the parasitic elements, which will be exploited for the purposes of system identification in subsequent sections. Additionally, the numerator order is observed to be $2N - 2$, implying up to $N - 1$ system-wide antiresonances may be present. Of course, were this a true continuum, the system order would be infinite, which would imply an arbitrarily large number of these frequencies.

3.5 Population Density Functions

The continuous population density functions were assumed to be zero outside the range $0 < x < 1$ and were normalized such that $\int_0^1 \rho(x) dx = 1$. For a DC

bias range of 0 to 5 V, the capacitance of the varactors used in the experimental setup was found to span 155 – 11.1 pF, implying that a varactor pair in series will span 77.5 – 5.55 pF. Since $C_d(x)$ has been ill-defined thus far, we define it such that $\frac{1}{C_d(x)} = 1.689 \times 10^{11}x + 1.290 \times 10^{10}$ (F⁻¹) for $x \in [0, 1]$, which provides a linear relation between the added stiffness and x and covers the full range of values achievable with the varactors. This choice of $C_d(x)$ allows x to be used as an analog for a crystal's detuned resonant frequency (i.e. setting $x = 0$ will result in a resonator with the lowest attainable resonant frequency in the subsequently examined experimental system, while setting $x = 1$ will result in the highest attainable frequency). The population density function $\rho(x)$ will then control the relative density in the resonator population associated with a particular frequency.

The values of C_d used in both the discrete approximation and the physical system were found using a lumped area approach as shown in Figure 3.1. First, the span $[0, 1]$ was divided into equal-area increments such that the area under $\rho(x)$ was equal to $\frac{1}{N}$, where N is the number of resonators in the discrete system. Next, the values of x which bisect each increment into sections of equal area were found and mapped to a set of detuning capacitances using the definition of C_d provided above. These values of C_d were then used directly in the discrete analytical solution and were mapped onto the experimental system using the known capacitance-bias curves of the varactors.

Three population density functions were considered in total: Dirac delta, constant, and quadratic distributions. The delta distribution results in a set of identical resonators (i.e. the system used to characterize the resonators and parasitics in Chapter 2). The constant and quadratic density functions and their discrete equivalents for $N = 16$ are shown in Figure 3.1 below, and the dynamic response of the system in each configuration will be discussed in a subsequent section.

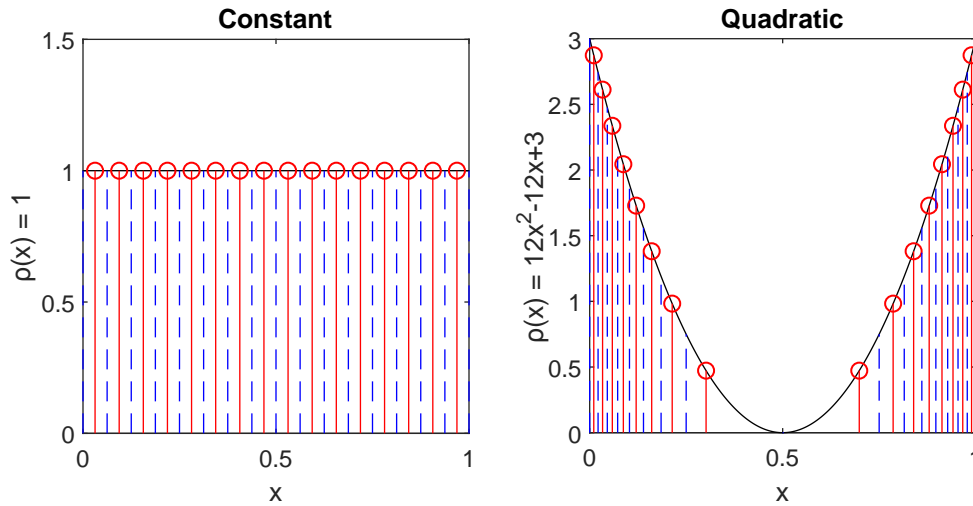


Figure 3.1. Population density functions for the constant and quadratic systems.

3.6 Convergence of the Discrete and Continuous Formulations

As an analysis tool for comparing the discrete and continuous systems, we can visualize the effect of discretization by plotting the magnitude and phase of the coupling term in Equation 3.1 normalized by the forcing function for each of the population density cases. These results are shown in Figure 3.2 for each of the distributions. Note use of a 16 MHz datum in frequency on this and subsequent figures, i.e. the x-axis values are differences relative to 16 MHz.

At a glance, the discrete solution and continuum approximation yield nearly identical responses for the constant distribution. The only notable differences are a slight ripple in the discrete response between each resonator's frequency and a slight leftward shift in the synchronous mode in the continuum response. Therefore, we conclude that the continuum formulation is generally a reasonable approximation of the system dynamics for this distribution.

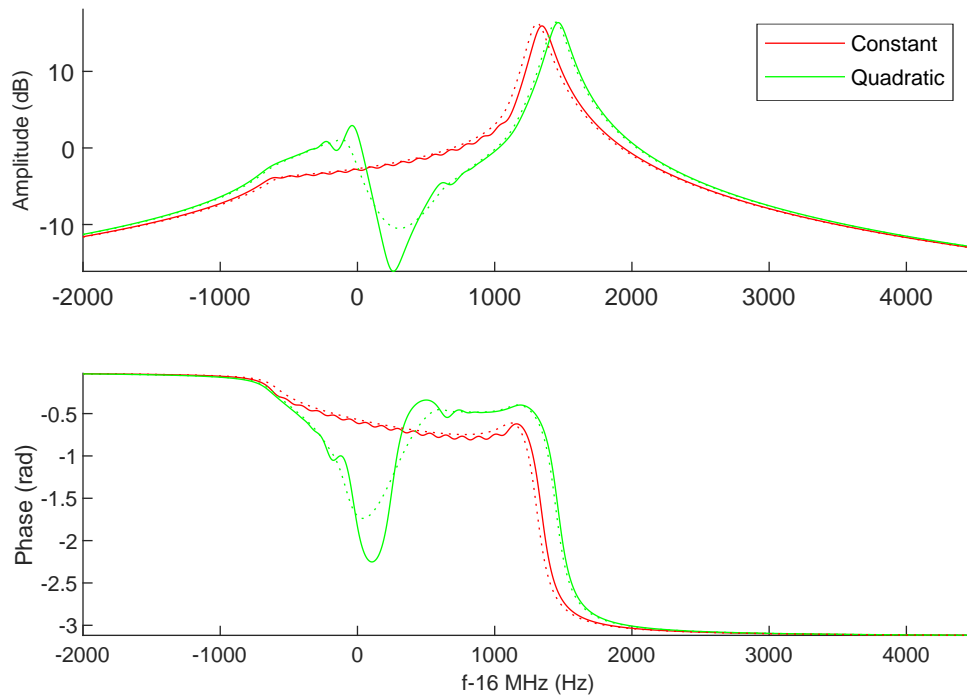


Figure 3.2. Comparison of the forcing-normalized coupling term for the (solid) discrete and (dashed) continuous solutions for each population density function with $C_c = 154$ pF and $R_c = 0$ Ω .

In the case of the quadratic system, the two methods still yield very similar results, except in the vicinity of the 0 Hz datum. This feature is unique to the quadratic distribution and is caused by the region of relatively low resonator population density in both the discrete and continuum solutions. This causes a breakdown in the continuum model of the system, as the initial assumption of an infinite continuum of resonators is no longer an accurate approximation when the gap between resonator bands becomes too large. This effect could be reduced, however, if more resonators were added to the discrete system, thus reducing the size of this gap. In practical terms, this divergence from the model should have minimal consequences when modeling the behavior of individual resonators. This is because the divergence only

happens in regions of very low population density, meaning that the discrete system will likely not have any resonators in this region for the error to be compared with. There may, however, be discrepancies when examining the dynamics at the common node, but this should not strongly effect the subsequent results in this chapter as they mainly focus on the responses of the resonators themselves.

3.7 Results and Discussion

3.7.1 Nearly-Identical System

Reactive Coupling

Figure 3.3 shows the measured responses for each of the resonators in the system. The responses were measured for systems consisting of 1, 8, and 16 resonators for values of C_c ranging from 154 pF to 11 pF. Key features include the decline in amplitude and the rightward shift in resonant frequency as C_c is decreased. The effect of the scaling factor of N on the coupling strength is also apparent as the rate of frequency shift versus C_c increases with N . The experimental results were found to be in reasonably good agreement with the model results from Section 2.7, though the discrepancies are more significant in the systems with larger N . There are a number of possible sources for this error, such as a failure of the model to take additional electrical components into account (such as the DC blocking series capacitances or the parasitic shunt capacitances across the resonators themselves), which may affect the relationship between the response and array size. Additionally, this may be caused by a breakdown of the Butterworth Van-Dyke equivalent circuit for the resonators. This model makes the assumption that these crystals are being operated near their natural frequency. When the crystals are being forced to operate significantly away from this point, the impedance may begin to diverge from that of a typical series RLC circuit, increasing the sensitivity of the crystals' frequency to the

added coupling capacitance beyond what is predicted by the basic Butterworth-Van Dyke model.

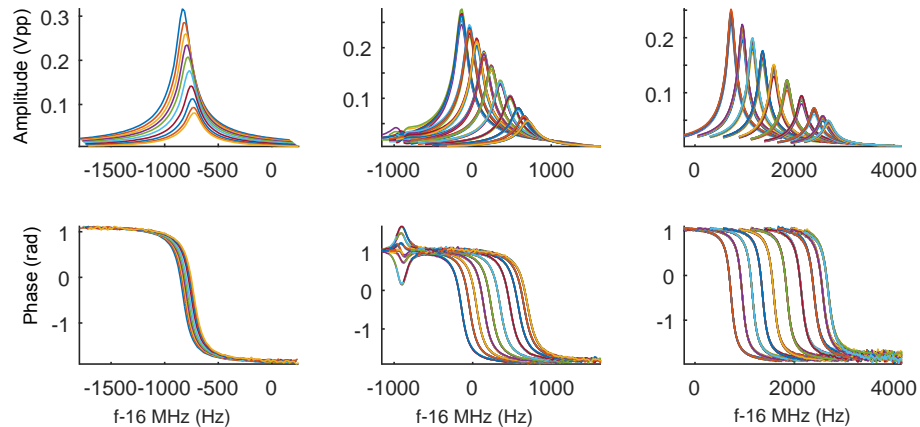


Figure 3.3. Experimental frequency response sweeps for a reactively coupled system for $N =$ (left) 1, (center) 8, and (right) 16. Each color represents an overlay of the responses of all of the resonators at varying values of C_c decreasing as the distributions shift to the right.

3.7.2 Dissipative Coupling

Figure 3.4 shows the predicted response of the continuous system with a coupling resistance value R_c of 100Ω for $C_c = 154 \text{ pF}$ and 11 pF . Figure 3.5 shows the experimentally obtained results of the corresponding physical system. The most notable features in the system with dissipative coupling are the significant decrease in quality factor when R_c is added to the system and the partial recovery as C_c is decreased. The experimental results confirm the prediction of the model in that regard, though the measured amplitude is slightly higher than expected. The features on the left half of the distributions in Figure 3.5 are the result of the resonators not being perfectly matched, which causes a region where the responses diverge near their natural resonance frequencies. However, these effects become less significant as the system is detuned further away from these frequencies.

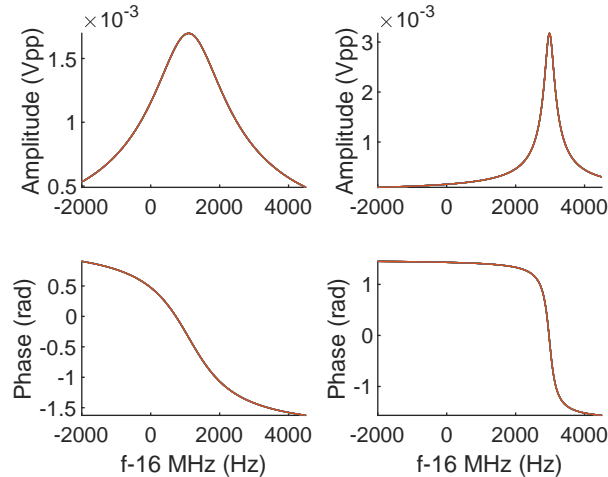


Figure 3.4. Predicted response from both the continuous and discrete models (which give identical results) with no added mistuning (i.e. C_{di} is shorted) for values of $R_c = 100 \Omega$ and (left) $C_c = 154 \text{ pF}$ and (right) $C_c = 11 \text{ pF}$.

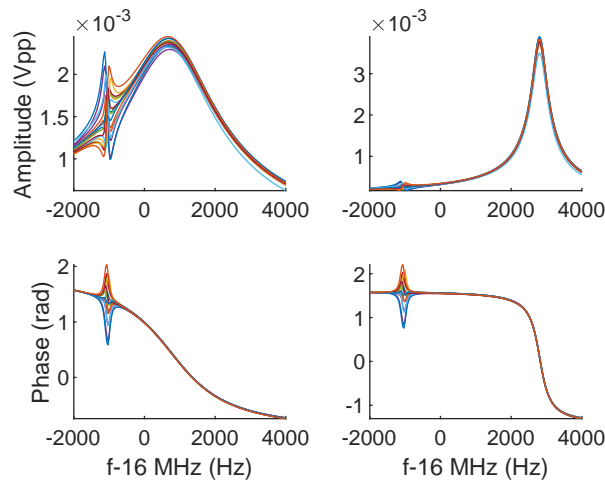


Figure 3.5. Experimental responses for a system with no added mistuning (i.e. C_{di} is shorted) for values of $R_c = 100 \Omega$ and (left) $C_c = 154 \text{ pF}$ and (right) $C_c = 11 \text{ pF}$. Each curve represents the response of a single resonator.

3.7.3 Constant Population Density

Reactive Coupling

The form of the model described by Equation 3.14 appears to predict two types of resonances: one at the normal detuned frequency for the resonator at index x ,

and a resonance at frequencies which minimize the $\alpha(s) + \lambda(s)\beta(s)$ term. Note that this term is independent of the index variable x . This implies that these particular resonance frequencies are properties of the system as a whole and common to all of the resonators in the array. The number and locations of these resonances are primarily functions of the population density function [through $\beta(s)$], the coupling type and strength [through $\lambda(s)$], and the parasitics in the system [through $\alpha(s)$]. Examining the responses of several resonators in the system with constant population density (shown in Figures 3.6-3.7) confirms the presence of these resonances in both the continuum models and experimental results. As can be seen in the figures, the distribution of resonators retain their expected resonance peaks at their natural detuned frequencies, as well as a relatively strong synchronous mode which shifts rightward as the coupling capacitance C_c is reduced. Additionally, there is significant attenuation in amplitude as C_c is reduced, which is caused by the $\frac{1}{C_c}$ terms in α and λ .

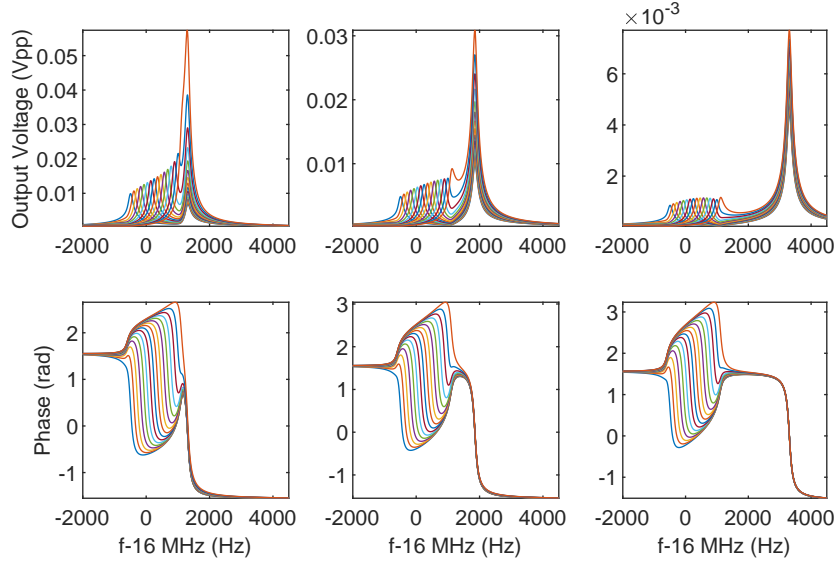


Figure 3.6. Predicted response for the continuum solution with a constant population density for values of (left) $C_c = 154$ pF, (center) $C_c = 67.8$ pF, and (right) $C_c = 11$ pF. Each curve represents the response of a single resonator evaluated at the values of x defined by the lumped population density function.

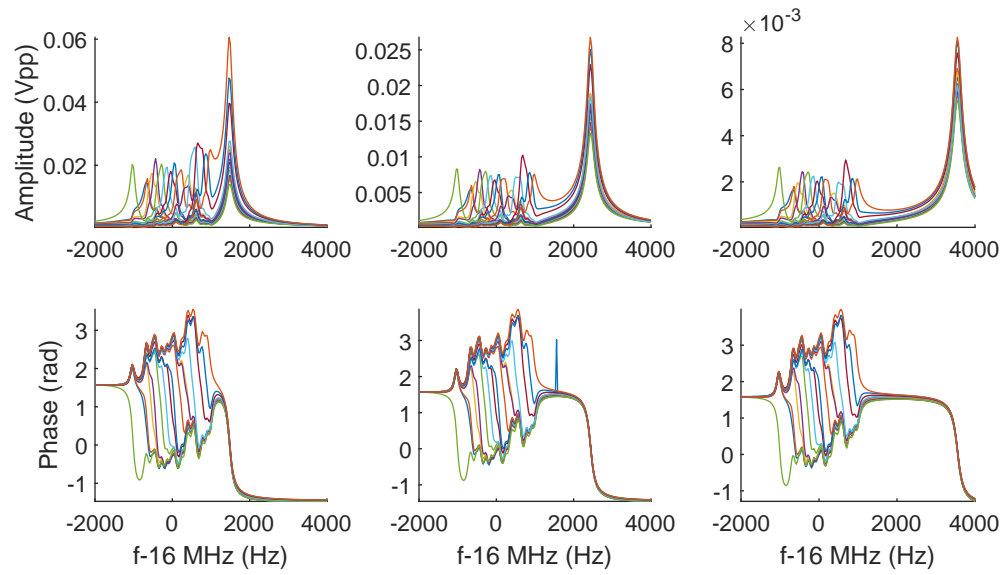


Figure 3.7. Experimentally obtained response for each of the 16 resonators with a constant population density for values of (left) $C_c = 154$ pF, (center) $C_c = 67.8$ pF, and (right) $C_c = 11$ pF. Each curve represents the response of a single resonator.

Dissipative Coupling

Figures 3.8 and 3.9 show the predicted responses of the continuous system with coupling resistance (R_c) values of 50Ω and 100Ω , respectively, with $C_c = 154 \text{ pF}$, 67.8 pF , and 11 pF . Figures 3.10 and 3.11 show the experimentally obtained results. As with the nearly-identical system, the most significant effect of increasing R_c is a drop in amplitude, though in this case the attenuation is not uniform across every mode. Using Resonator 1 (leftmost, in green) in Figure 3.11 (right) as an example, the resonance in the vicinity of the natural frequency was found to have an effective quality factor of 94.5×10^3 , which is still comparable to the original value of 101×10^3 . However, the effective quality factor associated with the synchronous mode was found to have dropped to 55.9×10^3 , implying that the dissipative element has a much stronger effect on the synchronous mode than the other modes of the system. Additionally, the relationship between the quality factor and C_c observed in the nearly-identical system seems to hold here as well, since the synchronous mode begins with a low effective quality factor in the system with weak reactive coupling but improves significantly when stronger reactive coupling is introduced.

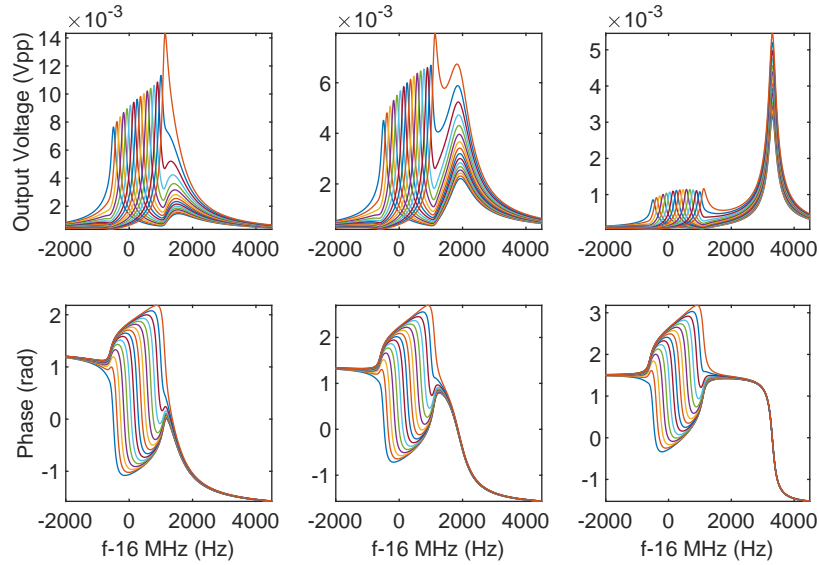


Figure 3.8. Predicted response for the continuum solution with a constant population density for values of $R_c = 50 \Omega$ and (left) $C_c = 154$ pF, (center) $C_c = 67.8$ pF, and (right) $C_c = 11$ pF.

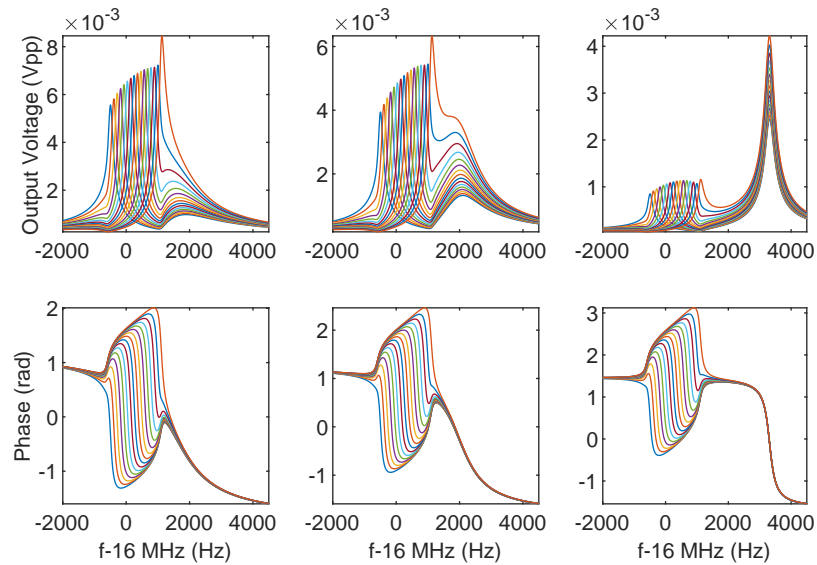


Figure 3.9. Predicted response for the continuum solution with a constant population density for values of $R_c = 100 \Omega$ and (left) $C_c = 154$ pF, (center) $C_c = 67.8$ pF, and (right) $C_c = 11$ pF.

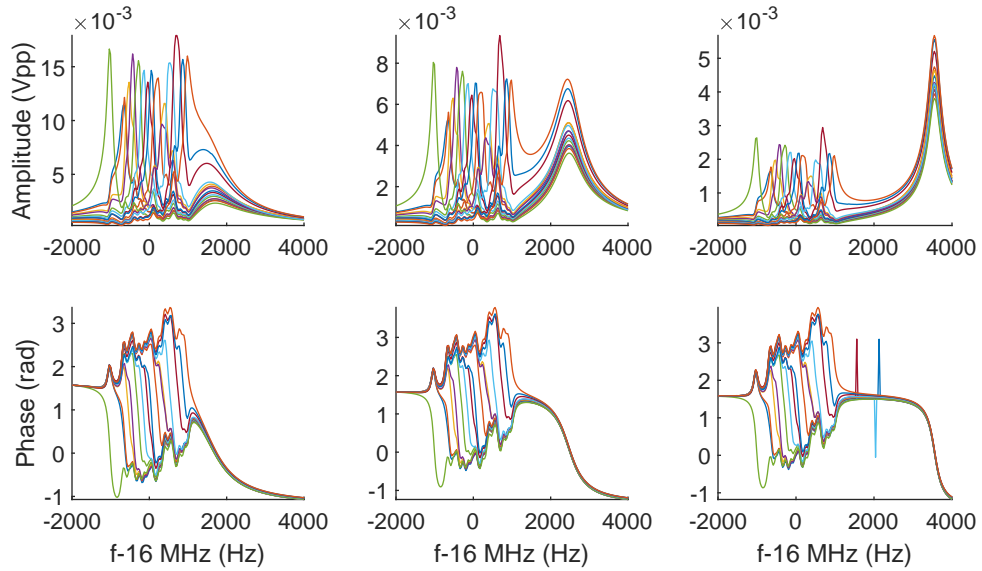


Figure 3.10. Experimentally obtained response with a constant population density for values of $R_c = 50 \Omega$ and (left) $C_c = 154 \text{ pF}$, (center) $C_c = 67.8 \text{ pF}$, and (right) $C_c = 11 \text{ pF}$.

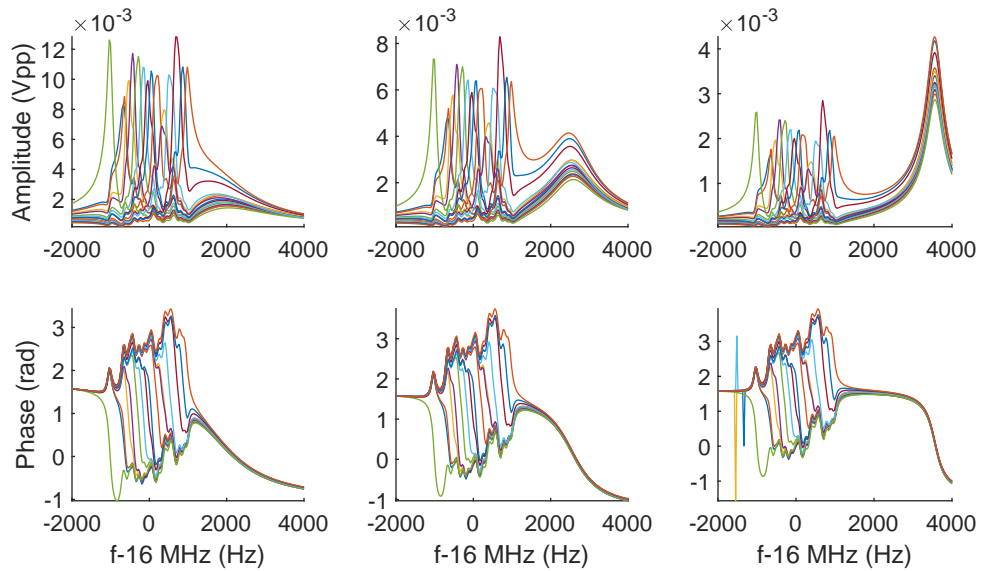


Figure 3.11. Experimentally obtained response with a constant population density for values of $R_c = 100 \Omega$ and (left) $C_c = 154 \text{ pF}$, (center) $C_c = 67.8 \text{ pF}$, and (right) $C_c = 11 \text{ pF}$.

3.7.4 Quadratic Population Density

Reactive Coupling

The predicted response for the system with purely reactive coupling using the quadratic population density is shown in Figure 3.12. The quadratic system shows trends similar to the constant system, but includes the notable addition of a second collective mode which is shared between the resonators appearing in between the two “clusters” of high resonator population density which are separated in frequency. The resonators whose natural bands overlap with this mode show a very strong response on par with that of the synchronous mode. Like the main synchronous mode, this mode shifts rightward as C_c is decreased, though unlike the other mode, this one seems to approach a limit in frequency in between the two resonator clusters. Figure 3.13 shows the experimental realization of this configuration, which shows nearly identical features.

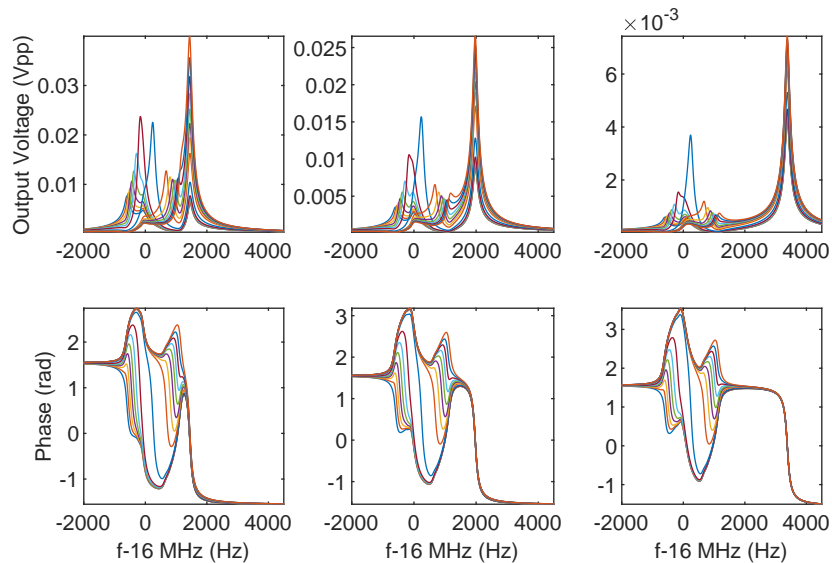


Figure 3.12. Predicted response for the continuum solution with a quadratic population density for values of (left) $C_c = 154$ pF, (center) $C_c = 67.8$ pF, and (right) $C_c = 11$ pF.

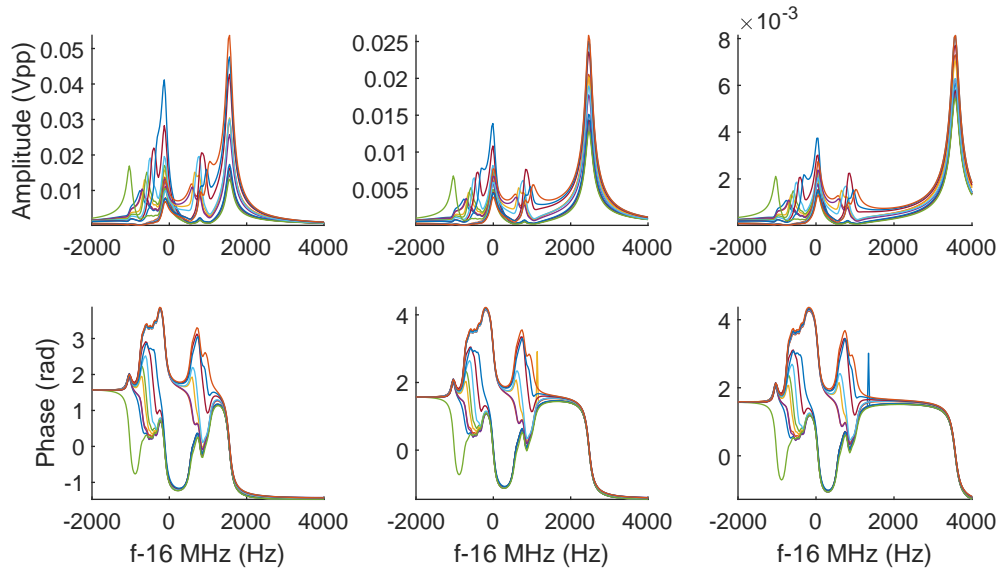


Figure 3.13. Experimentally obtained response for each of the 16 resonators with a quadratic population density for values of (left) $C_c = 154$ pF, (center) $C_c = 67.8$ pF, and (right) $C_c = 11$ pF.

Dissipative Coupling

Figures 3.14 and 3.15 show the responses of the system predicted by the continuum formulation with coupling resistance values R_c of 50Ω and 100Ω , respectively, with $C_c = 154$ pF, 67.8 pF, and 11 pF. Figures 3.16 and 3.17 show the experimentally obtained results. As before, the most notable result of the introduction of dissipative coupling is an attenuation in amplitude and effective quality factor which was greater in magnitude for the synchronous modes than the other modes of the system. Additionally, the quality factor was found to improve with decreasing C_c in the secondary synchronous mode, as well as the primary.

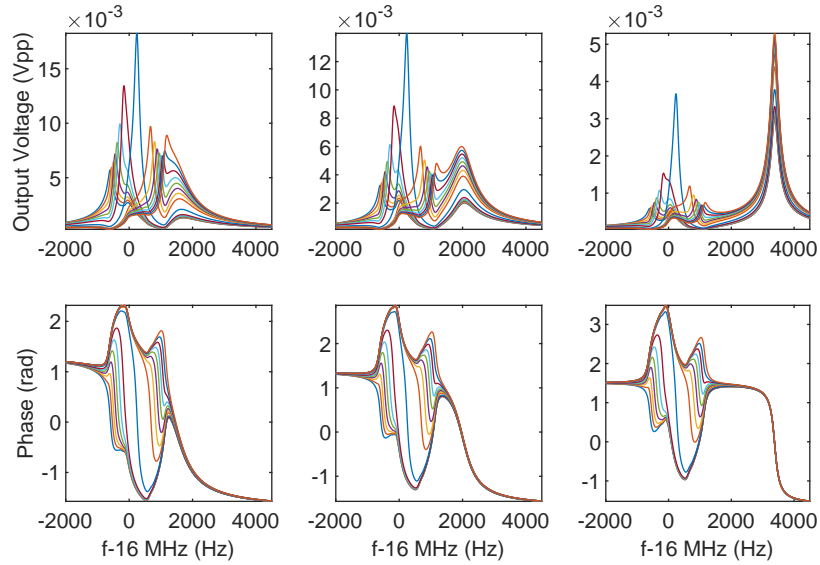


Figure 3.14. Predicted response of the continuum solution with a quadratic population density for values of $R_c = 50 \Omega$ and (left) $C_c = 154 \text{ pF}$, (center) $C_c = 67.8 \text{ pF}$, and (right) $C_c = 11 \text{ pF}$.

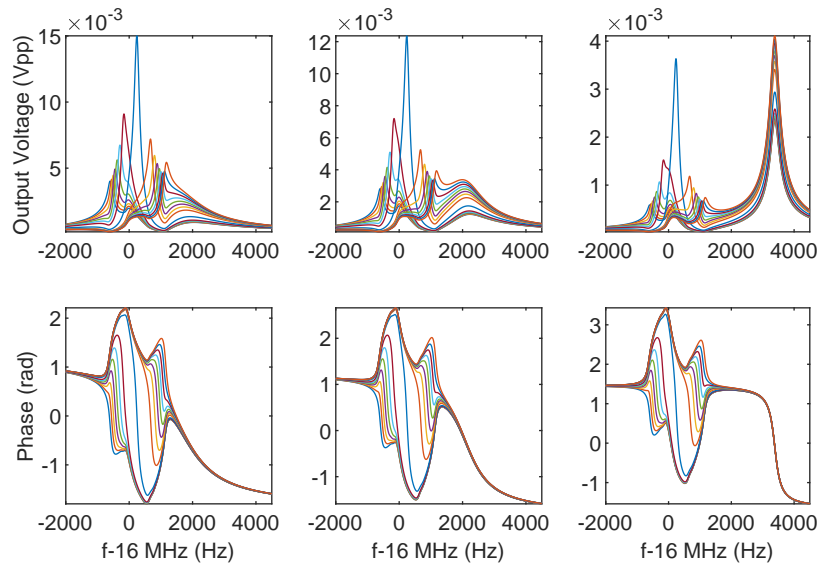


Figure 3.15. Predicted response for the continuum solution with a quadratic population density for values of $R_c = 100 \Omega$ and (left) $C_c = 154 \text{ pF}$, (center) $C_c = 67.8 \text{ pF}$, and (right) $C_c = 11 \text{ pF}$.

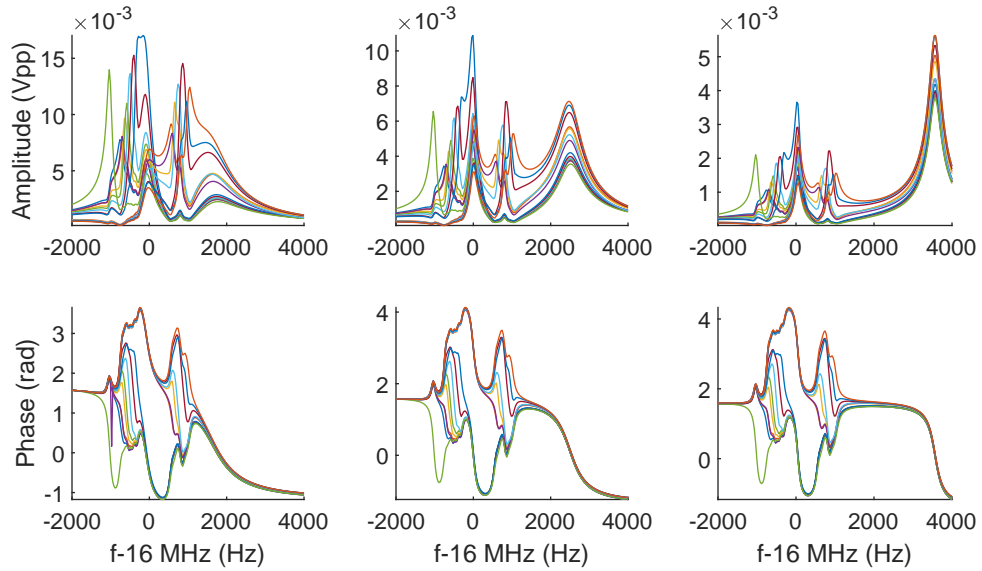


Figure 3.16. Experimentally obtained response with a quadratic population density for values of $R_c = 50 \Omega$ and (left) $C_c = 154 \text{ pF}$, (center) $C_c = 67.8 \text{ pF}$, and (right) $C_c = 11 \text{ pF}$.

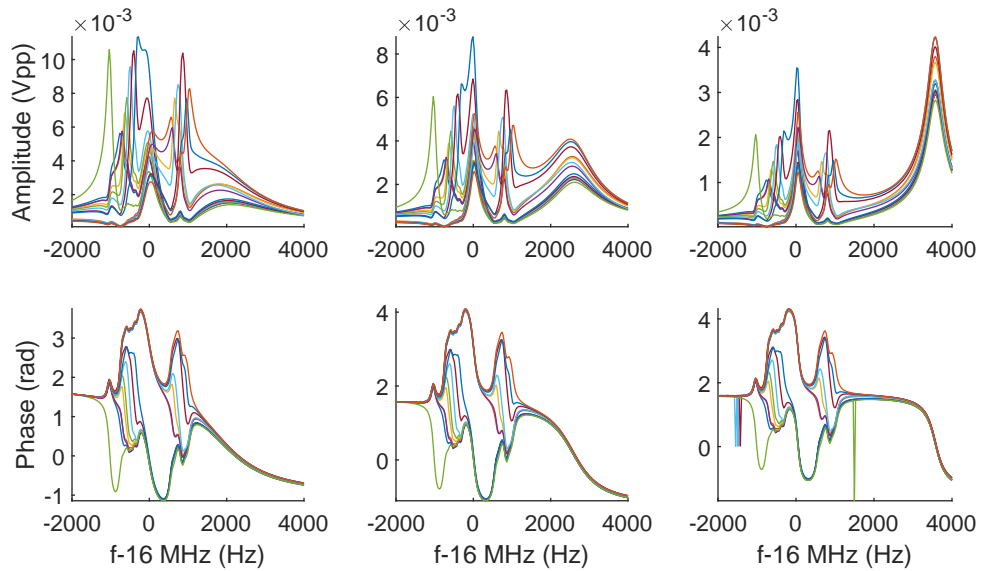


Figure 3.17. Experimentally obtained response with a quadratic population density for values of $R_c = 100 \Omega$ and (left) $C_c = 154 \text{ pF}$, (center) $C_c = 67.8 \text{ pF}$, and (right) $C_c = 11 \text{ pF}$.

3.8 Conclusions

In this chapter (and the previous), an architecture was proposed, constructed, and characterized for a system consisting of a parallel array of reactively and dissipatively coupled electromechanical resonators. This architecture may serve as an analog for other, similar, coupled systems, such as MEMS/NEMS resonator arrays, piezo-based systems such as those used in some energy harvesting applications, or other types of electromechanical systems. The behaviors of this system were examined in detail under varying coupling conditions and array sizes. The combined effects of intentional mistuning and reactive coupling were investigated and found to induce an additional resonance in the crystals which is dependent on the global properties of the system. Additionally, it was shown that an arbitrarily large number of system-wide antiresonances can be generated given a sufficiently large system, that the presence of these antiresonances can be controlled by careful selection of the element-level parameter distributions in the array, and that these antiresonances can provide for interesting collective modes of motion. Of particular interest to the authors is the possibility of exploiting these types of behaviors for resonant mass sensing applications, a subject which will be explored in detail in Chapter 4.

4. A SINGLE-INPUT, SINGLE-OUTPUT MULTI-ANALYTE VAPOR SENSOR BASED UPON REACTIVELY COUPLED RESONANT ELEMENTS

4.1 Introduction

Recent works have applied resonant mass sensors to applications in volatile organic compound (VOC) detection and other air quality monitoring applications due to their relatively high sensitivities and low power consumption [26, 80–83]. However, while these properties make these sensors attractive for many applications, they have a major drawback in the sense that typical implementations lack selectivity towards multiple analytes, i.e. the sensors can detect that mass of some kind has been added, but are unable to differentiate between different compounds (or classes thereof). This limitation can be overcome to some degree by parallelization of sensors with varying sensitivities to different compounds; however, doing so on a large scale can quickly drive up the ordinarily low power consumption of a device, and the cost of acquisition hardware scales dramatically as the throughput requirements for monitoring a large number of resonant devices simultaneously increase.

One solution to these throughput limitations is to make use of specialty hardware such as field-programmable gate arrays (FPGAs) to parallelize the monitoring process [84, 85]; however, there are still physical limitations associated with these methods in terms of the sheer number of on-board traces/ports that would be required to monitor a very large number of devices. A number of recent works have sought to alleviate this throughput problem by exploiting higher-order dynamics (particularly emergent behaviors in coupled systems) to create devices which are selective to multiple analytes; however, these efforts have been limited to a relatively small number of analytes [14, 20, 22–24, 39, 86].

Resonant mass sensors are commonly implemented in the form of micro-/nano-electromechanical devices, due to the ability to create high quality resonant elements with minimal footprints [15, 17, 23, 24, 29]. On the macro-scale, a common implementation of resonant mass sensor is the quartz crystal microbalance (QCM). This type of sensor consists of a crystal resonator upon the surface of which some amount of mass is deposited. Due to the inertial loading on the crystal, the frequency of the resonator is lowered in proportion to the added mass. In the field of chemical vapor detection, these crystals are often coated via a process such as electroplating or inkjet printing [19, 87] with some chemical sorbent which will bind a target analyte to the crystal's surface. In this work, we seek to overcome the aforementioned throughput limitations by exploiting the emergent behaviors of a coupled resonant system in order to monitor a large number of devices simultaneously. In particular, we leverage the presence of localized modes of vibration in an array of mistuned, reactively coupled crystal resonators to indirectly monitor shifts in the natural frequencies of the individual resonant elements.

4.2 Methodology

4.2.1 Electrical Overview

The system of interest initially consists of a parallel array of 16 crystal resonators, though, as will be discussed in subsequent sections, this number will be reduced to 7 due to practical limitations on the system. The array is driven by an external function generator, a diagram of which is shown in Figure 4.1. The excitation is buffered through a unity-gain inverting amplifier to avoid dynamics caused by the generator driving a dynamic load. The resonators are reactively coupled by connecting a capacitive element $C_c = 154$ pF in series between the array and the output of the buffer. Additionally, a parasitic shunt capacitance $C_0 = 488$ pF exists in the physical circuit in parallel with the array, the dynamics of which are significant enough to necessitate inclusion in the model.

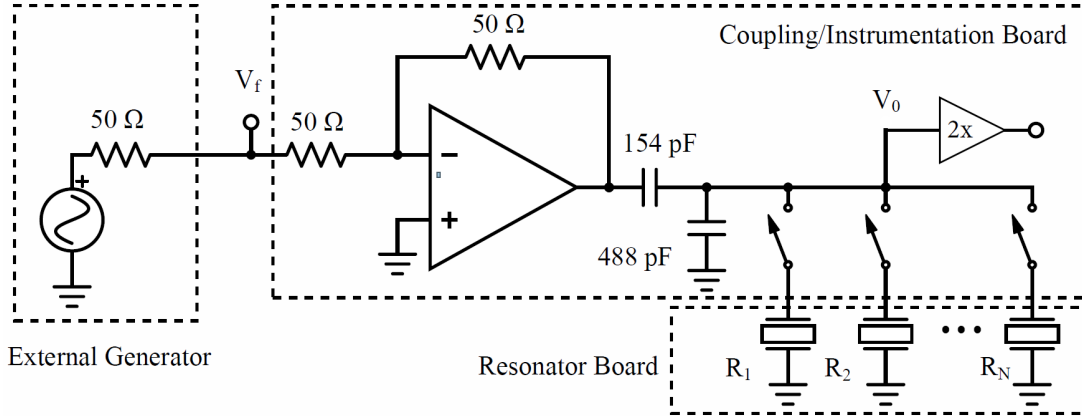


Figure 4.1. Circuit diagram showing the layout of the circuit. The dashed boxes separate the components which are on separate circuit boards.

The frequency response of the system is measured via the voltage at the common node of the resonator array, V_0 . An analog switch is placed in series with each resonator which allows the individual resonant elements to be disconnected from the circuit. The circuit as a whole is partitioned into two separate circuit boards: a coupling/instrumentation board and a resonator board. This partitioning allows different sets resonators to be exchanged quickly, without having to resort to soldering/desoldering the devices. The instrumentation board holds the input/output ports, the buffers, the switches and their associated digital logic components, and the coupling element, while the resonator board holds only the resonators themselves, which are arranged in a 4-by-4 grid. Electrical connections between the boards are made via an array of spring-loaded pogo pins mounted on the instrumentation board which connect to a pair of landing pads under each resonator on the resonator board. Figure 4.2 shows the physical realization of these boards.

The electrical dynamics of each resonator can be approximated by using the Butterworth-Van Dyke equivalent circuit model, shown in Figure 4.3 [88]. In this model, L_m , R_m , and C_m are referred to as the motional inductance, resistance, and

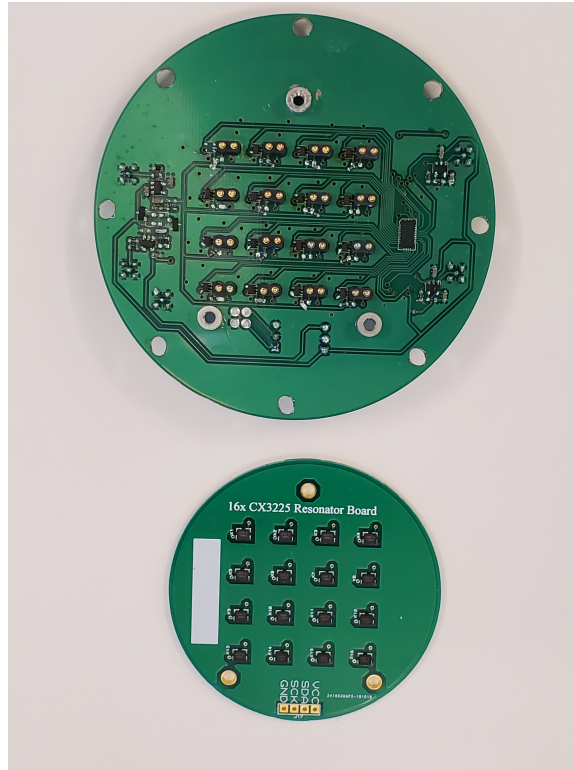


Figure 4.2. Physical realization of the coupling/instrumentation board. The top image shows the coupling/instrumentation board, while the bottom row shows the resonator board with its 4x4 grid of crystal resonators.

capacitance, and C_s the shunt capacitance. If the shunt capacitance is small enough to be neglected, the equation of motion for the i^{th} crystal is given by:

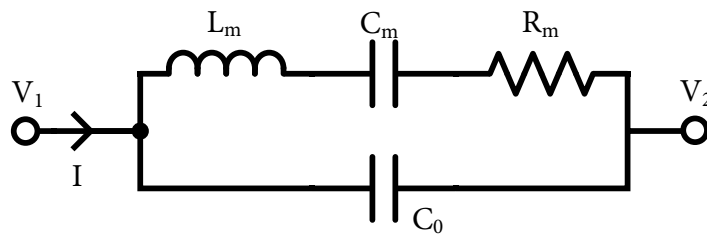


Figure 4.3. Diagram showing the Butterworth-Van Dyke equivalent circuit for a crystal resonator.

$$\dot{V}_0 = L_{mi}\ddot{I}_i + R_{mi}\dot{I}_i + \frac{1}{C_{mi}}I_i. \quad (4.1)$$

While the crystals used in this work are nominally identical, when mass is deposited on the surface of the crystal the additional inertial load imparted will lower the natural frequency. For a weakly damped system with a small variation in mass, this shift can be approximated by:

$$\delta f \approx -\frac{f_0}{2L_{m0}}\delta L_m, \quad (4.2)$$

where f_0 and L_{m0} are the initial natural frequency and motional inductance, δf is the change in frequency, and δL_m is the equivalent motional inductance of the added mass. In the coupled system shown in Figure 4.1, the dynamics of the common node voltage can be derived in the Laplace domain as:

$$V_0(s) = V_f(s)\frac{Z_1(s)}{Z_1(s) + Z_c(s)}, \quad (4.3)$$

where the impedance $Z_1(s)$ is the total parallel impedance of the array and shunt capacitance given by:

$$Z_1(s) = Z_{array}(s) \parallel Z_0(s) \equiv \frac{Z_{array}(s)Z_0(s)}{Z_{array}(s) + Z_0(s)}. \quad (4.4)$$

Additionally, the array impedance is given by

$$\frac{1}{Z_{array}(s)} = \sum_{i=1}^N \frac{1}{L_{mi}s + R_{mi} + \frac{1}{sC_{mi}}} = \frac{\sum_{i=1}^N \prod_{j \neq i} L_{mj}s + R_{mj} + \frac{1}{sC_{mj}}}{\prod_{j=1}^N L_{mj}s + R_{mj} + \frac{1}{sC_{mj}}}, \quad (4.5)$$

and the capacitive impedances Z_c and Z_0 by:

$$Z_{c,0}(s) = \frac{1}{sC_{c,0}}. \quad (4.6)$$

Substituting gives the total response of V_0 as:

$$\frac{V_0(s)}{V_f(s)} = \frac{\frac{C_c}{(C_0+C_c)} \prod_{j=1}^N L_{mj}s + R_{mj} + \frac{1}{sC_{mj}}}{\prod_{j=1}^N \left[L_{mj}s + R_{mj} + \frac{1}{sC_{mj}} \right] + \frac{1}{s(C_0+C_c)} \sum_{i=1}^N \prod_{j \neq i} \left[L_{mj}s + R_{mj} + \frac{1}{sC_{mj}} \right]}. \quad (4.7)$$

Consider this response in the vicinity of the k^{th} resonator's natural frequency, ω_k , making the assumption that the resonators are well-separated in frequency. This assumption implies that the other resonators are in a high impedance state at this frequency, i.e. $|Z_i(s)|_{i \neq k} \gg |Z_k(s)|$ in the vicinity of $s = i\omega_k$. With these assumptions, we can reduce the transfer function given by Equation 4.7 to:

$$\frac{V_0(s)}{V_f(s)} \approx \left(\frac{C_c}{C_c + C_0} \right) \frac{L_{mk}s + R_{mk} + \frac{1}{sC_{mk}}}{L_{mk}s + R_{mk} + \frac{1}{s} \left(\frac{1}{C_{mk}} + \frac{1}{C_c + C_0} \right)}. \quad (4.8)$$

Under these conditions, the spectral response of the system in the vicinity of ω_k will consist of an antiresonance at the location of resonator k 's uncoupled resonance frequency, as well as a resonance at a slightly higher frequency due to the added stiffness from the coupling capacitance C_c and shunt capacitance C_0 . Provided that this added stiffness is much smaller than the stiffness from the motional capacitance, the quality factor and magnitude of the resonance and antiresonance will be very nearly the same. Additionally, provided that the amount of adsorbed mass is not enough to significantly alter the damping characteristics of the resonator during operation, this offset in frequency will be approximately constant.

4.2.2 System Interrogation

The response of the system to vapor exposure is encoded in the frequency response of the common node voltage, V_0 , via changes in the locations of the aforementioned antiresonances. In order to measure the response of the system, the spectral response in an approximately 10 kHz window near the resonators' natural frequencies needs to

be measured. A relatively direct method of doing so would be to use a lock-in amplifier with a built-in sweep function to probe the region in frequency. However, doing this with a reasonable degree of resolution takes a significant amount of time, on the order of 20 min for a 1 Hz resolution sweep, which is untenable for a sensing application where dynamics occur on the order of seconds. In order to bypass this limitation, we instead use a frequency-modulated sine wave as the input voltage, which will generate a narrow band of excitation in the region of interest. The expression for the input signal is given by:

$$V_f(t) = A \sin \left[2\pi(f_c + \delta_f \sin[2\pi f_{mod}t])t \right], \quad (4.9)$$

where each parameter is as given in Table 4.1. This function generates a relatively flat band of excitation in frequency centered at f_c and spanning $\pm\delta_f$. A sample of this spectrum is shown in Figure 4.4.

Table 4.1. Excitation signal parameters.

| Symbol | Description | Value |
|------------|-------------------------|------------|
| A | Signal Amplitude | 1 V |
| f_c | FM Carrier Frequency | 15.995 MHz |
| f_{mod} | FM Modulation Frequency | 1 Hz |
| δ_f | Modulation Depth | 5 kHz |

To recover the frequency response, both V_f and V_0 are measured over a full modulation cycle. Due to constraints on acquisition memory depth, each signal is passed through a demodulator which is configured to shift the excitation band from a center frequency of 15.995 MHz to 10 kHz. Each demodulator consists of an AD835 analog multiplier and a low pass filter. The multiplier multiplies the measured voltage by a sinusoidal signal with a 1 V amplitude and frequency of 15.985 MHz. This results in a signal whose spectrum contains two images at half the amplitude of the original spectrum, each centered at $f_c \pm f_{demod}$. The higher frequency image is then filtered

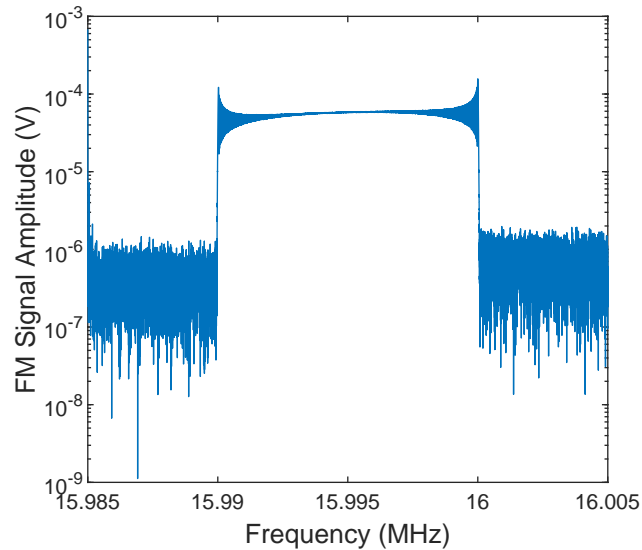


Figure 4.4. Amplitude spectrum of the excitation signal. The relatively flat, narrow region of high excitation is centered on the carrier frequency (15.995 MHz) and spans a 10 kHz band.

from the signal using a first-order, low-pass filter with a cutoff of 100 kHz. Acquisition is then performed using an oscilloscope sampling at 40 kSa/s. Figure 4.11 shows a sample of the measured frequency response of the system, truncated to the 10 kHz band of interest and offset in frequency to reflect the absolute frequency range of the system.

4.2.3 Recovery of the Population Density Function

Figure 4.5 shows the frequency response spectrum of a simulated system with 3 resonators. The simplest means of tracking each resonator's shift in frequency over time is to simply follow the peaks of this response directly. This method may work well in some cases; however, having multiple resonators in close proximity can distort the peaks in such a way that this approach no longer gives a robust approximation of their uncoupled response. This imposes unnecessarily strict restrictions on the spacing of the resonators, necessitating more precise control over their mistuning,

limiting the number of resonators which can be placed in a given frequency band, and reducing the overall fidelity of the frequency shift measurements.

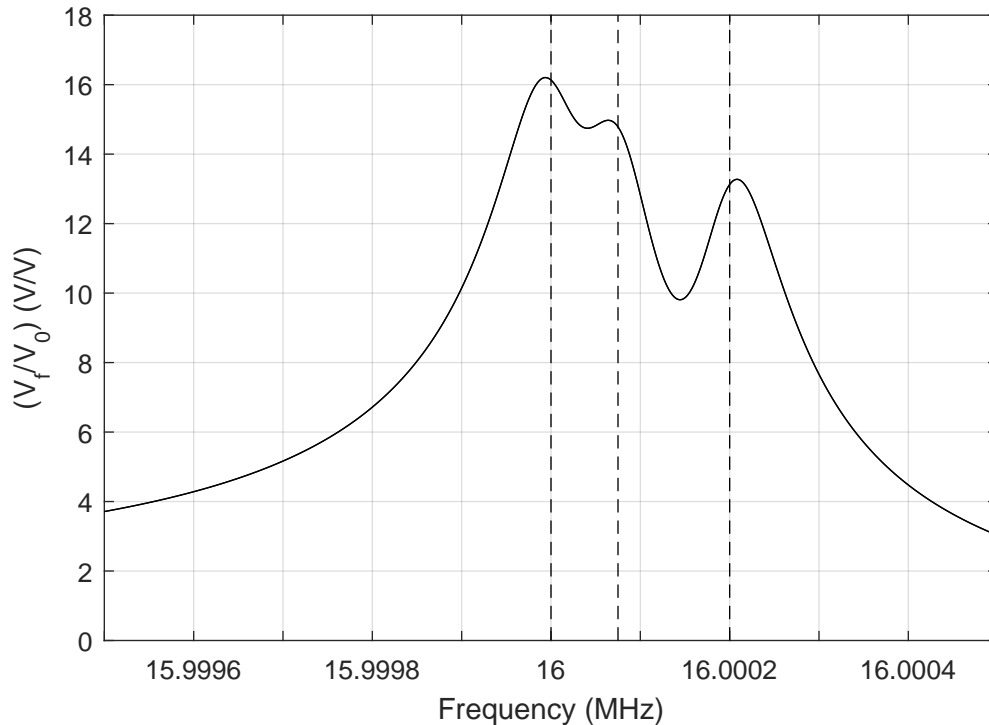


Figure 4.5. Simulated frequency response of the system. The dashed lines show the actual frequencies of the resonators in the simulation.

Borrowing from the analysis shown in Chapter 3, under the assumption that the individual resonators are well-matched but slightly mistuned, the measured spectral response, $\frac{V_0(f)}{V_f(f)}$, can be expressed in terms of a convolution between the spectral response of a single resonator with a population density function:

$$\frac{V_0(f)}{V_f(f)} = \frac{1}{1 + Z_c(f) \left[\frac{1}{Z_0(f)} + \Psi^*(f) * \rho(f) \right]}, \quad (4.10)$$

where $Z_c(f)$ and Z_0 are, respectively, the total impedance of the coupling circuit and shunt capacitance, $\rho(f)$ is the population density function, and $\Psi(f)$ is the characteristic admittance for a single resonator. For the purposes of this chapter, we will

consider the value of $\Psi(f)$ to be given by the high-frequency, constant-bandwidth, resonance-centered approximation of the admittance of a series RLC circuit, given by:

$$\begin{aligned}\Psi(f) &= \lim_{f_0 \rightarrow \infty} \frac{4\pi^2 B(f - f_0)}{-4\pi^2(f - f_0)^2 + 4i\pi^2 B(f - f_0) + 4\pi^2 f_0^2} \\ &= \lim_{f_0 \rightarrow \infty} \frac{-iB}{2(f - f_0) - iB + 2f_0} \\ &= \frac{B}{B + 2if},\end{aligned}\tag{4.11}$$

where B is the -3 dB bandwidth of the circuit, and f is the frequency deviation from the natural frequency, f_0 . In general, it is not the peaks in the raw distribution that must be localized in frequency, but the locations of the peaks in the population density function, $\rho(f)$. In order to calculate this function, it is necessary to execute a deconvolution operation on the raw data, i.e. find a function $g(f)$ such that:

$$\rho(f) = \left[\frac{\frac{V_f(f)}{V_0(f)} - 1}{Z_c(f)} - \frac{1}{Z_0(f)} \right] * g(f) = \beta(f) * g(f).\tag{4.12}$$

The most direct way of calculating this function is simply to apply the convolution theorem for Fourier/Inverse Fourier transforms:

$$g(f) = \mathcal{F} \left[\frac{1}{\mathcal{F}^{-1}[\Psi(f)]} \right],\tag{4.13}$$

$$\rho(f) = \mathcal{F} \left[\frac{\mathcal{F}^{-1}[\beta(f)]}{\mathcal{F}^{-1}[\Psi(f)]} \right].\tag{4.14}$$

Unfortunately, this methodology yields poor results in practice, due to deconvolution operations in general being exceptionally sensitive to noise. Instead, we must apply additional filtering to the operation in the form of a Wiener deconvolution:

$$g(f) = \mathcal{F} \left[\frac{1}{\mathcal{F}^{-1}[\Psi(f)]} \frac{1}{1 - \frac{1}{|\mathcal{F}^{-1}[\Psi(f)]|^2 SNR}} \right],\tag{4.15}$$

where SNR is the approximate signal-to-noise ratio of the measured signal. Figure 4.6 shows the result of applying this operation to the simulated distribution shown

in Figure 4.5, as well as the values of $\frac{V_f}{V_0}$ and β . Note that the signal-to-noise ratio is (nearly) infinite in the simulated system. The error between the peaks of each distribution is shown in Table 4.2. Note that the deviation of the peak from the ideal solution is greatly reduced in the population density estimate compared to the analytical value, and that the peaks of the density function are noticeably sharper, reducing uncertainty in fitting the peak in a noisy environment. In an ideal system, with no error from windowing, noise, or deviations from the prototype function used in the deconvolution, the population density function would appear as a series of real-valued delta functions at each resonance. However, due to the windowing and deconvolution mismatch, there will be a non-zero imaginary component which may be somewhat significant. Because of this, only the real components of the resultant population density are considered.

Table 4.2. Deviation between the peak of each distribution and the analytical value of each resonance frequency.

| Distribution | Frequency Deviation (Hz) | | |
|-------------------------|--------------------------|--------|--------|
| | Peak 1 | Peak 2 | Peak 3 |
| $Re[\rho(f)]$ | -1 | 0 | 0 |
| $\beta(f)$ | -4 | -8 | 11 |
| $\frac{V_f(f)}{V_0(f)}$ | -6 | -11 | 8 |

4.2.4 Windowing Effects

Because this methodology is limited to sampling over a finite window, there will be some amount of distortion in the measurement caused by truncating the system's response, particularly when the acquisition window is relatively short. This effect can be alleviated by continuing the acquisition beyond the system's settling time to capture the truncated components of the signal; however, this was found to be unnecessary in this work. The resonators used in this work have a settling time on

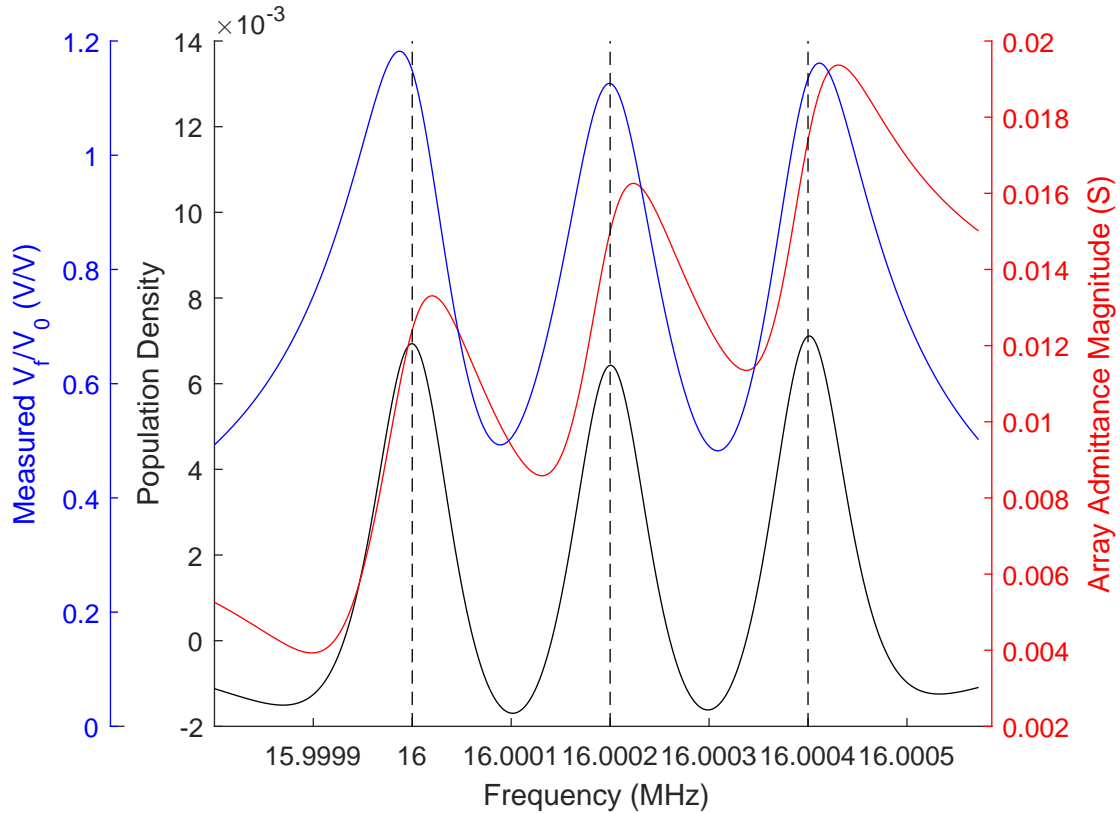


Figure 4.6. Comparison between peak locations between the deconvolved solution, $Re[\rho(f)]$, the calculated admittance, $\beta(f)$, and the spectral output, $\frac{V_f(f)}{V_0(f)}$.

the order of 1-2 ms, or about 0.1-0.2% of the acquisition period, which minimized this effect to a negligible level. Figure 4.7 demonstrates this effect by examining the spectral response of a sample system over several acquisition windows, ranging from 0.1 s to 100 s. A 1 Hz moving average filter was applied to the frequency responses of the 10 s and 100 s cases to improve legibility in the figure, due to the more densely sampled noise processes making these cases appear more noisy than they actually are when rendered in a plot. As can be seen in the figure, the shortest acquisition period shows a mild discrepancy in its response relative to the others. However, at and above the 1 s period, which was the configuration used in this work, the methodology yields consistent results.

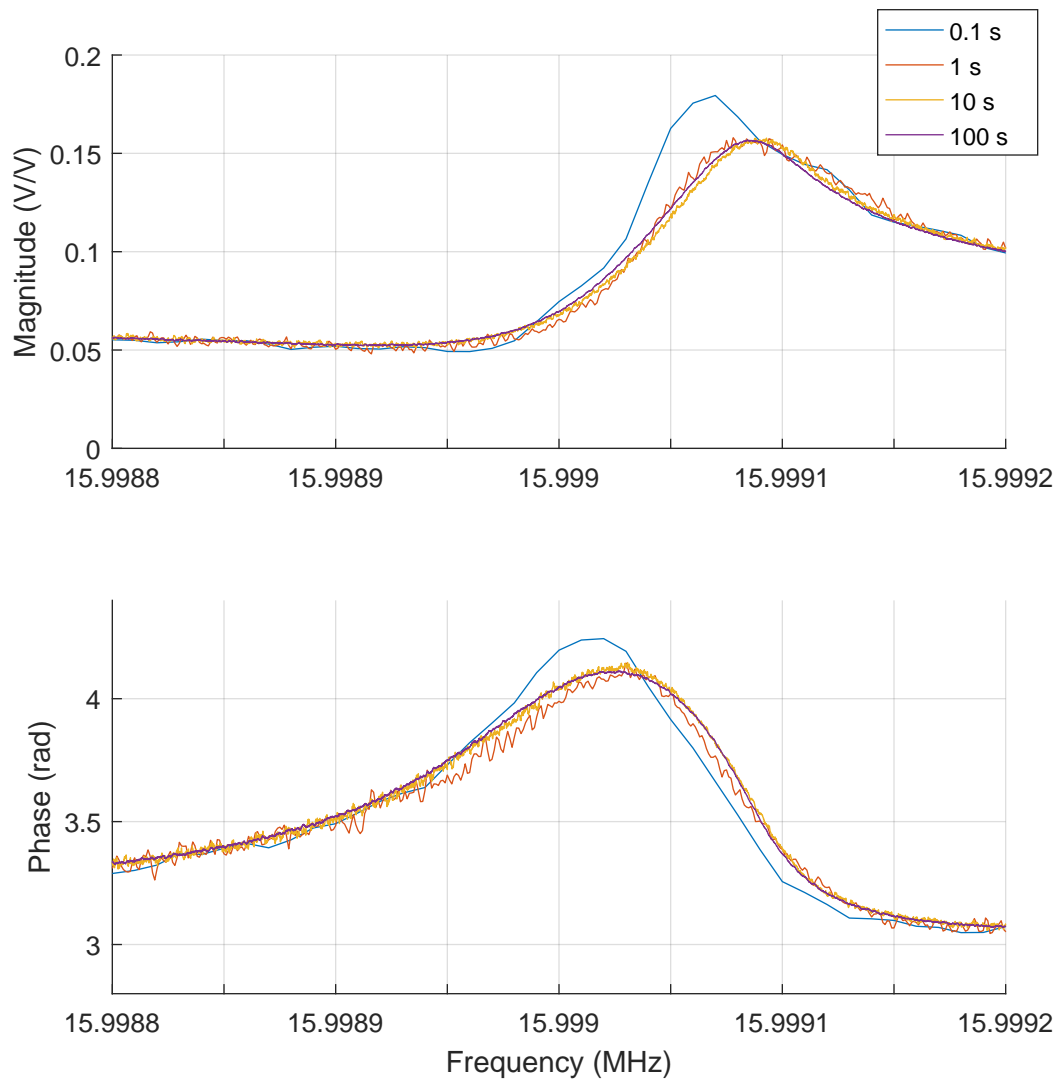


Figure 4.7. Comparison between varying acquisition periods showing the distortion due to truncating the system response to the input.

4.2.5 Noise Considerations

Due to the sensitivity to noise of the deconvolution process outlined in Section 4.2.3, it may be necessary in some applications to take additional measures to improve the signal-to-noise ratio in the system. The principle factors responsible for noise

error in these measurements can be divided between two main sources: constraints on the power spectral density of the input excitation, and losses in signal return for measurements of the V_0 spectrum caused by the presence of parasitic elements (i.e. C_0).

The first of these factors is due to the fact that the total energy of the input signal is constrained by the limitations on the amplifiers driving the board in combination with the finite sampling window, as well as the fact that this energy is then divided over a frequency band. Specifically, given a maximum input amplitude of A , a modulation depth of δ_f , and a modulation (and measurement) period of T , then the total energy of the input signal (assuming $T \gg \frac{2\pi}{\Omega}$) can be approximated by:

$$E \approx \int_0^T [A \cos(\Omega t)]^2 dt = \frac{A^2 T}{2}, \quad (4.16)$$

and the energy spectral density within the excitation frequency band, assuming that the excitation magnitude is nominally flat within this band, is approximately:

$$S_{xx}(f) \approx \frac{E}{2\delta_f} = \frac{A^2 T}{4\delta_f}. \quad (4.17)$$

This implies that the energy spectral density of the input signal (and therefore the signal-to-noise ratio) is directly proportional to the measurement period, and inversely proportional to the width of the frequency band being excited. The practical implications of this on the noise characteristics of the system are that the wider the frequency band that the resonators populate is, and the shorter the acquisition window, the lower the resultant signal-to-noise ratio will be.

The second factor affecting the noise performance of the system is the parasitic capacitance, C_0 . As shown in Equation 4.7, the amplitude of the spectral response, $\frac{V_0}{V_f}$, is proportional to a factor of $\frac{C_c}{C_c + C_0}$. For the system being examined in this work, this corresponds to a factor of 4.17x loss in amplitude, and a 17.4x loss in signal power. One means of correcting for this error is to add an inductive element in parallel with C_0 which has been tuned to form a band stop filter in the vicinity of the natural frequencies of the resonators. Applying this change alters Equation 4.7 to become:

$$\frac{V_0(s)}{V_f(s)} = \frac{\frac{s^2 C_c L_0}{s^2 (C_0 + C_c) L_0 + 1} \prod_{j=1}^N L_{mj} s + R_{mj} + \frac{1}{s C_{mj}}}{\prod_{j=1}^N \left[L_{mj} s + R_{mj} + \frac{1}{s C_{mj}} \right] + \frac{s L_0}{s^2 (C_0 + C_c) L_0 + 1} \sum_{i=1}^N \prod_{j \neq i} \left[L_{mj} s + R_{mj} + \frac{1}{s C_{mj}} \right]}, \quad (4.18)$$

and the attenuating factor is now given by $\frac{s^2 C_c L_0}{s^2 (C_0 + C_c) L_0 + 1}$. By careful tuning of the inductive element, the denominator of this factor (and thus the signal loss) can be reduced significantly. However, care should be taken when employing this method to ensure that the resultant LC tank does not overload the other circuit elements.

4.2.6 Resonator Functionalization

The resonators in this work were divided into five functional material groups. The first group of resonators was left unfunctionalized to serve as a humidity and temperature reference. The remaining groups of resonators were functionalized with 1 μL of an ink from Table 4.3 using an auto-pipette. All of the substances, with the exception of the single walled carbon nanotubes (SWCNTs) were used as received from Sigma Aldrich. The SWCNTs were heated at 300 $^\circ\text{C}$ for 24 hr in open air conditions and subsequently treated with hydrochloric acid to remove impurities. Note that Group c was functionalized with 1 μL of the SWCNTs and 1 μL of the hydroxylamine hydrochloride (HHC1). Upon deposition, the resonators were stored in a vacuum oven for 24 hr to remove the remaining solvent.

4.2.7 Experimental Apparatus

The functionalized resonator board was secured to the instrumentation board and sealed in the 9.5 cm diameter chamber. Figure 4.8 shows a high-level diagram of the experimental apparatus. As shown in the figure, the chamber was placed in-line with a flow distribution system consisting of a series of mass flow controllers (MFC, MKS)

Table 4.3. Resonator groupings by functional material and solvent. Note: Group c was functionalized with 1 μL of single walled carbon nanotubes (SWCNTs) and 1 μL of hydroxylamine hydrochloride (HHCl).

| Group | Solute and Solvent | Concentration (mg/mL) |
|-------|-----------------------------------|--------------------------|
| a | polymethylmethacrylate in toluene | 1 |
| b | poly(5-carboxylindole) in ethanol | 1 |
| c | SWCNTs in tetrahydrofuran | 0.1 |
| | HHCl in methanol | 1 |
| d | poly(4-vinylpyridine) in ethanol | 1 |

and bubblers (Chem-glass) to achieve the desired analyte concentrations. In this work, a nitrogen source was connected to four parallel lines. The first line remained exclusively nitrogen to allow for chamber purging. The remaining three lines ran in parallel through a bubbler containing methanol, toluene, or xylene. The four lines met at a laminar manifold before entering the testing chamber. The data presented herein was collected at concentration ranges from 4,000 to 14,000 ppm at 150 ccm.

4.3 Results and Discussion

4.3.1 Resonator Selection

As mentioned in Section 4.2.1, the methodology used in this work requires that the resonators be separated in frequency so as to isolate their responses in the output. Unfortunately, because the resonators were nominally identical pre-functionalization, and due to the fact that the precise amount of material deposited during the functionalization process was not controlled, a number of resonators in the initial set of 16 had excessive overlap between their response bands. Additionally, the process of unsealing the crystals and the subsequent deposition process leaves some entirely non-

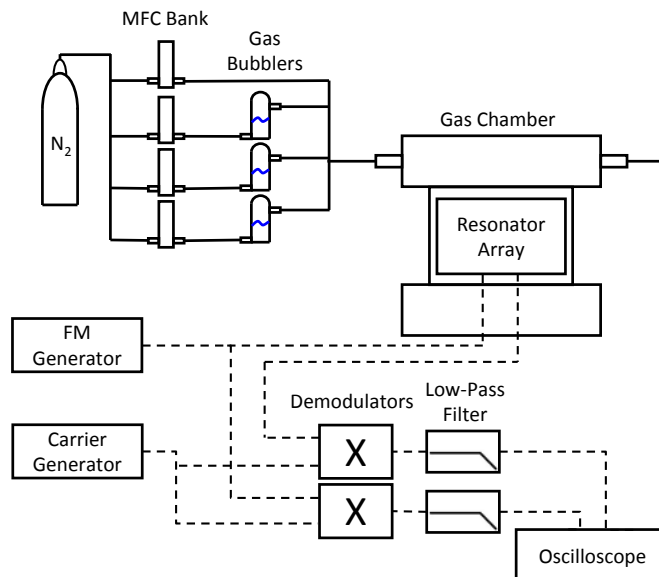


Figure 4.8. Layout of the chemical and electrical components of the experimental setup. Solid lines represent gas/vapor connections, and dashed lines represent electrical connections.

functional (in this case, a total of 3 resonators no longer had any significant dynamic response). Because of this, a subset of the initial set of resonators had to be selected for use in experiment, with the others disconnected via the array of switches shown in Figure 4.1.

In order to select the set of resonators to be used in experiment, each individual resonator's response was measured directly using an H2FLI lock-in amplifier from Zurich Instruments. From this response, the resonant frequency and bandwidth of each resonator was calculated. First, the subset of resonators that was entirely unresponsive was disconnected. For the remaining resonators, those whose bands overlapped were prioritized in terms of their quality factor. Where the difference in quality factor was not significant, manual substitutions were made to ensure that at least one resonator of each functional chemistry was present in the final population. The minimum frequency spacing between any two resonators was considered to be approximately two bandwidths. Table 4.4 shows which of the 16 resonators were ultimately retained,

along with their individually characterized resonant frequency, bandwidth, quality factor, and the functional chemistry deposited.

Table 4.4. A list of the resonators which were retained post-functionalization. These resonators have a sufficiently high quality factor and frequency separation to be observable in the common node spectrum.

| Resonator | Chemistry | f_r (MHz) | -3 dB BW (Hz) | Q |
|-----------|----------------------------|-------------|---------------|--------|
| 1 | SWCNT with HHCl | 15.991008 | 538 | 29723 |
| 2 | Poly(4-vinylpyridine) | 15.994931 | 155 | 103193 |
| 3 | Poly(5-carboxylindole) | 15.995257 | 183 | 87406 |
| 4 | Poly(5-carboxylindole) | 15.995930 | 120 | 133299 |
| 5 | Poly(methyl methacrylate) | 15.996459 | 142 | 112651 |
| 6 | SWCNT with HHCl | 15.996766 | 137 | 116765 |
| 7 | Unfunctionalized reference | 15.997526 | 137 | 120282 |

4.3.2 Thermal Sensitivity

Because the resonators used in this device are mechanical in nature, their characteristics can be altered by changes in their environment. In some ways this is intended, as the nature of this work is to functionalize these resonators to respond to organic compounds in the air, but secondary environmental factors, such as temperature and humidity, can also lead to observable effects. Particularly with temperature, small thermal variations over time can increase or decrease the stiffness of the quartz crystal by a small, but measurable, amount. To quantify this effect, the system was placed in an enclosed box with a Pt1000 thermal probe. All of the resonators were disconnected except for a single unfunctionalized resonator. The resonator was uncapped and exposed to air for a 30 min period prior to the start of measurement to allow the resonator to reach steady state after breaking the hermetic seal of the

packaging. The temperature and resonance frequency were then monitored over the course of 48 hr. Figure 4.9 shows the drift in the frequency of the resonator as well as the temperature measurement over this period. The sensitivity was found to be approximately $-11 \frac{\text{Hz}}{^\circ\text{C}}$.

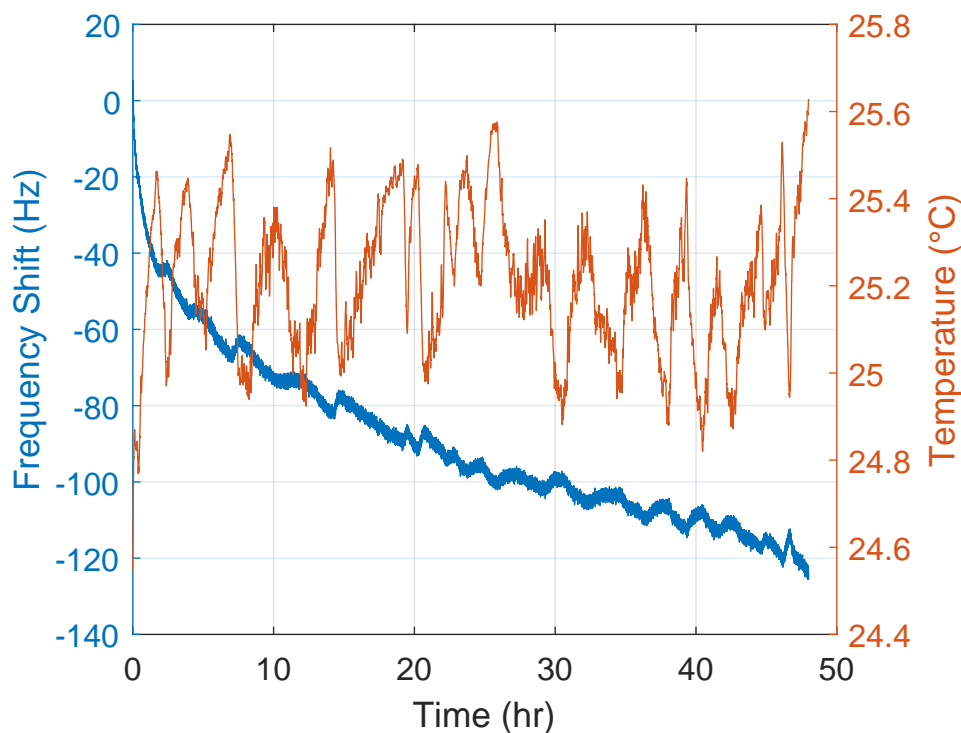


Figure 4.9. The change in resonator frequency and temperature over a period of 48 hr.

4.3.3 Non-Thermal Drift

The most prominent feature of the response shown in Figure 4.9 is the drift of approximately 120 Hz over the course of the experiment which is uncorrelated with the temperature. One possible explanation of this is the oxidation of the silver film coating the resonator crystal due to breaking the hermetic seal of the resonator and exposing it to air. As the surface oxidizes, the additional mass adds an inertial load

to the crystal lowering the resonant frequency in a similar manner to the sorbents used on the functionalized resonators. To test this theory, the oxidation process was artificially accelerated by exposing the crystal to a source of ozone (a handheld plasma wand from Plasma Etch) for varying exposure times. Figure 4.10 shows the drift of four resonators with varying exposure periods (no exposure, 1 min, 5 min, and 15 min) over a 48 hr period. The unexposed resonator behaves in a similar manner to that of the thermal sensitivity test, in that it shifts downward in frequency by approximately 120 Hz over 48 hr. The 15 min exposure time generates the opposite response, with the frequency rising rapidly over the course of 10 hr before stabilizing. This may be indicative of over-exposure to ozone forcing the silver on the surface to a higher oxidation state [i.e. silver (I,III) oxide], which then decays to the more stable silver (I) oxide on a slightly shorter timescale than the untreated resonator's oxidation. The 5 and 10 min exposure cases show responses which, while still drifting slightly, are much more stable compared to the extreme cases. This indicates that the mild exposure cases have passivated the silver surface, preventing the long-period drift from occurring. While this process is enlightening towards the source of the anomalous drift, it was not repeated for the resonators in the subsequent sections to avoid unintended chemical interactions with the deposited sorbents.

4.3.4 VOC Exposure Results

Figure 4.11 shows a sample spectral measurement for the coupled system. The locations of the antiresonances correlating to each of the retained resonators is shown in the amplitude plot, and the corresponding phase peaks are shown in the phase plot. The population density function, shown in Figure 4.12, was derived via the method previously described. In order to extract the natural frequencies of the resonators from this response, a quadratic regression was performed on the peaks of this population density function to track the drift of the resonators over time. These peak locations are indicated in the figure by dashed red lines. Figures 4.13 and 4.14 show the shifts

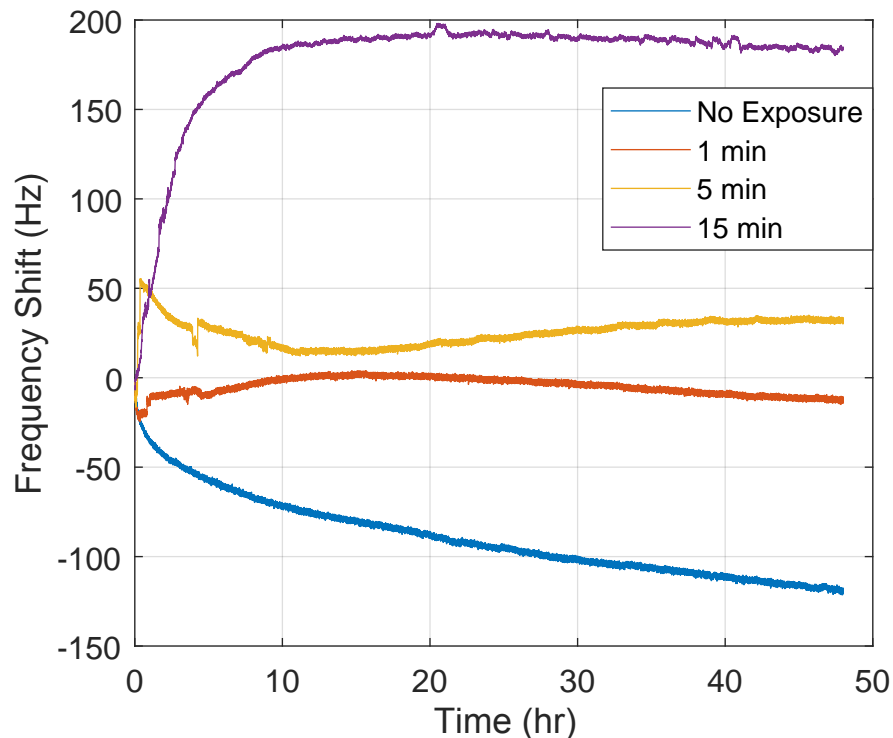


Figure 4.10. The change in resonator frequency over a period of 48 hr after varying exposure times to the plasma wand.

of each resonator as well as the concentration of each analyte throughout the duration of the test. The analytes were supplied in 20-min pulses in varying concentrations, starting with “pure” tests for single analytes and then moving on to combinations of analytes. After each pulse a 20-min period of pure nitrogen was applied to purge the chamber of the previous analyte. Each of the vertical grid lines on the plots separates these 20-min windows. For use with the regression model that will be developed in Section 4.3.5, the steady-state frequency of each resonator within each window was measured by averaging the frequency across the final 200 s of each 20-min period. The frequency shifts used in the model were then taken as the difference of these steady-state values. With a surface-level inspection of the figures, we can see that every resonator (including the unfunctionalized reference) clearly responded to the presence of every analyte, though some responded more strongly to certain

analytes than others. Additionally, the gradual downward trend which was observed previously is also observable in several of the plots; however, the magnitude of the drift is not consistent between them, possibly due to the deposited material shielding the underlying silver from atmospheric oxygen.

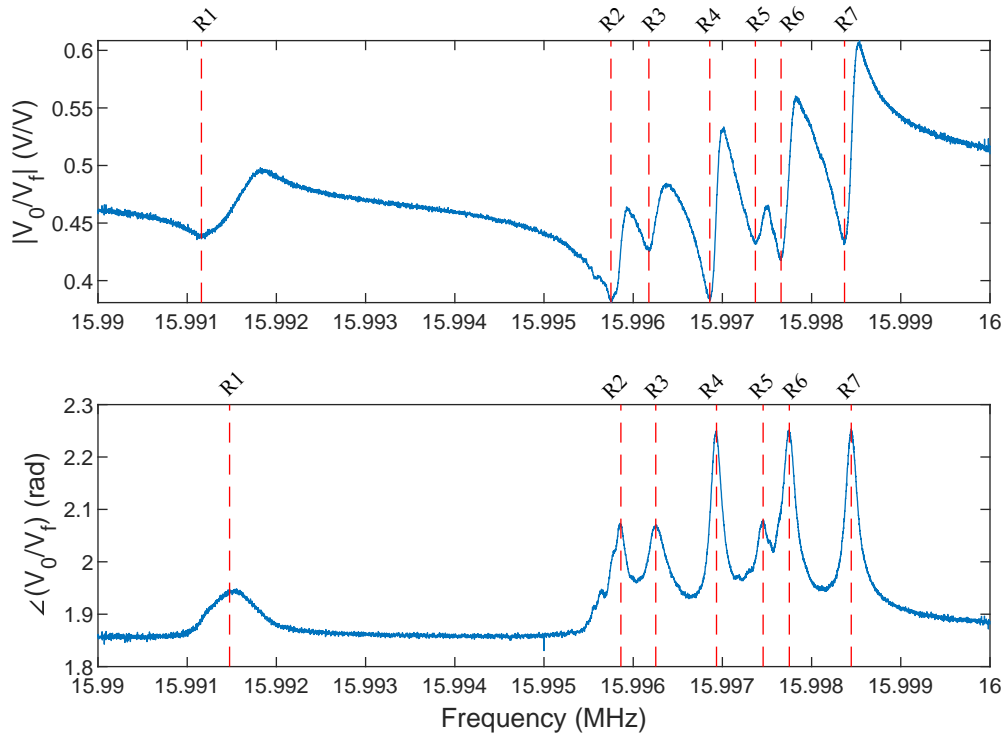


Figure 4.11. A sample output spectrum showing the distribution of resonator responses in a 10 kHz window. Each of the 7 antiresonances in the amplitude plot (and their associated peaks in the phase plot) correlate to the dynamics of a single resonator affecting the spectral response at the common node.

4.3.5 Sensitivity and Regression Model

The shifts in resonant frequency of each resonator with a distinct resonant peak were tracked through the aforementioned procedure. For a series of individual and

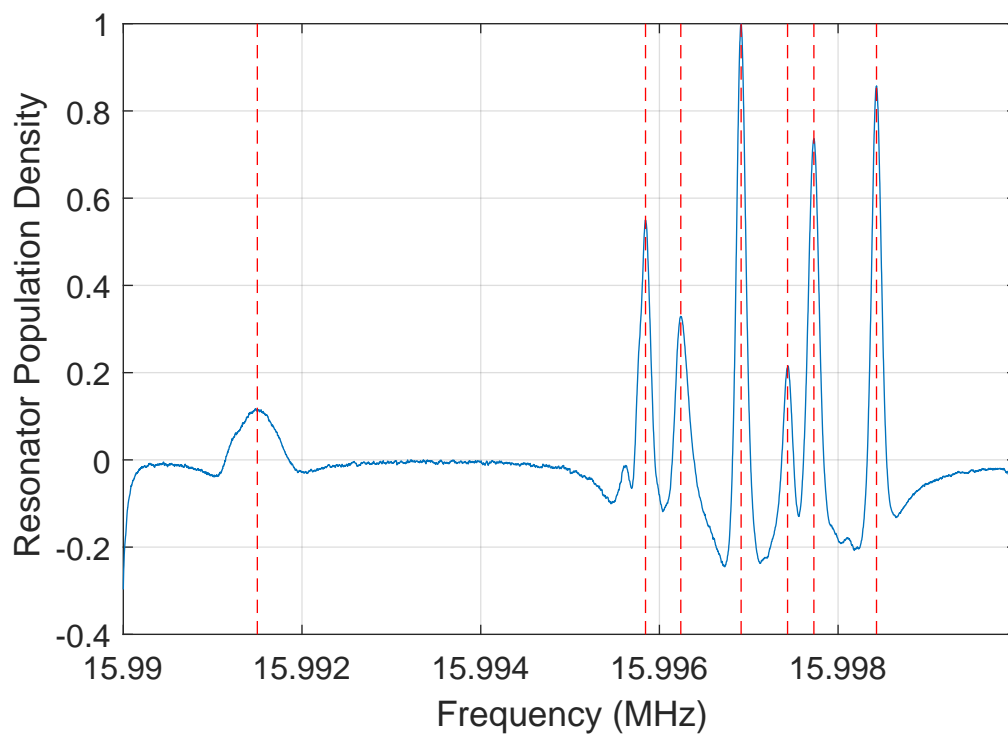


Figure 4.12. Derived population density function for the measured spectrum shown in Figure 4.11. The red dashed lines indicate the locations of the peaks in frequency.

combined methanol, toluene, and xylene exposures ranging from 4,000 to 14,000 ppm, the shift in frequency was recorded. For each resonator, i , a linear regression model was used of the form:

$$\delta\Omega_i - \delta\Omega_{ref} = p_0 + p_1M + p_2T + p_3X \quad (4.19)$$

where $\delta\Omega_i$ is the frequency shift of resonator i , $\delta\Omega_{ref}$ is the frequency shift of the unfunctionalized reference resonator, M is the methanol concentration (ppm), T is the toluene concentration (ppm), and X is the xylene concentration (ppm). The p_i coefficients and the correlation coefficient for each resonator group is reported in

Table 4.5. Higher-order terms and cross terms were not included in the final model due to their lack of statistical significance in predicting the frequency shift.

Table 4.5. The equation coefficients and correlation coefficients for the give ink groupings in which the group details can be located in Table 4.3.

| Resonator | Ink Group | p_0 | p_1 | p_2 | p_3 | R^2 |
|-----------|-----------|--------|-----------|-----------|-----------|-------|
| | | | 10^{-4} | 10^{-4} | 10^{-4} | |
| 1 | c | -6.63 | -6.99 | -0.36 | -3.05 | 0.696 |
| 2 | d | -10.23 | -11.15 | -1.03 | 3.85 | 0.913 |
| 3 | b | -9.03 | -4.65 | -2.34 | -3.60 | 0.845 |
| 4 | b | -7.33 | -4.65 | -1.18 | -0.53 | 0.885 |
| 5 | a | -14.00 | -3.77 | -0.43 | -6.85 | 0.278 |
| 6 | c | -8.38 | 1.10 | -2.14 | -4.06 | 0.697 |

Table 4.5 details the coefficients for the linear regression relationship between frequency shift and analyte concentration. It can be interpreted that Groups b, c, and d, namely resonators functionalized with poly(5-carboxylindole), SWCNTs and HHCl, and poly(4-vinylpyridine) produced the best model fit. This is supported by noting that these channels had unique responses to the analytes of interest. Group a, functionalized with polymethylmethacrylate, has a very poor fit with an $R^2 = 0.28$. This suggests two possible conclusions. First, polymethylmethacrylate is a poor receptor to methanol, toluene, and xylene. Second, the response curve for Resonator 5 with polymethylmethacrylate, shown in Figure 4.14, is not conducive to consistent shift measurements due to significant noise and intermittent connection faults. Ultimately, this approach allowed for a prediction of the shift in frequency when methanol, toluene, or xylene was present.

Based on these results, it appears that Group d has the highest sensitivity to (and relative selectivity towards) methanol vapor. Group b shows a lower degree of sensitivity to methanol relative to Group d, and appears to be somewhat less selective

towards a particular analyte. Additionally, the two resonators with this functional chemistry showed different sensitivities towards toluene and xylene, though similar sensitivities towards methanol. This may indicate that variations in the functionalization or testing processes is causing variations in the sensitivities to each analyte. A similar effect is visible in the case of Group c, which showed an even wider discrepancy. Finally, Group a showed the highest sensitivity to xylene vapor and the lowest to toluene, though the results of this particular chemistry were likely skewed due to the poor performance of Resonator 6's fit.

4.4 Conclusions

This work demonstrated a proof-of-concept for a high-throughput, multi-analyte resonant mass sensor for volatile organic compound sensing. This was achieved by leveraging the emergent dynamics in a coupled resonant system to create a single-input, single-output system capable of measuring the frequency shifts in multiple resonant elements simultaneously. It was found that the system generally performed well, with the exception of one of the four chemistries which were used in the functionalization of the resonators. Due to the varying sensitivities of each of these chemistries to each analyte, the procedure outlined in this work to estimate these sensitivities can be inverted, providing an estimate of the analyte concentrations based on direct measurements of the shifts in the resonators. Ongoing efforts are focused on improving the performance of this device, including investigating the cause of the slow frequency drift which was identified even in the reference channel. Additionally, more functional chemistries will be investigated which may be compatible with this device. Finally, improvements to the functionalization process will be investigated in an attempt to more precisely control the frequency separation of the resonators, allowing larger arrays to be used in future works.

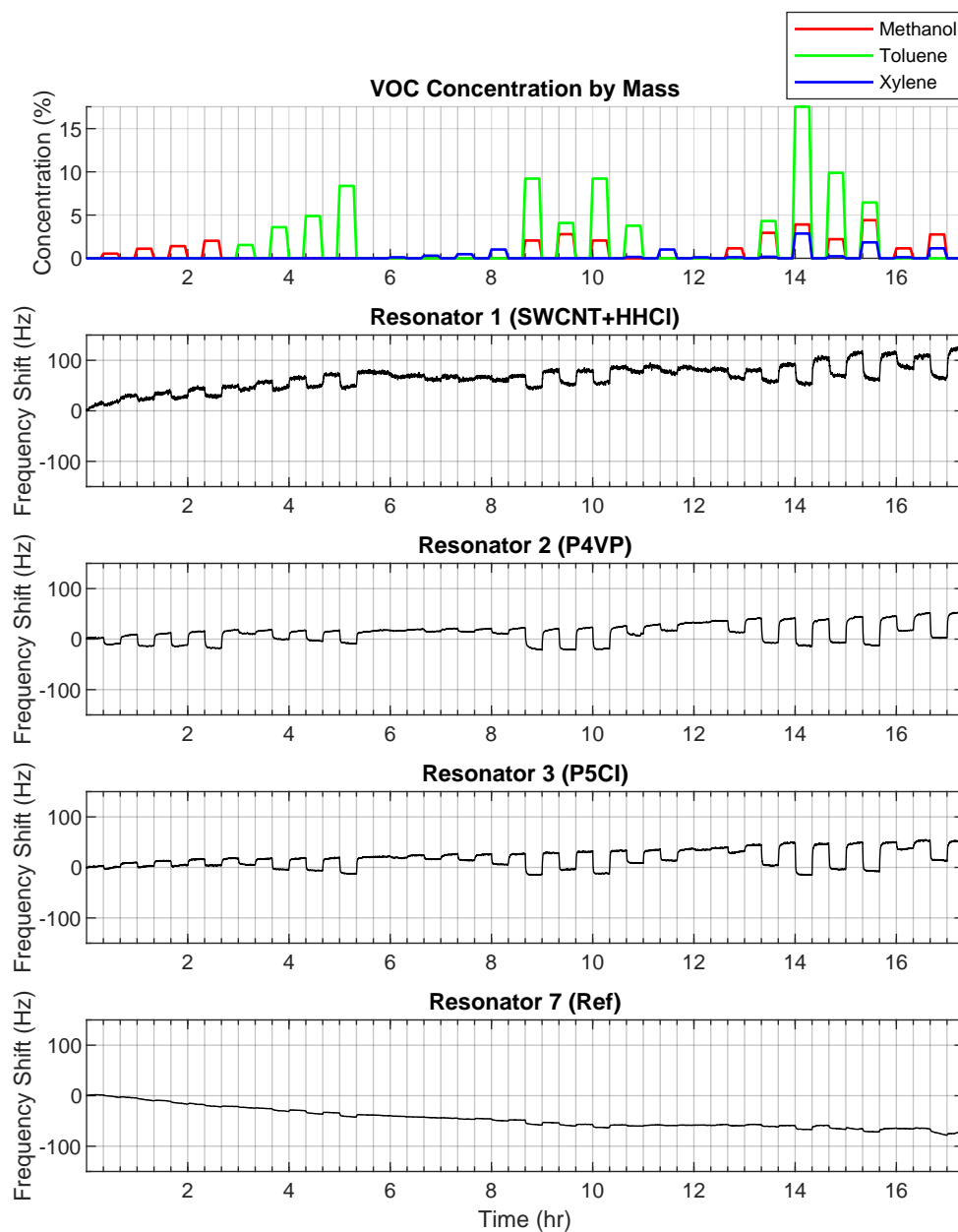


Figure 4.13. Frequency shift in resonators 1-3 over time. The top-most plot shows the concentration of the analytes in the chamber over the same time period, and the bottom plot shows the drift in the reference channel. The vertical grid lines separate the 20-min periods corresponding to pulses in analyte concentration.

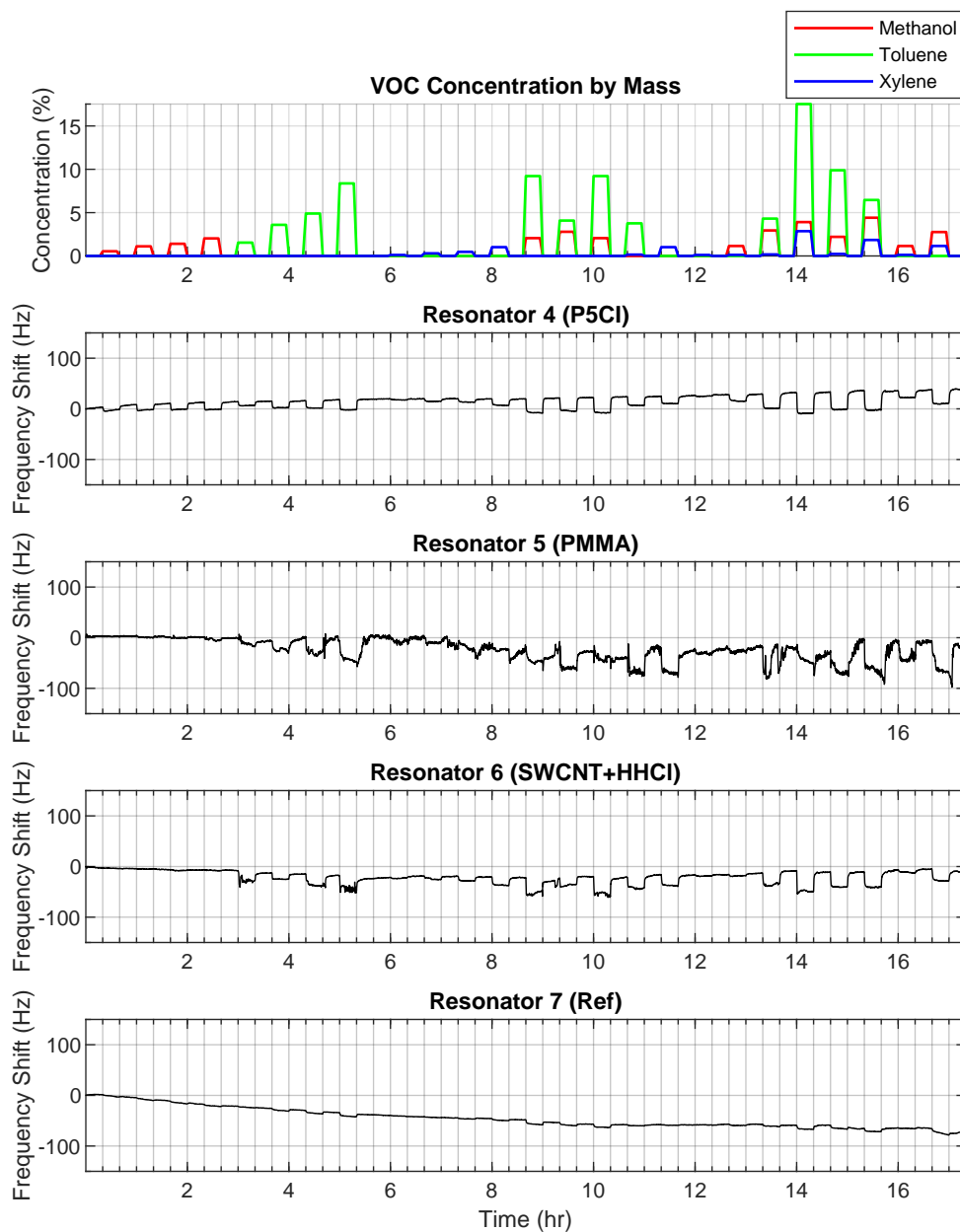


Figure 4.14. Frequency shift in resonators 4-6 over time. The top-most plot shows the concentration of the analytes in the chamber over the same time period, and the bottom plot shows the drift in the reference channel. The vertical grid lines separate the 20-min periods corresponding to pulses in analyte concentration.

5. COLOR RECOGNITION VIA A NETWORK OF COUPLED OSCILLATORS

5.1 Motivation

As previously noted, coupled oscillator networks can exhibit a variety of dynamical behaviors which make them feasible for use in a number of applications, such as energy harvesting [10, 12], signal processing [5, 6], and, of particular interest here, analog computing [72–77, 89, 90].

The emergent dynamics in a network of coupled oscillators can be made to emulate the behavior of neurons within neural networks. Typically, these behaviors include dynamics such as synchronization within subsets of the oscillator network, either through frequency or phase locking, and information within the networks can be encoded by tuning the internal parameters of the constituent oscillators or the coupling paths between them [91]. Among the earlier theoretical works in the field of neuromorphic computing which exploited these behaviors were the works by Hoppensteadt and Izhikevich, in which the authors developed analytical techniques for exploiting coupled oscillator networks ranging from providing systems with associative memory to pattern recognition [72, 92, 93]. Since then, these techniques have been further refined to provide for more advanced image filtering across a variety of different oscillator topologies. See, for example, the works of Nikonov et al. on the subjects of oscillator-based convolutional neural networks and memory operations towards image processing and pattern recognition [73, 74].

For many topologies, the system’s behavior can be modeled by leveraging certain symmetries (i.e. nearly-identical oscillators, symmetric, weak, or all-to-all coupling) to derive phase-only models, such as the Kuramoto model [69]. However, the subject of much contemporary study are systems in which the phase dynamics cannot be

separated from the amplitude dynamics, disallowing the use of these types of models. See, for example, the work done by Kumar and Mohanty in [94], in which the authors simulate the dynamics of a network of coupled Van der Pol Duffing oscillators, which exhibit strongly coupled amplitude and phase dynamics, and achieve auto-associative memory operation in simulation.

Other contemporary research has focused on developing physical realizations of these types of devices. Much of this has been driven by the advent of micro- and nano-electromechanical systems (MEMS/NEMS) which provide for high-quality and small-footprint resonant and electrical elements [14, 20–25, 95] due to the implicit scalability afforded by these types of devices allowing for very large networks of high-quality oscillators to be fabricated on on-chip. A number of oscillator topologies have been demonstrated experimentally, including spintronic oscillator networks [77, 96], drumhead resonators [97], and Colpitts oscillators [98].

In this work, we will be examining a system of 3 globally coupled Colpitts oscillators, similar to those shown in [98], and exploiting their dynamics to provide a threshold color sensor. In particular, the frequency-locking behaviors of the oscillators in the system are coupled to the color content of incident light by the use of color-filtered photo-resistive coupling paths. By examining the frequency spectrum of the voltage at a common coupling node, it is possible to extract information about the synchronization state of the oscillators. Since this state is directly related to the light intensity levels in each color band, it is then possible to map this state to a region in color space, effectively making the system a threshold color sensor, which is analogous to a single color pixel input for a pattern recognition system.

5.2 Background

5.2.1 Colpitts Oscillators

Figure 5.1 shows the circuit diagram for the Colpitts oscillators used in this work, which are similar to those shown in [99]. Colpitts oscillators exhibit three behaviors which may be useful for color recognition: injection pulling, in which two or more oscillators with different natural frequencies will begin to shift towards one another when coupled (generating a number of sideband frequencies in the process); injection locking [100], in which the oscillators will be pulled to the point of locking at the same frequency given a sufficiently strong coupling path; and phase locking [76], which occurs gradually in frequency-locked oscillators as the coupling strength is increased further beyond the frequency-locking threshold. In this work, we will primarily focus on the effects of frequency-locking, as the associated dynamics are easier to observe from a single point of measurement.

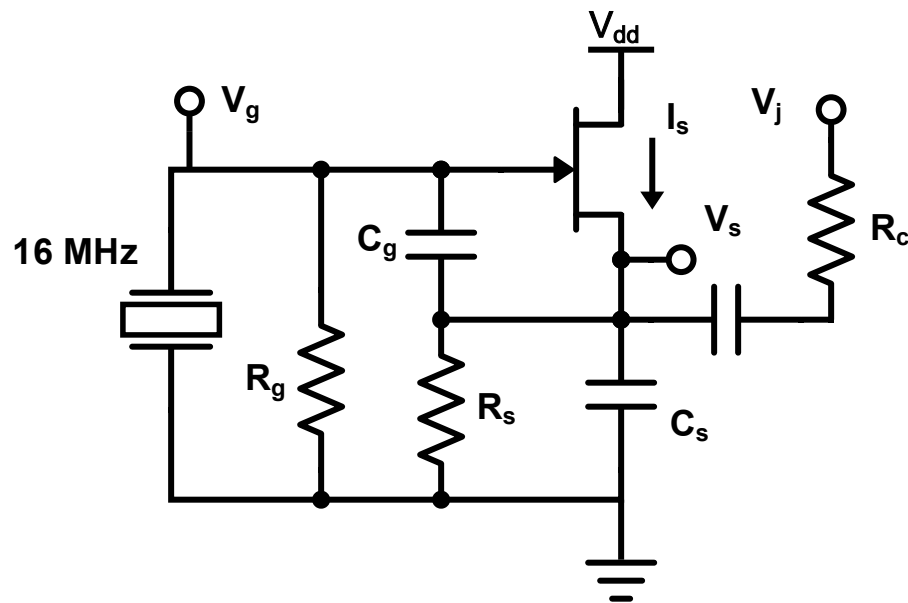


Figure 5.1. Circuit diagram for a single Colpitts oscillator.

5.3 Analysis

Prior to the experimental examination of a coupled system, we will begin with an analysis of the steady-state behavior, and particularly the frequency-locking behavior, of a single oscillator system in response an injected signal V_j , as shown in Figure 5.1. Note that, due to the dynamics of the transistor, this system is strongly nonlinear and exhibits significant coupling between its amplitude and phase dynamics, which can complicate the analysis, particularly when the dynamics of multiple coupled oscillators are considered. Because of this modeling difficulty for coupled systems, the analysis will instead focus on describing a single oscillator's behavior and identifying the dependence of its dynamics on the internal parameters. This analysis is intended as a stepping stone towards encoding specific patterns or information within this type of network, which is a necessary prerequisite to establish a pattern recognition scheme.

5.3.1 Equations of Motion

For the oscillator circuit shown in Figure 5.1, the equations of motion can be derived via nodal analysis:

$$\begin{aligned} L_m \ddot{I}_c + R_m \dot{I}_c + \frac{1}{C_m} I_c &= \dot{V}_g, \\ C_g \dot{V}_g - C_g \dot{V}_s &= -\frac{1}{R_g} V_g - I_c, \\ C_g \dot{V}_g - (C_g + C_s) \dot{V}_s &= \frac{1}{R_s} V_s - I_s (V_g - V_s + V_{th}) - \frac{1}{R_c} (V_j - V_s), \end{aligned} \quad (5.1)$$

where I_c is the current passing through the resonator, V_g is the voltage at the gate of the transistor, V_s is the voltage at the source of the transistor, and I_j is the current injected through the coupling branch. Note that within this equation it is assumed that the capacitor in series with the coupling path is large enough that its contribution to the system dynamics is negligible. The low-frequency effects of this assumption will be addressed directly in subsequent analysis.

The FET used in this work was the ATF-35143 from Broadcom Limited. The source current, I_s can be approximated as a piecewise quadratic function from the Statz FET model [101] as:

$$I_s = \begin{cases} \frac{\beta(V_g - V_s + V_{th})^2}{1 - b(V_g - V_s + V_{th})} \approx G(V_g - V_s + V_{th})^2 & (V_g - V_s + V_{th}) \geq 0, \\ 0 & (V_g - V_s + V_{th}) \leq 0, \end{cases} \quad (5.2)$$

where G is a parameter which, for these particular devices, is approximately equal to 0.12 AV^{-2} . Note that the quadratic approximation used here implicitly assumes that the system is operating in a region such that $V_g - V_s + V_{th} \approx 0$. The other circuit parameters used within this work are given by Table 5.1, which are similar to the parameters of the oscillators demonstrated in [98]. Note that the value given for the resonator frequency is the nominal rated value, but this naturally varies within a range of approximately 200 Hz between devices.

Table 5.1. Nominal values of the circuit parameters shown in Figure 5.1.

| Parameter | Description | Value | Units |
|-----------|--|--------|------------|
| f_r | Resonator natural frequency | 16 | MHz |
| Q | Resonator quality factor | 102000 | |
| R_m | Resonator equivalent series resistance | 100 | Ω |
| L_m | Resonator motional inductance | 101.46 | mH |
| C_m | Resonator motional capacitance | 975.14 | aF |
| C_s | Source-Ground capacitance | 15 | pF |
| C_g | Gate-Source capacitance | 24 | pF |
| R_s | Source-Ground resistance | 7.5 | k Ω |
| R_g | Gate-Ground resistance | 50.8 | k Ω |

5.3.2 Nondimensionalization

In order to reduce the number of parameters within the problem, the system equations will be nondimensionalized. First, introduce the normalization factors Π_V , Π_I , and Π_t , which have units of volts, amperes, and seconds, respectively. Let the state variables be related to their nondimensional counterparts by:

$$\begin{aligned} V_g &= \Pi_V v, \\ V_s &= \Pi_V u, \\ V_j &= \Pi_V v_j, \\ I_c &= \Pi_I i_c, \\ \frac{d}{dt} &= \frac{1}{\Pi_t} \frac{d}{d\tau}, \end{aligned} \tag{5.3}$$

where v , u , i_c , and τ are the nondimensional gate voltage, source voltage, crystal current, and time, respectively. Additionally, let:

$$\begin{aligned} I_s &= \begin{cases} G\Pi_V^2(v - u - \frac{V_{th}}{\Pi_V})^2 & (v - u + \frac{V_{th}}{\Pi_V}) \geq 0, \\ 0 & (v - u + \frac{V_{th}}{\Pi_V}) \leq 0, \end{cases} \\ &= G\Pi_V^2 i_s (v - u + \frac{V_{th}}{\Pi_V}), \end{aligned} \tag{5.4}$$

where i_s represents the nondimensional source current, in terms of the nondimensional parameter given by $v - u + \frac{V_{th}}{\Pi_V}$. The equations of motion then become:

$$\frac{\Pi_V}{\Pi_t} v' = L_m \frac{\Pi_I}{\Pi_t^2} i_c'' + R_m \frac{\Pi_I}{\Pi_t} i_c' + \frac{1}{C_m} \Pi_I i_c, \tag{5.5}$$

$$C_g \frac{\Pi_V}{\Pi_t} (v' - u') = -\frac{1}{R_g} \Pi_V v - \Pi_I i_c, \tag{5.6}$$

$$C_g \frac{\Pi_V}{\Pi_t} v' - (C_g + C_s) \frac{\Pi_V}{\Pi_t} u' = \frac{1}{R_s} \Pi_V u - G\Pi_V^2 i_s \left(v - u + \frac{V_{th}}{\Pi_V} \right) - \frac{\Pi_V}{R_c} (v_j - u). \tag{5.7}$$

Simplifying the equations yields:

$$\frac{\Pi_V \Pi_t}{L_m \Pi_I} v' = i_c'' + \frac{R_m}{L_m} \Pi_t i_c' + \frac{1}{L_m C_m} \Pi_t^2 i_c, \tag{5.8}$$

$$v' - u' = -\frac{1}{C_g R_g} \Pi_t v - \frac{1}{C_g} \frac{\Pi_I \Pi_t}{\Pi_V} i_c, \quad (5.9)$$

$$v' - \frac{C_g + C_s}{C_g} u' = \frac{1}{C_g R_s} \Pi_t u - \frac{G}{C_g} \Pi_V \Pi_t i_s \left(v - u + \frac{V_{th}}{\Pi_V} \right) - \frac{\Pi_t}{C_g R_c} (v_j - u). \quad (5.10)$$

Next, we assign the previously undefined normalization parameters in terms of the circuit parameters as follows:

$$\Pi_V = V_{th}, \quad (5.11)$$

$$\Pi_I = V_{th} \sqrt{\frac{C_g}{L_m}}, \quad (5.12)$$

$$\Pi_t = \sqrt{L_m C_m}, \quad (5.13)$$

giving:

$$\sqrt{\frac{C_m}{C_g}} v' = i_c'' + R_m \sqrt{\frac{C_m}{L_m}} i_c' + i_c, \quad (5.14)$$

$$v' - u' = -\frac{\sqrt{L_m C_m}}{C_g R_g} v - \sqrt{\frac{C_m}{C_g}} i_c, \quad (5.15)$$

$$v' - \frac{C_g + C_s}{C_g} u' = \frac{\sqrt{L_m C_m}}{C_g R_s} u - \frac{G V_{th} \sqrt{L_m C_m}}{C_g} i_s (v - u + 1) - \frac{\sqrt{L_m C_m}}{C_g R_c} (v_j - u). \quad (5.16)$$

Finally, define the nondimensional parameters defining the system dynamics as:

$$\begin{aligned} \epsilon &= \sqrt{\frac{C_m}{C_g}}, & \alpha_1 &= \frac{\sqrt{L_m C_m}}{C_g R_g}, \\ \mu &= \frac{C_g + C_s}{C_g}, & \alpha_2 &= \frac{\sqrt{L_m C_m}}{C_g R_s}, \\ \lambda &= \frac{R_m C_g}{\sqrt{L_m C_m}}, & \gamma &= \frac{G V_{th} \sqrt{L_m C_m}}{C_g}, \\ \rho &= \frac{\sqrt{L_m C_m}}{C_g R_c}. \end{aligned} \quad (5.17)$$

The values of these nondimensional parameters are shown in Table 5.2. By substituting these parameters into the equations of motion, the nondimensional equations may be represented as:

$$\epsilon v' = i_c'' + \epsilon^2 \lambda i_c' + i_c, \quad (5.18)$$

$$v' - u' = -\alpha_1 v - \epsilon i_c, \quad (5.19)$$

$$v' - \mu u' = \alpha_2 u - \gamma i_s (v - u + 1) - \rho (v_j - u). \quad (5.20)$$

Table 5.2. Nominal values of the nondimensional circuit parameters. Note that the arbitrary parameters ρ and v_j are left undefined.

| Parameter | Value |
|------------|--------------------------|
| ϵ | 6.348×10^{-3} |
| μ | 1.623 |
| λ | 0.2433 |
| α_1 | 8.087×10^{-3} |
| α_2 | 55.10×10^{-3} |
| γ | 46.86 |
| Π_V | 0.95 V |
| Π_I | 1.467×10^{-5} A |
| Π_t | 9.947×10^{-9} s |

As a final simplifying measure, define a new state variable, w , as:

$$w = v - u + 1, \quad (5.21)$$

which represents the nondimensional activation voltage of the transistor. Substituting this variable in place of v allows the nonlinear drain current term to be represented in terms of a single dynamic variable:

$$\epsilon(u' + w') = i_c'' + \epsilon^2 \lambda i_c' + i_c, \quad (5.22)$$

$$w' = -\alpha_1(w + u - 1) - \epsilon i_c, \quad (5.23)$$

$$w' + (1 - \mu)u' = \alpha_2 u + \rho u - \rho v_j - \gamma i_s(w). \quad (5.24)$$

5.3.3 Harmonic Analysis: Single Oscillator

Because the oscillator being examined shows evidence of strong amplitude dynamics, ordinary methods of analysis such as a reduction to a phase-only model is likely unable to accurately model its behavior. Instead, we will approximate the system's steady-state response using a first-order harmonic approximation. We begin by lumping the linear components in the equations of motion into a series of transfer functions relating each independent variable. In the Laplace domain, the equations of motion become:

$$i_c = \frac{\epsilon s(w + u)}{s^2 + \epsilon^2 \lambda s + 1}, \quad (5.25)$$

$$s w = -\alpha_1 \left(w + u - \frac{1}{s} \right) - \epsilon i_c, \quad (5.26)$$

$$s w + [(1 - \mu)s - \alpha_2 - \rho]u = -\rho v_j - \gamma i_s(w). \quad (5.27)$$

Rearranging and eliminating i_c gives the following equations relating u , w , i_s , and v_j :

$$u = -\frac{(s^2 + \epsilon^2 \lambda s + 1)(\alpha_1 + s) + \epsilon^2 s}{\alpha_1(s^2 + \epsilon^2(\lambda + \frac{1}{\alpha_1})s + 1)} w + \frac{s^2 + \epsilon^2 \lambda s + 1}{s(s^2 + \epsilon^2(\lambda + \frac{1}{\alpha_1})s + 1)}, \quad (5.28)$$

$$\gamma i_s(w) = \left[-s + \frac{[(1-\mu)s - \alpha_2 - \rho][(s^2 + \epsilon^2\lambda s + 1)(\alpha_1 + s) + \epsilon^2 s]}{\alpha_1(s^2 + \epsilon^2(\lambda + \frac{1}{\alpha_1})s + 1)} \right] w - \rho v_j - \frac{[(1-\mu)s - \alpha_2 - \rho][s^2 + \epsilon^2\lambda s + 1]}{s(s^2 + \epsilon^2(\lambda + \frac{1}{\alpha_1})s + 1)}. \quad (5.29)$$

Note that the rightmost terms primarily model the system's startup dynamics. If we constrain the problem to steady-state operation, then by the Final Value Theorem these terms become constant in the time domain. Then, the equations above can be simplified as:

$$u = -\frac{(s^2 + \epsilon^2\lambda s + 1)(\alpha_1 + s) + \epsilon^2 s}{\alpha_1(s^2 + \epsilon^2(\lambda + \frac{1}{\alpha_1})s + 1)} w + \frac{1}{s}, \quad (5.30)$$

$$\gamma i_s = \left[-s + \frac{[(1-\mu)s - \alpha_2 - \rho][(s^2 + \epsilon^2\lambda s + 1)(\alpha_1 + s) + \epsilon^2 s]}{\alpha_1(s^2 + \epsilon^2(\lambda + \frac{1}{\alpha_1})s + 1)} \right] w - \rho v_j + \frac{\alpha_2 + \rho}{s}. \quad (5.31)$$

For brevity in subsequent sections, two transfer functions, $G(s)$ and $H(s)$ can be defined:

$$G(s) = -\frac{(s^2 + \epsilon^2\lambda s + 1)(\alpha_1 + s) + \epsilon^2 s}{\alpha_1(s^2 + \epsilon^2(\lambda + \frac{1}{\alpha_1})s + 1)}, \quad (5.32)$$

$$H(s) = -s + \frac{[(1-\mu)s - \alpha_2][(s^2 + \epsilon^2\lambda s + 1)(\alpha_1 + s) + \epsilon^2 s]}{\alpha_1(s^2 + \epsilon^2(\lambda + \frac{1}{\alpha_1})s + 1)}, \quad (5.33)$$

which allows the system equations to be reduced to:

$$u = G(s)w + \frac{1}{s}, \quad (5.34)$$

$$\gamma i_s = H(s)w + \rho G(s)w - \rho v_j + \frac{\alpha_2 + \rho}{s}. \quad (5.35)$$

Next, we assume that w can be described as:

$$w(t) = A_w \cos(\Omega t) + w_{dc}. \quad (5.36)$$

At first glance, this approximation may seem like a relatively poor model for a system with as strong a nonlinearity as appears in the FET current model. One may expect, correctly, that the piecewise-quadratic nonlinearity would generate a multitude of relatively strong harmonics that need to be accounted for. However, a key advantage to the use of w as a dynamic variable is that while u and v will have these secondary harmonics, they are largely rejected in w . Examining the frequency response of $\frac{1}{G(s)}$ will show that it's dominant behavior is to act as a high-Q bandpass filter from u to w , centered near the fundamental frequency. For example, for the given circuit parameters, the gain from u to w at the second harmonic is 48 dB below that of the first harmonic (see Figure 5.2). Because of this, the principle harmonic components of w will be the natural frequency of the resonator, and at very low (near-DC) frequencies.

DC Analysis

The relations between the DC components of the solution can be derived by taking the limit of Equations 5.34 and 5.35 as the frequency approaches zero. Note that the coupling conductance, ρ , is set to zero for this analysis to account for the high impedance of the coupling branch at low frequencies due to the large DC-blocking capacitance.

$$u_{dc} = G(0)w_{dc} + 1 = -w_{dc} + 1, \quad (5.37)$$

$$\gamma i_{sdc} = H(0)w_{dc} + \alpha_2 = \alpha_2(-w_{dc} + 1). \quad (5.38)$$

The value of i_{sdc} can be calculated by substituting Equation 5.36 into Equation 5.4 for the source current and averaging over a single period. Note, however, the implications that the approximation of w has for the source current, i_s :

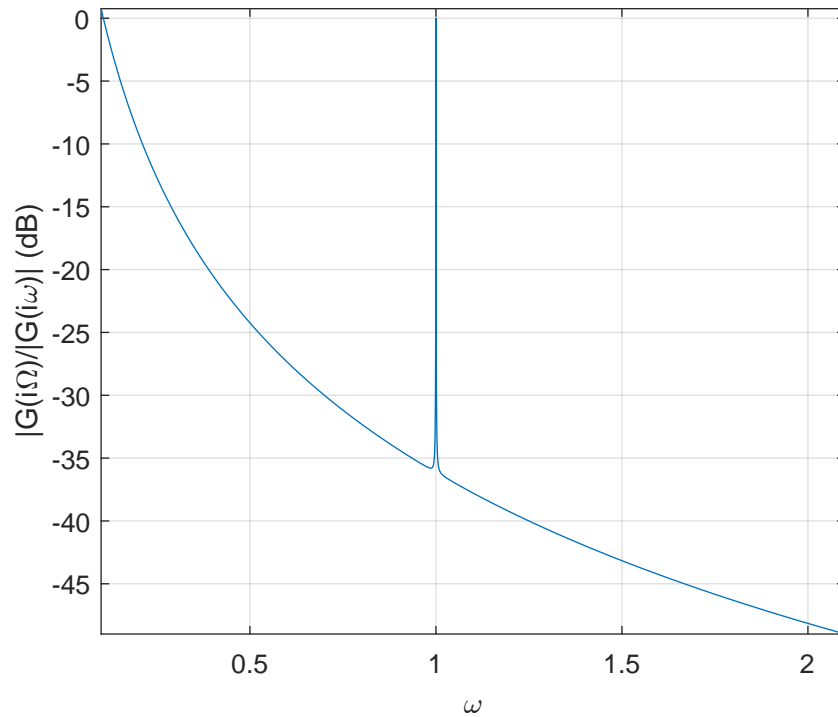


Figure 5.2. Magnitude of the inverse of the transfer function $G(s)$. Normalized by the magnitude at the fundamental frequency.

$$\gamma i_s = \begin{cases} \gamma w^2 & w \geq 0, \\ 0 & w \leq 0. \end{cases} \quad (5.39)$$

Because the source current is uniformly zero when $w \leq 0$, then, provided that $0 \leq -\frac{w_{dc}}{A_w} \leq 1$, i_s is only nonzero for the portion of an oscillation cycle given by $-t_0 \leq t \leq t_0$, where t_0 is:

$$t_0 = \frac{1}{\Omega} \arccos \left(-\frac{w_{dc}}{A_w} \right). \quad (5.40)$$

Then, i_{sdc} can be calculated as:

$$\begin{aligned}
\gamma i_{sdc} &= \frac{\gamma\Omega}{2\pi} \int_{-\frac{\pi}{\Omega}}^{\frac{\pi}{\Omega}} i_s dt = \frac{\gamma\Omega}{2\pi} \int_{-t_0}^{t_0} (w_{dc} + A_w \cos \Omega t)^2 dt \\
&= \frac{\gamma A_w^2}{2\pi} \left[\left(1 + 2 \frac{w_{dc}^2}{A_w^2}\right) \arccos \left(-\frac{w_{dc}}{A_w} \right) + 3 \frac{w_{dc}}{A_w} \sqrt{1 - \frac{w_{dc}^2}{A_w^2}} \right]. \quad (5.41)
\end{aligned}$$

AC Analysis

Because the FET model given by Equation 5.4 forces the source current i_s and w to be in-phase in steady-state operation, the oscillation frequency Ω for an oscillator with no external excitation (i.e. $v_j, \rho = 0$) can be calculated as the frequency which satisfies:

$$\angle H(i\Omega; 0) = 0. \quad (5.42)$$

For a system which is assumed to be frequency locked to the injected signal, the oscillation frequency will instead be a prescribed parameter of the system, and the phase angle ϕ between the injected signal v_j and w will become a variable to be solved. Converting Equation 5.35 to the time domain gives:

$$\gamma i_s(t) = |H(i\Omega)| A_w \cos[\Omega t + \angle H(i\Omega)] + \rho A_w |G(i\Omega)| \cos[\Omega t + \angle G(i\Omega)] - \rho v_j \cos(\Omega t + \phi). \quad (5.43)$$

To extract the first harmonic, multiply each side by $\frac{\Omega}{\pi} \cos[\Omega t + \angle H(i\Omega)]$ and integrate over a single period:

$$\begin{aligned}
\gamma i_{ac1} &= \frac{\gamma\Omega}{\pi} \int_{-\frac{\pi}{\Omega}}^{\frac{\pi}{\Omega}} i_s \cos[\Omega t + \angle H(i\Omega)] dt \\
&= \frac{\gamma\Omega}{\pi} \int_{-t_0}^{t_0} (w_{dc} + A_w \cos[\Omega t + \angle H(i\Omega)])^2 \cos[\Omega t + \angle H(i\Omega)] dt \\
&= \frac{2\gamma A_w^2}{3\pi} \left[3 \frac{w_{dc}}{A_w} \arccos \left(-\frac{w_{dc}}{A_w} \right) + \left(2 + \frac{w_{dc}^2}{A_w^2} \right) \sqrt{1 - \frac{w_{dc}^2}{A_w^2}} \right], \quad (5.44)
\end{aligned}$$

$$\begin{aligned}
\gamma i_{ac1} &= \frac{\Omega}{\pi} \int_{-\frac{\pi}{\Omega}}^{\frac{\pi}{\Omega}} \left[|H(i\Omega)| A_w \cos[\Omega t + \angle H(i\Omega)] \right. \\
&\quad \left. + \rho A_w |G(i\Omega)| \cos[\Omega t + \angle G(i\Omega)] - \rho v_j \cos(\Omega t + \phi) \right] \cos[\Omega t + \angle H(i\Omega)] dt \\
&= |H(i\Omega)| A_w + \rho |G(i\Omega)| A_w \cos(\angle H(i\Omega) - \angle G(i\Omega)) - \rho v_j \cos(\angle H(i\Omega) - \phi). \quad (5.45)
\end{aligned}$$

Repeat for $\frac{\Omega}{\pi} \sin[\Omega t + \angle H(i\Omega)]$:

$$\begin{aligned}
\gamma i_{ac2} &= \frac{\gamma \Omega}{\pi} \int_{-\frac{\pi}{\Omega}}^{\frac{\pi}{\Omega}} i_s \sin[\Omega t + \angle H(i\Omega)] dt \\
&= \int_{-t_0}^{t_0} (w_{dc} + A_w \cos[\Omega t + \angle H(i\Omega)])^2 \sin[\Omega t + \angle H(i\Omega)] dt \\
&= 0, \quad (5.46)
\end{aligned}$$

$$\begin{aligned}
\gamma i_{ac2} &= \frac{\Omega}{\pi} \int_{-\frac{\pi}{\Omega}}^{\frac{\pi}{\Omega}} \left[|H(i\Omega)| A_w \cos[\Omega t + \angle H(i\Omega)] \right. \\
&\quad \left. + \rho A_w |G(i\Omega)| \cos[\Omega t + \angle G(i\Omega)] - \rho v_j \cos(\Omega t + \phi) \right] \sin[\Omega t + \angle H(i\Omega)] dt \\
&= \rho A_w |G(i\Omega)| \sin(\angle H(i\Omega) - \angle G(i\Omega)) - \rho v_j \sin(\angle H(i\Omega) - \phi). \quad (5.47)
\end{aligned}$$

This final equation provides a constraint for the phase variable, ϕ :

$$\phi = \angle H(i\Omega) - \arcsin \left[\frac{A_w}{V_j} |G(i\Omega)| \sin(\angle H(i\Omega) - \angle G(i\Omega)) \right]. \quad (5.48)$$

The equations above can be solved numerically to give values of A_w , w_{dc} , $i_{ac} = i_{ac1}$, i_{dc} , and ϕ , which represent the steady-state dynamics of the system for a given excitation v_j and coupling coefficient ρ . Table 5.3 shows the steady-state solution with no external excitation (and with ρ set to zero to avoid loading the circuit). For the purpose of validating this solution, Figure 5.3 shows a comparison between the prescribed model and the experimentally measured value of w for a single oscillator. As can be seen in the figure, the model and experimental results are fairly well

matched despite a small amount of distortion visible at lower voltage levels. This distortion may be caused by higher-order harmonics which were neglected in the model, or by nonidealities introduced in the measurement circuit due to the output of the operational amplifiers measuring V_g and V_s approaching the limits of their voltage rails.

Table 5.3. Solution of the system equations with no signal injection at the natural frequency.

| Parameter | Value | Dimensional Value |
|-----------|-----------|-------------------|
| Ω | 1.0000542 | 16000867 Hz |
| A_w | 0.6726 | 0.6390 V |
| w_{dc} | -0.5421 | -0.5150 V |
| u_{ac} | 1.107 | 1.052 V |
| u_{dc} | 1.542 | 1.465 V |

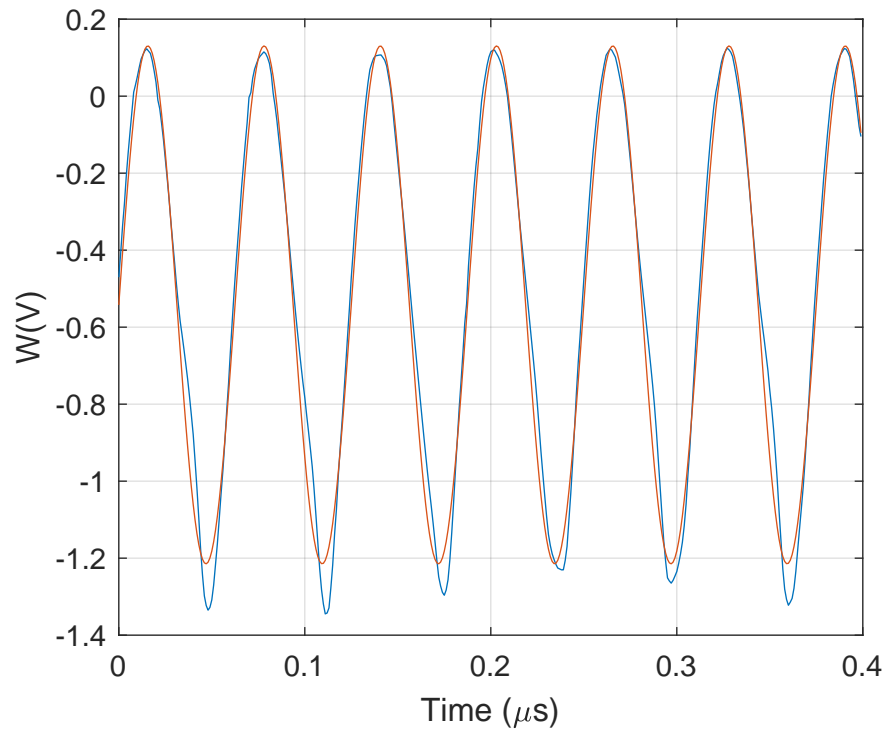


Figure 5.3. Comparison in the time domain between the model solution and an experimentally measured response.

5.3.4 Limitations of This Model

In this analysis, a number of assumptions are made which may or may not hold for the physical implementation, particularly under coupling conditions. The first is the assumption that w remains small enough that the quadratic approximation of the Statz transistor model remains valid. For a standalone oscillator with the prescribed parameters, this appears to be true based on the data shown in Figure 5.3, where the maximum value of w is around 0.1 V. Additionally, this model neglects non-fundamental harmonics. While this is somewhat justifiable by the argument proposed in Section 5.3.3, in the coupled system the injected signal will likely contain components which are somewhat close to the fundamental frequency, which would not be rejected. This means this model may not yield accurate results for a system which contains elements which are not locked to a singular frequency, unless the individual oscillators are sufficiently separated in frequency as to reject these components.

Another assumption of this model is that the system will eventually settle to steady-state operation. Again, this appears to be the case based on observation, but periodicity is not necessarily guaranteed in the coupled system, due to quasi-locking tendencies between the oscillators, which may be exacerbated by effects such as phase noise. Finally, this model assumes linearity in the circuit components aside from the transistor. This is likely a fair assumption for the elementary components, however the crystal resonators are known to have a Duffing-like hardening response under sufficient excitation amplitude, meaning that it is possible under sufficiently large oscillation amplitudes for bistable operation, or more exotic attractors, to appear in the circuit.

5.3.5 Parametric Study

In this section, the effects of variations in certain model parameters on the first-order harmonic solution will be examined. These results were obtained by numerically solving Equations 5.38, 5.41, 5.44, 5.45, 5.46, and 5.47. Except where specified, these solutions utilize the circuit parameters listed in Tables 5.1 and 5.2.

Variation in V_j

Figure 5.4 shows the simulated response of the system to various external forcing amplitudes. The upper-left plot shows the upper and lower bounds of the locking range as a function of the forcing amplitude. Outside of this range, the numerical solver was no longer able to find any physically valid solution to the equations, implying that the system has no stable frequency-locked solution outside of this envelope and may instead enter a quasi-locked regime with the excitation. The locking envelope shows a strong, approximately linear dependence on the amplitude of the excitation, widening significantly as the amplitude is increased.

The upper-right and lower plots show the dependence of the amplitude of w , and the amplitude and phase of the current injection as a function of the excitation frequency and amplitude. Among the salient features of this response is a strong dependence of the oscillation amplitude on the injection amplitude, with stronger excitations resulting in larger oscillations. Additionally, there is an asymmetry with respect to the injection frequency for the oscillation amplitude and injection current, with both increasing disproportionately at frequencies lower than the natural frequency than higher. This asymmetry is ultimately caused by a frequency mismatch between the $G(s)$ and $H(s)$ transfer functions, with $G(s)$ reaching a resonance several hundred Hz lower in frequency. Additionally, the coupling element in the circuit acts as a load on the circuit, even with no signal injection, contributing to this effect as well. Also visible is an inversion in the phase response of I_j as the excitation amplitude exceeds the value of u_{ac} .

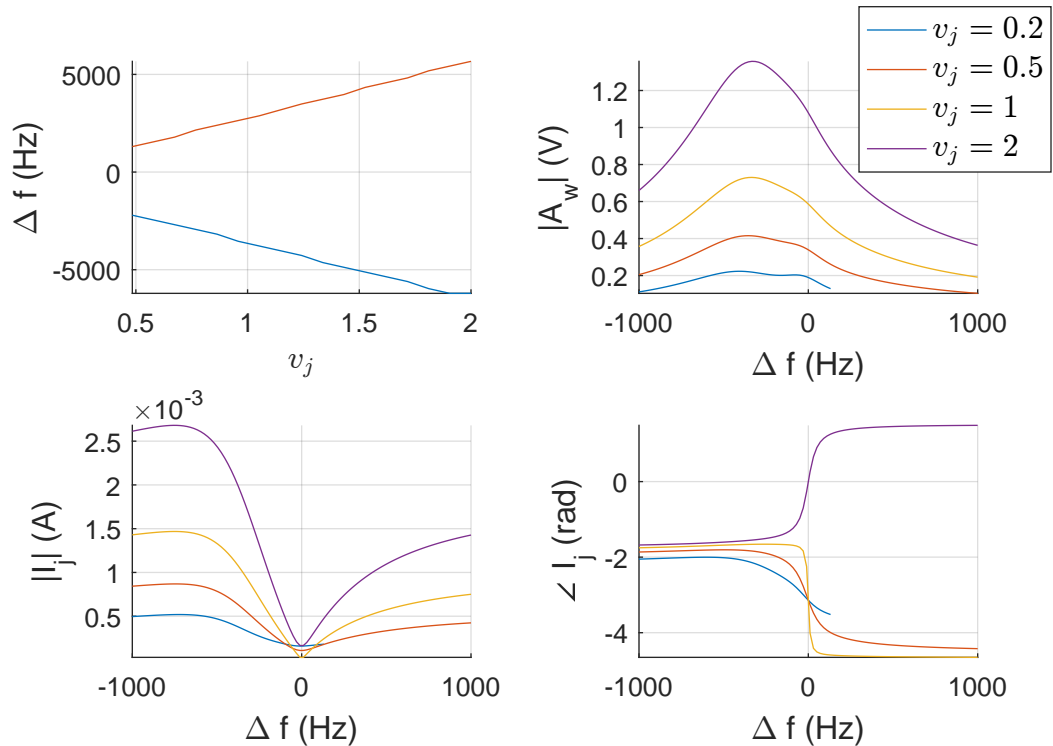


Figure 5.4. Change in the locking range and steady-state solution values with variation in v_j .

5.3.6 Variation in C_g

Figure 5.5 shows a similar diagram, varying the value of the source-gate capacitance, C_g . While the locking range does show some dependence on this parameter, the effect is less significant than in the previous case. Additionally, the oscillation amplitude appears to scale proportionally with the impedance of C_g , and the asymmetry about the 0 Hz datum is lessened as well as the impedance is increased. This provides a way to efficiently tune the amplitude of the oscillator by varying the value of this element. This could even be done dynamically by using a varactor diode in place of C_g and controlling the bias (and thus the oscillation amplitude) externally.

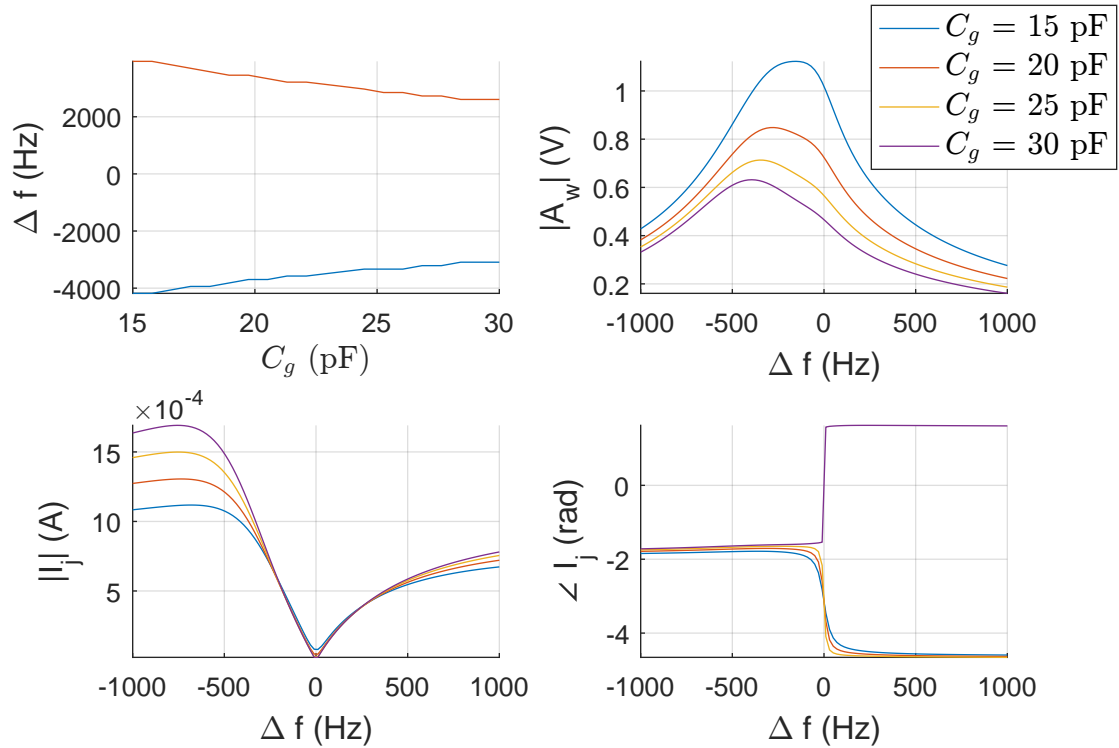


Figure 5.5. Change in the locking range and steady-state solution values with variation in C_g .

Variation in ρ

Like the previous case, the amplitude responses show a strong asymmetry across the frequency datum, which becomes more significant as the value of ρ increases. As this parameter increases, the peak amplitude shifts to a lower frequency, and increases in magnitude. Additionally, as the value of ρ is increased, it can be seen that the locking range expands as well. From this response, it can be inferred that an increase in the coupling strength between coupled oscillators will correlate with an increased tolerance of higher frequency separation.

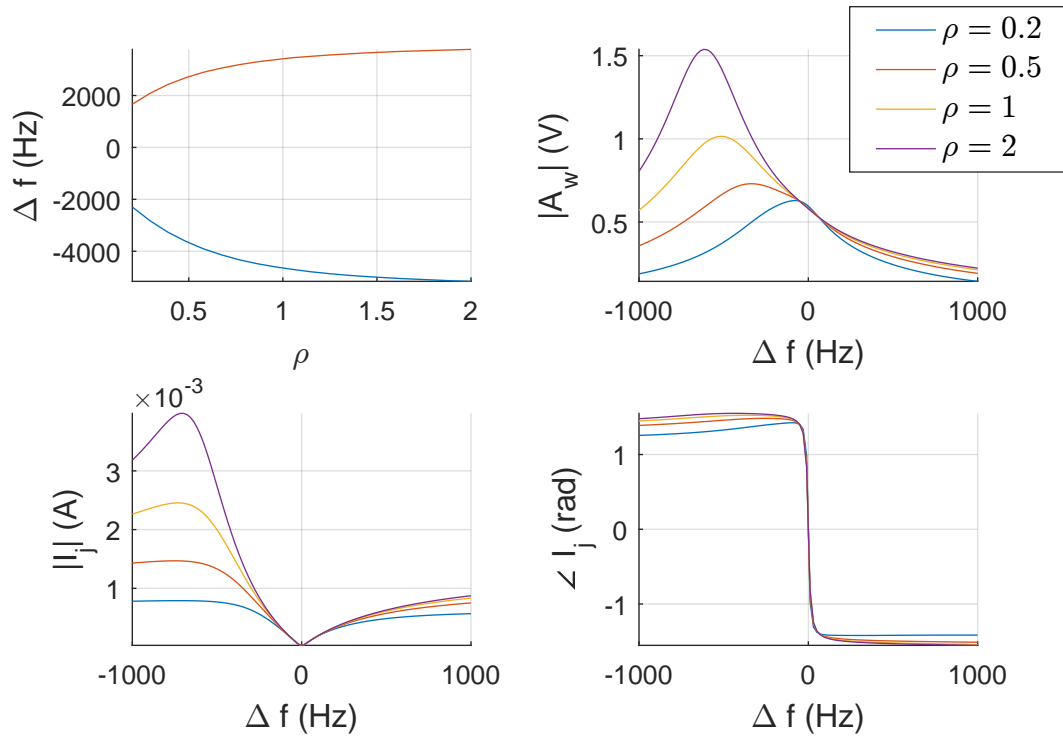


Figure 5.6. Change in the locking range and steady-state solution values with variation in ρ .

Variation in Quality Factor

Figure 5.7 shows variations in the steady-state solution in response to changes in the resonator quality factor. The main effect of varying this parameter is apparent in the change in the locking envelope, with higher quality factors restricting the range. In fact, this parameter appears to act as a simple scaling factor in frequency, with a higher quality factor correlating to a more compact frequency response with little impact on the response magnitudes. Varying this parameter could be a means of controlling the locking range itself, though practically speaking this may be difficult, as it would necessitate either using resonator crystals with varying specifications for each oscillator, or artificially damping the resonator to lower the quality factor.

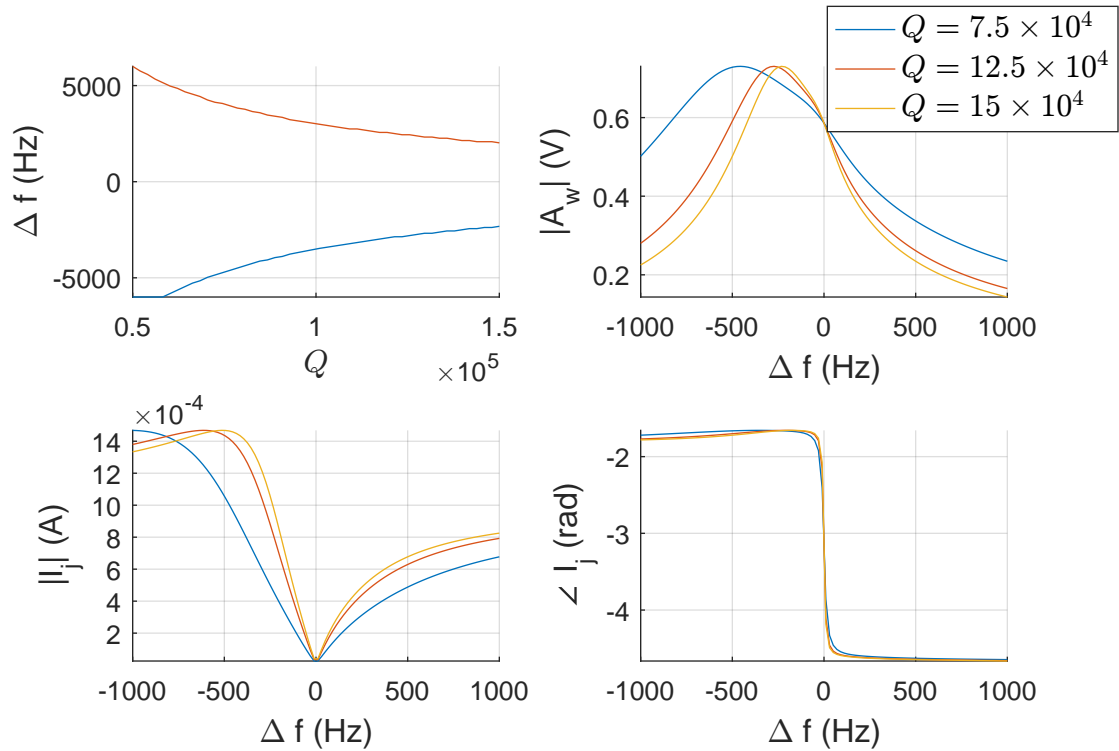


Figure 5.7. Change in the locking range and steady-state solution values with variation in quality factor.

5.3.7 Conclusions From the Analysis

In this section, the dependence of the locking range and oscillation amplitude of a single oscillator operating under external excitations was characterized analytically. Four system parameters were identified as directly impacting these factors: the crystal quality factor (Q), the gate-source feedback capacitance (C_g), and the amplitude of and coupling to the excitation signal (v_j and ρ , respectively). Because the purpose of this analysis was to inform the design of a coupled system of these oscillators for subsequent sections, the key takeaways were that higher values of C_g support lower oscillation amplitudes, higher values of quality factor support more narrow locking ranges, and that stronger excitation values and stronger coupling to said excitation

will support wider locking ranges. As will be discussed in subsequent sections, the latter parameter, ρ , provides the most direct path towards manipulating the locking behaviors in the coupled system in response to incident light.

5.4 Experimental Methodology

In this section, we will pivot from the examination of a single oscillator under signal injection and begin an empirical examination of a coupled network. Based on the parametric study performed in the preceding section, the easiest means of manipulating the locking ranges of the individual oscillators is to vary the conductance of the coupling paths (i.e. ρ). This method of coupling is also convenient for use in pattern recognition applications, as off-the-shelf photoconductive components can be used directly to couple the strength of the coupling path for each oscillator to the brightness or spectral content of incident light on the photoconductors.

5.4.1 Design Overview

The system of interest consists of three main components: an oscillator circuitry board, a variable-RGB microscope illuminator, and a dark box. The oscillator board consists of a set of three 16 MHz Colpitts oscillators, which are AC coupled to a single common node via a set of three CdSe photocells. The dark box is an opaque, black hexagon into which the oscillator board and illuminator head are inset. A small circular cutout is placed over each photocell and an optical filter tuned to pass either red, green, or blue light is placed within each cutout, filtering the light incident on each photocell. Figure 5.8 shows a high level diagram of the experimental setup.

5.4.2 Oscillator Board

The oscillator board is a hexagonal circuit board containing the three Colpitts oscillators, with a high impedance buffer for measurement purposes on the gate and

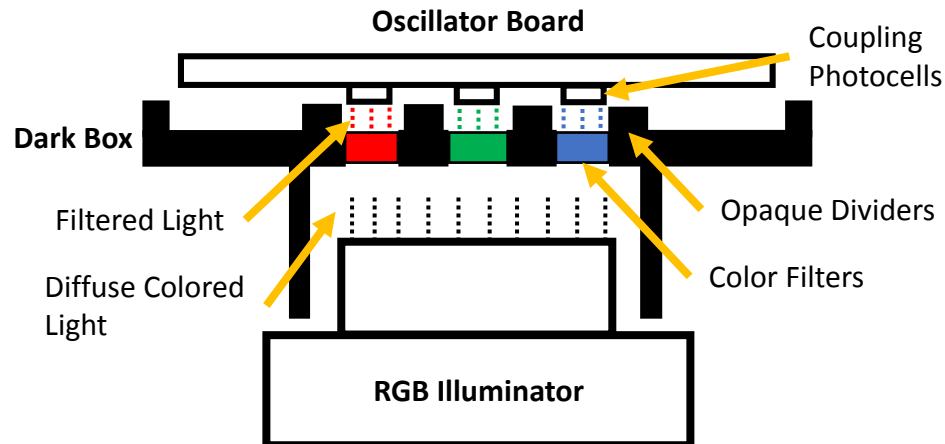


Figure 5.8. High-level diagram of the experimental setup.

source nodes for each oscillator and one on the common coupling node. The oscillators are connected to the common node by a large ($1 \mu\text{F}$) capacitor (which provides DC signal blocking but admits the 16 MHz oscillator signals) and a single CdSe photocell. Although the Colpitts circuit incorporates potential parasitic elements, in order to preserve symmetry in terms of the values of these elements, each oscillator was laid out with an identical footprint and arranged in a rotational pattern about the common node with an angle of 120° between them. Figure 5.9 shows an overview of the oscillator board, including the geometry and high-level electrical connections.

While the oscillators are nominally identical, small variations in the crystals (and possibly other components) will cause the oscillators to be, in practice, varied in frequency on the order of approximately 100 Hz. In this work we examine two cases: a system with the oscillators approximately equally spaced in frequency and one in which two oscillators are close in frequency while the third is more isolated. This controlled mistuning was achieved by carefully selecting from a set of pre-characterized resonators. Figure 5.10 illustrates the frequency separation between the oscillators for each case.

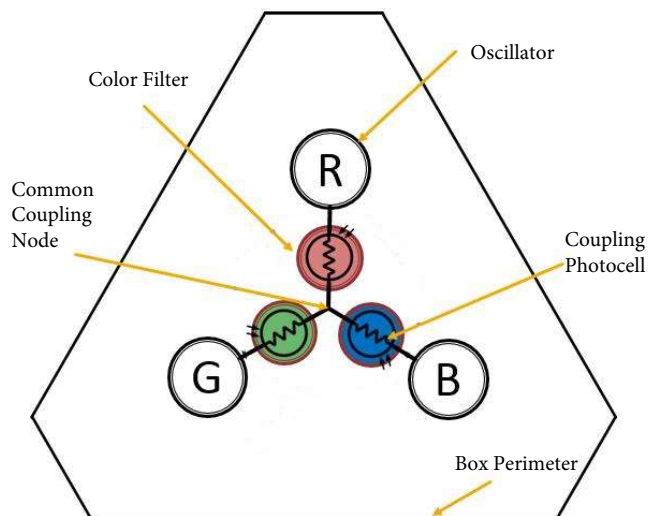


Figure 5.9. Diagram of the oscillator board layout showing the geometry, oscillator/photocell locations, and filter locations. Each oscillator (labeled R, G, and B after their associated color filter) consists of a single Colpitts oscillator of the type described in Section 4.2.1.

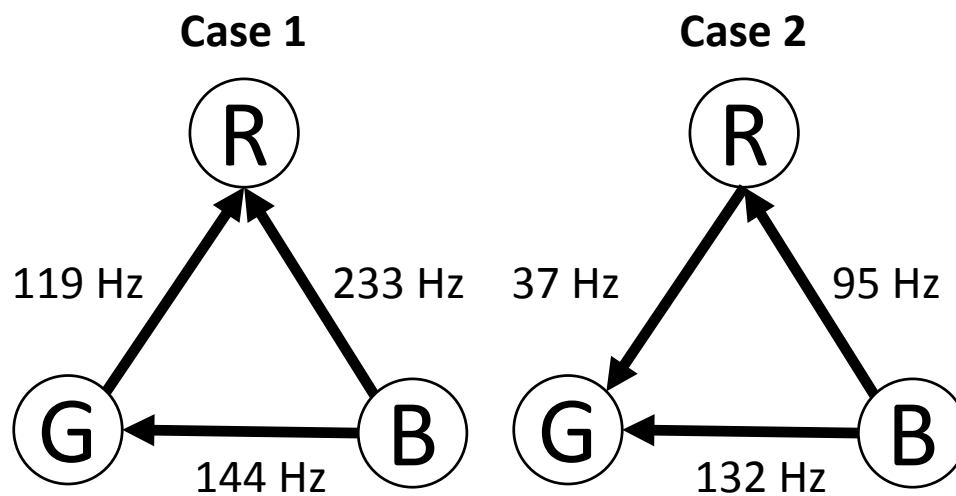


Figure 5.10. Diagram illustrating the frequency separation between the two versions of the system examined in this work.

5.4.3 Illumination Source

The illumination source is an adjustable red-green-blue-amber (RGBA) microscope illuminator with a regulated power output. The peak wavelengths for each color channel are 625 nm for red, 523 nm for green, 457 nm for blue, and 587 nm for amber, though the latter was not utilized in this work. The illuminator has a 1" diameter aperture/diffuser, which is large enough to encompass all three of the photocells simultaneously.

5.4.4 Component Characterization

Illuminator and Filters

In order to examine the precise dynamics of the system as a function of color exposure, it is necessary to characterize the spectra of light that passes through each filter as the illuminator's light levels are varied. This was done by constructing a secondary dark box similar to the first, but instead of mounting to the oscillator board it was designed to fasten to a handheld spectrometer (a Sekonic C-700-U Spectromaster). Next, two of the filters were blocked, and the transmitted light spectrum from the third was measured for varying illumination levels for each color channel. This process was repeated for each of the filters. Figure 5.11 below shows the results of this test, showing the measured irradiance for each color channel and filter combination. As can be seen in the figure, each filter is reasonably capable of filtering out the emissions for the non-correlating bands. In particular, the cross-admissions for the green and blue filters are at least two orders of magnitude less than that of the corresponding color band, and the red is still approximately one order of magnitude less. In particular, since the photocells are known to be less reactive to blue light, the blue-light leakage for the red filter is considered negligible.

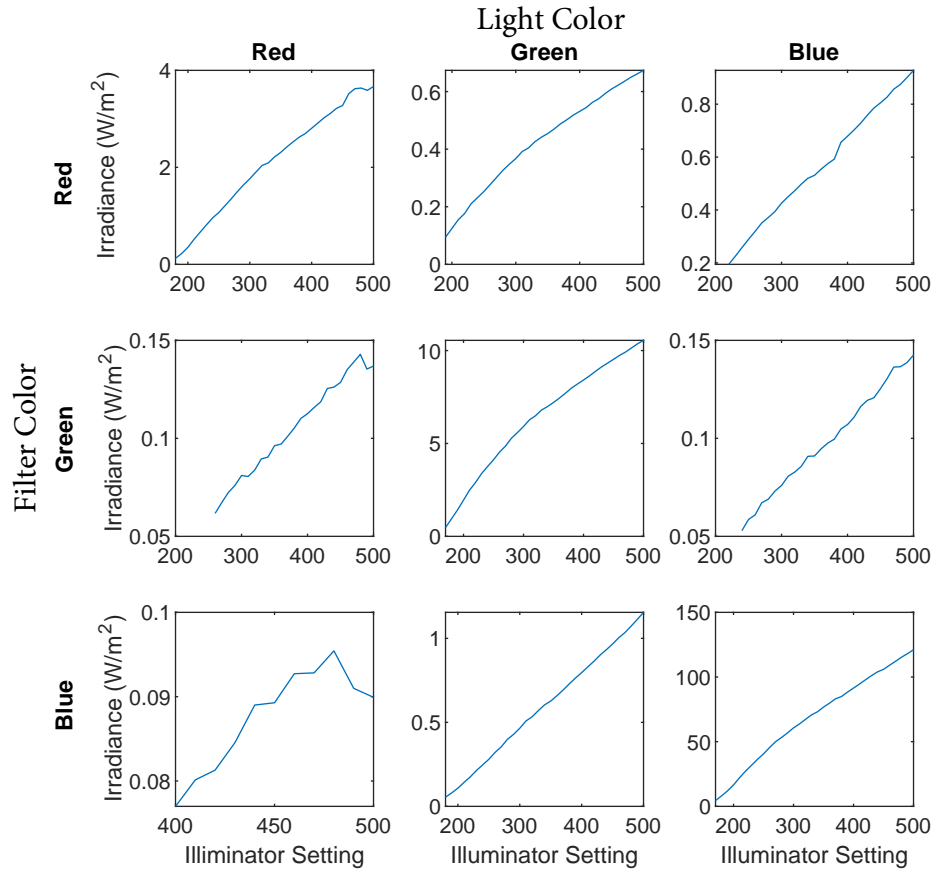


Figure 5.11. Diagram showing the measured irradiance on each photocell for each combination of light and filter color.

CdSe Photocells

The light sensitive elements used in the coupling paths between the oscillators are CdSe-based photocells, which are also known as photoresistors. As the name suggests, these cells are nominally resistive in nature and are most commonly used in DC applications. Due to this, however, commercially available photocells are typically only rated in terms of their DC electrical characteristics, making it necessary to characterize their dynamics for high-frequency applications. Figure 5.12 shows a top view of a typical commercially available photocell.

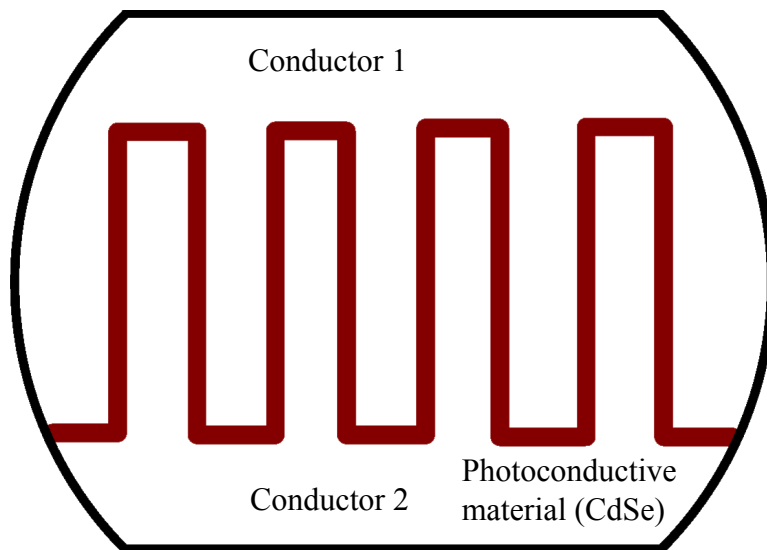


Figure 5.12. Diagram of a CdSe photocell.

The cell itself consists of a pair of conductors separated by a trace of photoconductive material. When the cell is exposed to light within a particular wavelength (typically in the visible band, with the maximum sensitivity being around 720 nm for CdSe cells), the conductance of this region increases, decreasing the resistance of the device as a whole. The relative sensitivity of the cell to varying wavelengths is given in the product datasheet. For the purposes of characterizing the higher-frequency behaviors of the device, the equivalent circuit shown in Figure 5.13 was assumed.

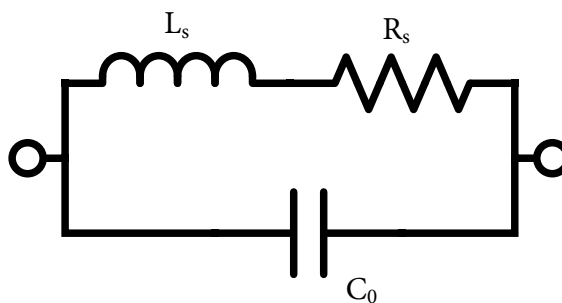


Figure 5.13. Equivalent Circuit of a CdSe photocell.

In order to find the values of the equivalent circuit parameters as a function of irradiance, the cell was excited using an external function generator. The current response of the cell was then measured using an op-amp based transimpedance amplifier. The transfer function of the system was measured by varying the frequency of the input signal and measuring the amplitude and phase of the output using a lock-in amplifier. This procedure was repeated for varying illumination levels using a 625 nm LED light source. The measured transfer function was then normalized by that of an identical system with the photocell replaced by a 1 k Ω resistor in order to remove the high-frequency dynamics of the op-amps and instrumentation from the measurements. Finally, the resulting transfer function was then fit to the expected model using a least-squares method. Figure 5.14 shows the results of the fit for each parameter as well as the mean squared error of the fit as a function of the irradiance of the cell. Despite the fit returning a negative value for the internal inductance, the absolute value was extremely small and the negative value is likely just an artifact of the fit. This implies that the model can be reduced to a simple parallel-RC circuit. Additionally, a discontinuity was found in the fit at an irradiance of approximately 0.19 Wm⁻², which may be indicative of nonlinear behavior in the photoconductor at low light levels. Fortunately, this behavior is only observed when the photocell is in a relatively high-impedance state (>3 k Ω), so that the effect on the oscillator dynamics should be negligible.

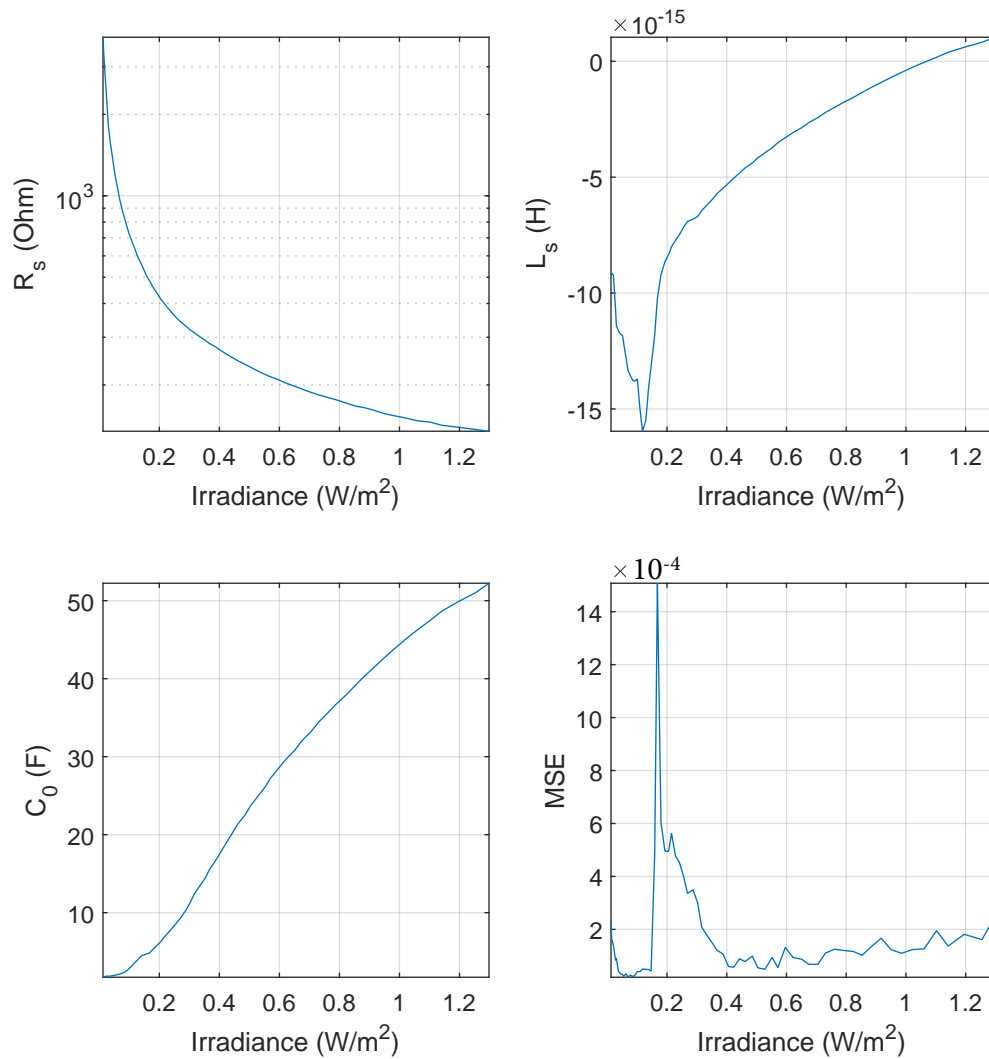


Figure 5.14. Experimental characterization of the photocell with 625 nm light using the model given by Figure 5.13. (Upper-Left) Effective series resistance. (Upper-Right) Effective series inductance. (Lower-Left) Effective shunt capacitance. (Lower-Right) Mean squared error between the best fit of the model and the measured impedance of the photocell.

Mistuning Control

While the analysis section was illuminating in terms of the effects of the circuit parameters on the oscillator's dynamics, one additional measure which may be useful in the design of this system is precision control of the oscillators' natural frequencies. The most direct way of achieving this is to add a small capacitance in series with the resonator, as was done with the resonator crystals in Chapters 2 and 3. This effectively adds a small stiffness term to the equations of motion. By using a varactor diode as the capacitive element, precision control can be exerted over the oscillation frequency by varying a DC bias voltage. These devices are often included in packages of two diodes, connected at a common cathode, such that they can be configured to operate as an individual diode, or a series or parallel pair. Figure 5.15 shows the result of an experimental characterization of this effect for both a single and dual (parallel) varactor configuration. For the dual varactor, a maximum shift of 658 Hz was achieved, whereas the single achieved a shift of 1143 Hz.

5.5 Experimental Results

5.5.1 Case One: Equally Spaced Oscillators

Figure 5.16 shows a set of spectral measurements measured at the common coupling node under varying lighting conditions. In the dark case (upper-left), the three photocells are all in a high-impedance state, meaning the oscillators are not coupled strongly enough to lock in frequency. Because of this, three distinguishable peaks can be identified which correspond, from left to right, to the blue-, green-, and red-linked oscillators. Additionally, some smaller sideband frequencies caused by injection pulling between the oscillators are visible. As the intensity of the blue light is increased (upper-right), however, the impedance of the blue photocell drops enough that the blue oscillator (the leftmost peak) locks in frequency to the green (the center peak). A similar effect occurs between the red- and green-linked oscillators by

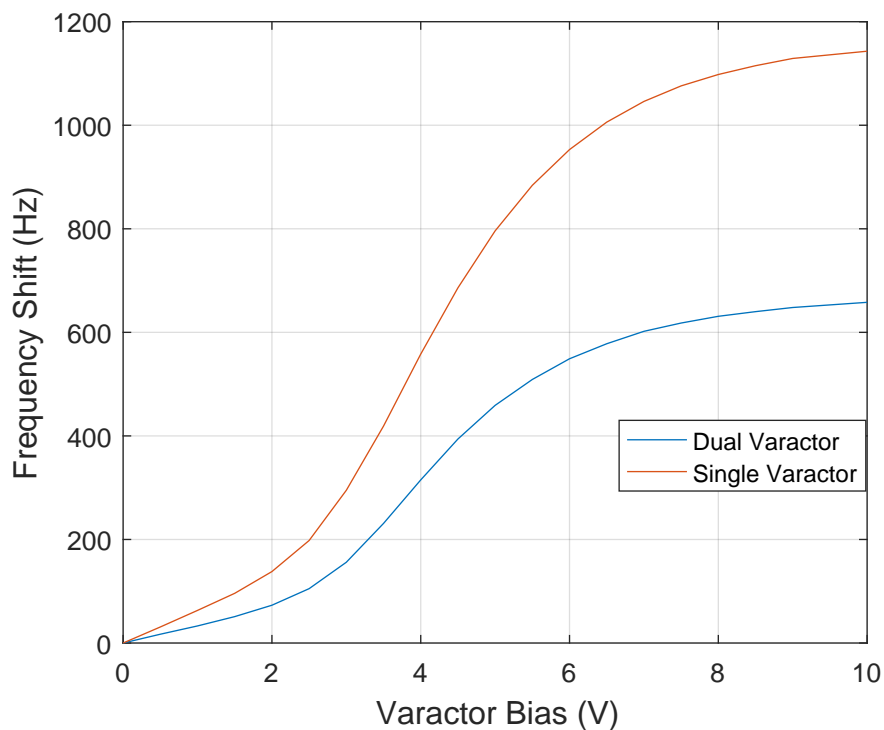


Figure 5.15. Experimental characterization of the frequency shift in a varactor-mistuned Colpitts oscillator.

increasing the levels of red and green light while leaving the blue low (lower-left), though in this case the pulling on the third oscillator becomes very significant, creating a number of large sideband signals. By increasing all three of the colors (i.e. moving towards white light), all three of the oscillators will lock at a frequency near the center of the original distribution. In theory, a fifth state could exist in which the red- and blue-linked oscillators are synchronized while excluding the green, but in practice this is difficult to replicate because the resulting locked frequency is in very close proximity to the third oscillator's natural frequency, which instead triggers the fully locked condition.

Using these results, it becomes possible to make inferences regarding the color content of the light by measuring the frequency spectrum of the common node. To quantify this, the illumination was swept through a 3-dimensional space in color, with

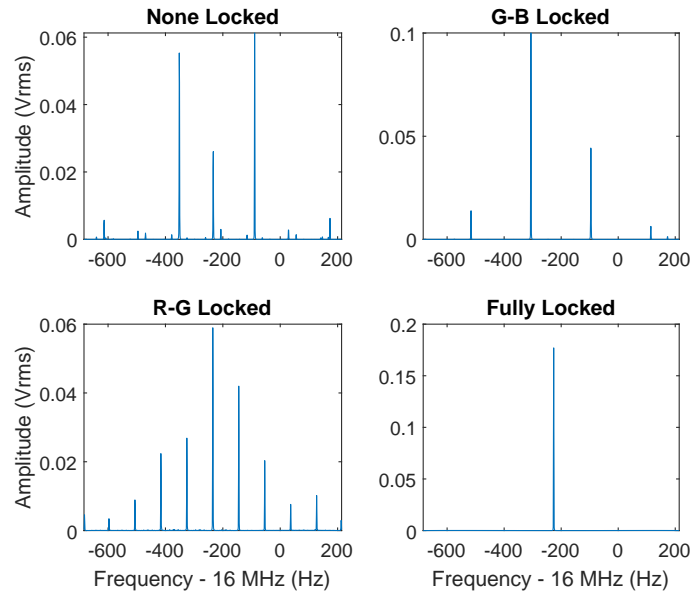


Figure 5.16. Comparison of four identifiable locking states under various illumination conditions. These spectra were measured at [R,G,B] power coordinates, in Wm^{-2} , of: (Upper-Left) [0, 0, 0], (Upper-Right) [0, 6, 60], (Lower-Left) [1.4, 1, 0], and (Lower-Right) [1.4, 6, 60].

each axis representing the irradiance of a particular color channel (red, green, or blue). At each point, the spectrum at the common node was recorded, and the locking state was categorized based on these spectral measurements as per Figure 5.16. Figure 5.17 shows a slice chart of these states versus the irradiance of each channel, with each color highlighting a region which encompasses a specific locking state. These regions are color coded in the figure to indicate the color of light corresponding to that state, i.e. locking between the blue- and green-linked oscillators is indicated by cyan coloration and locking between all oscillators indicated by light gray.

As expected, four regions are visible, corresponding to each type of locking condition. Since the irradiance in each color band has a direct correlation to the color of the light produced by the LEDs, this system is effectively a threshold sensor which reacts to exposure to white, cyan, and yellow colored light. By altering the frequencies of the oscillators, the bands of the light filters, and adjusting the impedance ranges of the

photocells, it may be possible to fine tune these regions and obtain more controlled thresholds, as will be demonstrated in the next section.

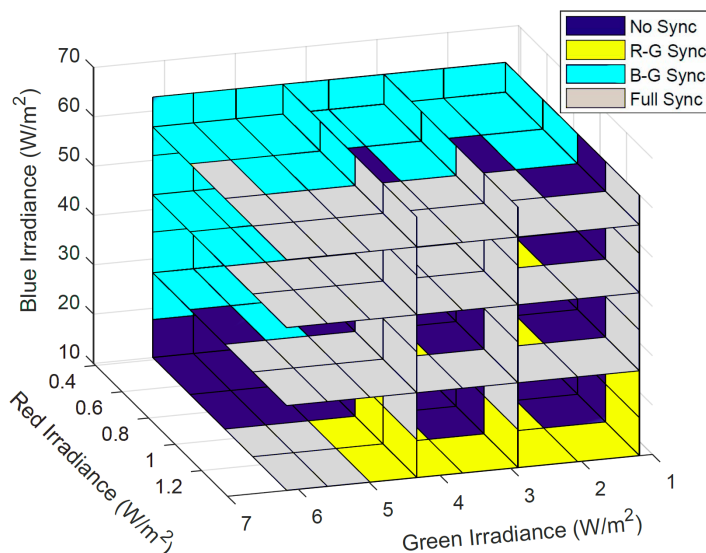


Figure 5.17. State map for a system with the oscillators spaced approximately evenly in frequency.

5.5.2 Case Two: Asymmetrically-Spaced Oscillators

For this case, the crystal of the red-linked oscillator was replaced with one of a slightly lower frequency. This shifted the oscillator's natural frequency downward such that it was now between the green and blue oscillators, with the green being much closer in frequency. Repeating the state map experiment from before shows significantly altered locking regions, mainly in the sense that it now seems to be sensitive to magenta light for one of its locked states and no longer has a state corresponding to cyan. Additionally, this version of the system is significantly more sensitive to yellow-colored light, requiring lower levels of both green and red light to enter this state. This is due to the increased proximity between these two oscillators in frequency, which enables the oscillators to become locked with a weaker level of coupling.

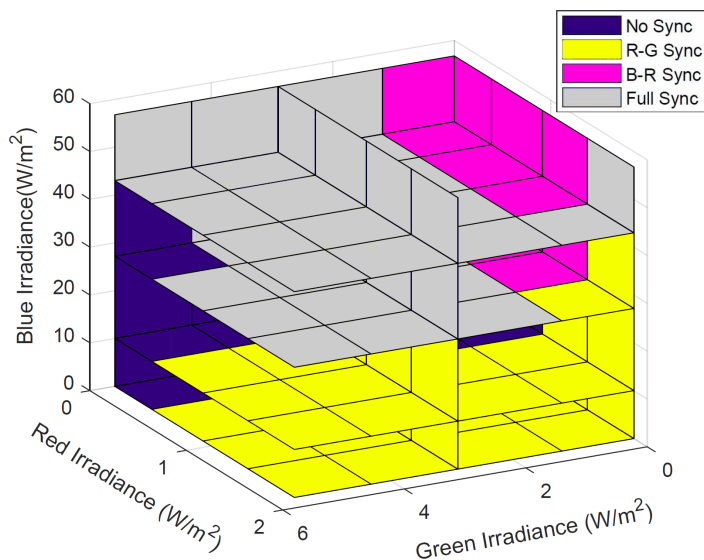


Figure 5.18. State map for a system with the red- and green-linked oscillators close in frequency.

5.6 Conclusions

This chapter presents a proof-of-concept color recognition device which utilizes frequency-locking within a network of coupled oscillators to make inferences about the color of incident light. These inferences are made by mapping the locking state to a set of regions in color space, and it is shown that these regions can be manipulated by controlling certain parameters of the oscillators, such as frequency separation and the coupling coefficients. An elementary harmonic model is derived which demonstrates further trends in the locking behaviors and internal dynamics of the individual oscillators, and offers paths for future works to more precisely tune the response of this type of network. Future works may seek to exploit this behavior to create a fully realized optical pattern recognition scheme, utilizing the inputs from multiple oscillator networks to make inferences about a given array of color inputs.

6. CONCLUSIONS AND RECOMMENDATIONS FOR FUTURE STUDY

6.1 Summary

In this work, an experimental apparatus consisting of a large network of coupled electromechanical resonators was designed, modeled, and tested experimentally. The emergent dynamics in this coupled system were then exploited to create a resonant mass based volatile organic compound sensor. The salient dynamics identified in the system allowed for a single-input, single-output device which alleviated several of the major constraints on contemporary VOC sensors, namely a lack of selectivity in a multi-analyte environment and the throughput constraints presented by rote parallelization of many individual sensors.

In Chapter 5 of this work, a system was designed and demonstrated which coupled the internal locking state of a network of 3 coupled Colpitts oscillators to the color content of incident light. A first-order harmonic model was created which could examine the steady-state locking behavior of the elements of this system in response to varying the circuit parameters, and the ways in which these parameters could tune the behavior of the individual oscillators were discussed. The locking state of the oscillators within the system was then shown to be experimentally measurable through a single output port, allowing the color of incident light to be inferred from a single spectral measurement.

6.2 On Future Work for Mass Sensing

In future work on this subject, it may be useful to further investigate ways to prevent the slow frequency drift observed during the system's operation. While the likely cause was identified as oxidation of the silver coating of the resonator, it will be necessary to prevent this in a real-world implementation so as not to interfere

with the frequency measurements. Additionally, further study may be warranted in the investigation of various sorbents with which to functionalize the resonators, with a particular emphasis placed on improving the selectivity of the chemistries and identifying additional sorbents which are more robust to longer term real-world environmental conditions.

6.3 On Future Work for Oscillator-Based Pattern Recognition

For future study on this system, a more in depth examination into the nonlinear dynamics of this system is warranted. Unfortunately, ordinary methods of analysis such as phase-only models are likely insufficient for this task, as this system exhibits significant amplitude dynamics and complex, asymmetric coupling, which makes such models ill-suited for describing the behavior of the system. Perturbative techniques such as multiple scales or averaging analyses may find more success, particularly when it comes to incorporating the amplitude dynamics into the model. Additionally, more study should be put into the quasi-locking tendencies of the system, and how those behaviors affect the interactions between oscillators in larger networks. Finally, larger systems should be investigated, possibly eventually approaching the continuum limit, as well as means of encoding responses to more complex stimuli to achieve a higher degree of pattern recognition than the single-pixel sensor described in this work.

REFERENCES

REFERENCES

- [1] B. A. Geesey, B. A. Wetherton, N. Bajaj, and J. F. Rhoads. Shaping the frequency response of electromechanical resonators using a signal interference control topology. *Journal of Dynamic Systems, Measurement, and Control*, 139(3):031011, 2017.
- [2] D. S. Greywall and P. A. Busch. Coupled micromechanical drumhead resonators with practical application as electromechanical bandpass filters. *Journal of Micromechanics and Microengineering*, 12(6):925–938, 2002.
- [3] E. Buks and M. L. Roukes. Electrically tunable collective response in a coupled micromechanical array. *Journal of Microelectromechanical Systems*, 11(6):802–807, 2002.
- [4] D. B. Blocher, A. T. Zehnder, and R. H. Rand. Frequency multiplication and demultiplication in MEMS. In *MEMS and Nanotechnology, Volume 6*, pages 53–58. Springer, 2013.
- [5] V. B. Chivukula and J. F. Rhoads. Microelectromechanical bandpass filters based on cyclic coupling architectures. *Journal of Sound and Vibration*, 329(20):4313 – 4332, 2010.
- [6] J. A. Judge, B. H. Houston, D. M. Photiadis, and P. C. Herdic. Effects of disorder in one- and two-dimensional micromechanical resonator arrays for filtering. *Journal of Sound and Vibration*, 290(3):1119 – 1140, 2006.
- [7] Y. Lin, L. Hung, S. Li, Z. Ren, and T.-C. Nguyen. Quality factor boosting via mechanically-coupled arraying. In *TRANSDUCERS 2007-2007 International Solid-State Sensors, Actuators and Microsystems Conference*, pages 2453–2456, 2007.
- [8] K. R. Qalandar, B. S. Strachan, B. Gibson, M. Sharma, A. Ma, S. W. Shaw, and K. L. Turner. Frequency division using a micromechanical resonance cascade. *Applied Physics Letters*, 105(24):244103, 2014.
- [9] D. Weinstein, S. A. Bhave, M. Tada, S. Mitarai, S. Morita, and K. Ikeda. Mechanical coupling of 2d resonator arrays for MEMS filter applications. In *2007 IEEE International Frequency Control Symposium Joint with the 21st European Frequency and Time Forum*, pages 1362–1365, 2007.
- [10] A. Erturk and D. J. Inman. Broadband piezoelectric power generation on high-energy orbits of the bistable Duffing oscillator with electromechanical coupling. *Journal of Sound and Vibration*, 330(10):2339–2353, 2011.
- [11] D. F. Berdy, B. Jung, J. F. Rhoads, and D. Peroulis. Increased-bandwidth, meandering vibration energy harvester. In *2011 16th International Solid-State Sensors, Actuators and Microsystems Conference*, pages 2638–2641, 2011.

- [12] R. L. Harne. Modeling and analysis of distributed electromagnetic oscillators for broadband vibration attenuation and concurrent energy harvesting. *Applied Mathematical Modelling*, 37(6):4360–4370, 2013.
- [13] W. Wang, X. Wang, X. He, M. Wang, H. Shu, and K. Xue. Comparisons of bioinspired piezoelectric wind energy harvesters with different layout of stiffeners based on leaf venation prototypes. *Sensors and Actuators A: Physical*, 298(1):111570, 2019.
- [14] B. E. DeMartini, J. F. Rhoads, M. A. Zielke, K. G. Owen, S. W. Shaw, and K. L. Turner. A single input-single output coupled microresonator array for the detection and identification of multiple analytes. *Applied Physics Letters*, 93(5):054102, 2008.
- [15] V. Kumar, J. W. Boley, Y. Yang, H. Ekowaluyo, J. K. Miller, G. T.-C. Chiu, and J. F. Rhoads. Bifurcation-based mass sensing using piezoelectrically-actuated microcantilevers. *Applied Physics Letters*, 98(15):153510, 2011.
- [16] V. Kumar, Y. Yang, J. W. Boley, G. T.-C. Chiu, and J. F. Rhoads. Modeling, analysis, and experimental validation of a bifurcation-based microsensor. *Journal of Microelectromechanical Systems*, 21(3):549–558, 2012.
- [17] Y. T. Yang, C. Callegari, X. L. Feng, K. L. Ekinici, and M. L. Roukes. Zeptogram-scale nanomechanical mass sensing. *Nano Letters*, 6(4):583–586, 2006.
- [18] N. Bajaj, J. F. Rhoads, and G. T.-C. Chiu. Characterization of resonant mass sensors using inkjet deposition. In *ASME 2016 Dynamic Systems and Control Conference*, page V002T26A005. American Society of Mechanical Engineers, 2016.
- [19] N. Bajaj, J. F. Rhoads, and G. T.-C. Chiu. Characterizing the spatially dependent sensitivity of resonant mass sensors using inkjet deposition. *Journal of Dynamic Systems, Measurement, and Control*, 139(11):114505, 2017.
- [20] J. Feng, X. Ye, M. Esashi, and T. Ono. Mechanically coupled synchronized resonators for resonant sensing applications. *Journal of Micromechanics and Microengineering*, 20(11):115001, 2010.
- [21] K. Gajo, S. Schuz, and E. M. Weig. Strong 4-mode coupling of nanomechanical string resonators. *Applied Physics Letters*, 111(13):133109, 2017.
- [22] A. B. Sabater, A. G. Hunkler, and J. F. Rhoads. A single-input, single-output electromagnetically-transduced microresonator array. *Journal of Micromechanics and Microengineering*, 24(6):065005, 2014.
- [23] M. Spletzer, A. Raman, A. Q. Wu, X. Xu, and R. Reifenberger. Ultrasensitive mass sensing using mode localization in coupled microcantilevers. *Applied Physics Letters*, 88(25):254102, 2006.
- [24] M. Spletzer, A. Raman, H. Sumali, and J. P. Sullivan. Highly sensitive mass detection and identification using vibration localization in coupled microcantilever arrays. *Applied Physics Letters*, 92(11):114102, 2008.

- [25] D. K. Agrawal, J. Woodhouse, and A. A. Seshia. Synchronization in a coupled architecture of microelectromechanical oscillators. *Journal of Applied Physics*, 115(16):164904, 2014.
- [26] R. L. Harne and K. W. Wang. Robust sensing methodology for detecting change with bistable circuitry dynamics tailoring. *Applied Physics Letters*, 102(20):203506, 2013.
- [27] C. T. Nguyen. MEMS technology for timing and frequency control. *IEEE Transactions on Ultrasonics, Ferroelectrics, and Frequency Control*, 54(2):251–270, 2007.
- [28] J. M. Puder, S. S. Bedair, J. S. Pulskamp, R. Q. Rudy, R. G. Polcawich, and S. A. Bhave. Higher dimensional flexure mode for enhanced effective electromechanical coupling in PZT-on-silicon MEMS resonators. In *2015 Transducers - 2015 18th International Conference on Solid-State Sensors, Actuators and Microsystems*, pages 2017–2020, 2015.
- [29] V. Kumar and J. F. Rhoads. Modeling and analysis of an optically-actuated, bistable MEMS device. *Journal of Computational and Nonlinear Dynamics*, 7(2):021007, 2012.
- [30] A. B. Sabater and J. F. Rhoads. On the dynamics of two mutually-coupled, electromagnetically-actuated microbeam oscillators. *Journal of Computational and Nonlinear Dynamics*, 7(3):031011, 2012.
- [31] C. Pierre and E. H. Dowell. Localization of vibrations by structural irregularity. *Journal of Sound and Vibration*, 114(3):549–564, 1987.
- [32] C. Pierre and D. V. Murthy. Aeroelastic modal characteristics of mistuned blade assemblies-mode localization and loss of eigenstructure. *AIAA Journal*, 30(10):2483–2496, 1992.
- [33] M. K. Zalalutdinov, J. W. Baldwin, M. H. Marcus, R. B. Reichenbach, J. M. Parpia, and B. H. Houston. Two-dimensional array of coupled nanomechanical resonators. *Applied Physics Letters*, 88(14):143504, 2006.
- [34] V. T. Yolong and P. Woaf. Synchronization in a ring of mutually coupled electromechanical devices. *Physica Scripta*, 74(5):591–598, 2006.
- [35] J. Buck. Synchronous rhythmic flashing of fireflies. II. *The Quarterly Review of Biology*, 63(3):265–289, 1988.
- [36] D. C. Michaels, E. P. Matyas, and J. Jalife. Mechanisms of sinoatrial pacemaker synchronization: a new hypothesis. *Circulation Research*, 61(5):704–714, 1987.
- [37] R. S. MacKay and S. Aubry. Proof of existence of breathers for time-reversible or Hamiltonian networks of weakly coupled oscillators. *Nonlinearity*, 7(6):1623–1643, 1994.
- [38] R. Yamapi and P. Woaf. Synchronized states in a ring of four mutually coupled self-sustained electromechanical devices. *Communications in Nonlinear Science and Numerical Simulation*, 11(2):186–202, 2006.

- [39] A. B. Sabater and J. F. Rhoads. Dynamics of globally and dissipatively coupled resonators. *Journal of Vibration and Acoustics*, 137(2):021016, 2015.
- [40] C. B. Wallin, R. De Alba, D. Westly, G. Holland, S. Grutzik, R. H. Rand, A. T. Zehnder, V. A. Aksyuk, S. Krylov, and B. R. Ilic. Nondegenerate parametric resonance in large ensembles of coupled micromechanical cantilevers with varying natural frequencies. *Physical Review Letters*, 121(26):264301, 2018.
- [41] Y. Bromberg, M. C. Cross, and R. Lifshitz. Response of discrete nonlinear systems with many degrees of freedom. *Physical Review E*, 73(1):016214, 2006.
- [42] C. Borra, C. S. Pyles, B. A. Wetherton, D. D. Quinn, and J. F. Rhoads. The dynamics of large-scale arrays of coupled resonators. *Journal of Sound and Vibration*, 392(1):232–239, 2017.
- [43] M. Sato, B. E. Hubbard, and A. J. Sievers. Colloquium: Nonlinear energy localization and its manipulation in micromechanical oscillator arrays. *Reviews of Modern Physics*, 78(1):137–157, 2006.
- [44] R. Yamapi, F.M. Moukam Kakmeni, and J.B. Chabi Orou. Nonlinear dynamics and synchronization of coupled electromechanical systems with multiple functions. *Communications in Nonlinear Science and Numerical Simulation*, 12(4):543–567, 2007.
- [45] J. F. Rhoads, V. Kumar, S. W. Shaw, and K. L. Turner. The non-linear dynamics of electromagnetically actuated microbeam resonators with purely parametric excitations. *International Journal of Non-Linear Mechanics*, 55(1):79–89, 2013.
- [46] R. L. Harne and K. W. Wang. A bifurcation-based coupled linear-bistable system for microscale mass sensing. *Journal of Sound and Vibration*, 333(8):2241–2252, 2014.
- [47] N. Bajaj, A. B. Sabater, J. N. Hickey, G. T. Chiu, and J. F. J. Rhoads. Design and implementation of a tunable, duffing-like electronic resonator via nonlinear feedback. *Journal of Microelectromechanical Systems*, 25(1):2–10, 2016.
- [48] I. Stachiv, A. I. Fedorchenko, and Y.-L. Chen. Mass detection by means of the vibrating nanomechanical resonators. *Applied Physics Letters*, 100(9):093110, 2012.
- [49] H. P. Lang, M. Hegner, and C. Gerber. Cantilever array sensors. *Materials Today*, 8(4):30–36, 2005.
- [50] C. B. Burgner, L. A. Shaw, and K. L. Turner. A new method for resonant sensing based on noise in nonlinear MEMS. In *2012 IEEE 25th International Conference on Micro Electro Mechanical Systems (MEMS)*, pages 511–514, 2012.
- [51] A. Boisen, J. Thaysen, H. Jensenius, and O. Hansen. Environmental sensors based on micromachined cantilevers with integrated read-out. *Ultramicroscopy*, 82(1-4):11–16, 2000.
- [52] H. Pakdast and M. Lazzarino. Triple coupled cantilever systems for mass detection and localization. *Sensors and Actuators A: Physical*, 175(1):127–131, 2012.

- [53] M. Su, S. Li, and V. P. Dravid. Microcantilever resonance-based DNA detection with nanoparticle probes. *Applied Physics Letters*, 82(20):3562–3564, 2003.
- [54] R. Raiteri, M. Grattarola, H.-J. Butt, and P. Skladal. Micromechanical cantilever-based biosensors. *Sensors and Actuators B: Chemical*, 79(2):115–126, 2001.
- [55] A. Gupta, D. Akin, and R. Bashir. Single virus particle mass detection using microresonators with nanoscale thickness. *Applied Physics Letters*, 84(11):1976–1978, 2004.
- [56] P. S. Waggoner, M. Varshney, and H. G. Craighead. Detection of prostate specific antigen with nanomechanical resonators. *Lab Chip*, 9(21):3095–3099, 2009.
- [57] H. P. Lang and C. Gerber. Microcantilever sensors. In *STM and AFM Studies on (Bio)molecular Systems: Unravelling the Nanoworld*, pages 1–27. Springer Berlin Heidelberg, 2008.
- [58] R. T. Howe and R. S. Muller. Integrated resonant-microbridge vapor sensor. In *1984 International Electron Devices Meeting*, pages 213–216, 1984.
- [59] R. T. Howe and R. S. Muller. Resonant-microbridge vapor sensor. *IEEE Transactions on Electron Devices*, 33(4):499–506, 1986.
- [60] D. Lange, C. Hagleitner, A. Hierlemann, O. Brand, and H. Baltes. Complementary metal oxide semiconductor cantilever arrays on a single chip: mass-sensitive detection of volatile organic compounds. *Analytical Chemistry*, 74(13):3084–3095, 2002.
- [61] D. F. Wang, K. Chatani, T. Ikehara, and R. Maeda. Mode localization analysis and characterization in a 5-beam array of coupled nearly identical micromechanical resonators for ultra-sensitive mass detection and analyte identification. *Microsystem Technologies*, 18(11):1923–1929, 2012.
- [62] K. J. Johnson and S. L. Rose-Pehrsson. Sensor array design for complex sensing tasks. *Annual Review of Analytical Chemistry*, 8(1):287–310, 2015.
- [63] D. K. Agrawal, J. Woodhouse, and A. A. Seshia. Observation of locked phase dynamics and enhanced frequency stability in synchronized micromechanical oscillators. *Physical Review Letters*, 111(8):084101, 2013.
- [64] M. Zalalutdinov, K. L. Aubin, M. Pandey, A. T. Zehnder, R. H. Rand, H. G. Craighead, J. M. Parpia, and B. H. Houston. Frequency entrainment for micromechanical oscillator. *Applied Physics Letters*, 83(16):3281–3283, 2003.
- [65] R. Yamapi and P. Wofo. Dynamics and synchronization of coupled self-sustained electromechanical devices. *Journal of Sound and Vibration*, 285(4):1151–1170, 2005.
- [66] M. C. Cross, J. L. Rogers, R. Lifshitz, and A. Zumdick. Synchronization by reactive coupling and nonlinear frequency pulling. *Physical Review E*, 73(3):036205, 2006.

- [67] R. Adler. A Study of Locking Phenomena in Oscillators. *Proceedings of the IRE*, 34(6):351–357, 1946.
- [68] P. Bhansali and J. Roychowdhury. Gen-Adler: The generalized Adler’s equation for injection locking analysis in oscillators. In *2009 Asia and South Pacific Design Automation Conference*, pages 522–527, 2009.
- [69] S. H. Strogatz. From Kuramoto to Crawford: Exploring the onset of synchronization in populations of coupled oscillators. *Physica D: Nonlinear Phenomena*, 143(1):1–20, 2000.
- [70] L. Mendelowitz, A. Verdugo, and R. Rand. Dynamics of three coupled limit cycle oscillators with application to artificial intelligence. *Communications in Nonlinear Science and Numerical Simulation*, 14(1):270–283, 2009.
- [71] Y. Fang, C. N. Gnegy, T. Shibata, D. Dash, D. M. Chiarulli, and S. P. Levitan. Non-boolean associative processing: circuits, system architecture, and algorithms. *IEEE Journal on Exploratory Solid-State Computational Devices and Circuits*, 1(1):94–102, 2015.
- [72] F. C. Hoppensteadt and E. M. Izhikevich. Synchronization of MEMS resonators and mechanical neurocomputing. *IEEE Transactions on Circuits and Systems I: Fundamental Theory and Applications*, 48(2):133–138, 2001.
- [73] D. E. Nikonov, I. A. Young, and G. I. Bourianoff. Convolutional networks for image processing by coupled oscillator arrays. *arXiv preprint arXiv:1409.4469*, 2014.
- [74] D. E. Nikonov, G. Csaba, W. Porod, T. Shibata, D. Voils, D. Hammerstrom, I. A. Young, and G. I. Bourianoff. Coupled-oscillator associative memory array operation for pattern recognition. *IEEE Journal on Exploratory Solid-State Computational Devices and Circuits*, 1(1):85–93, 2015.
- [75] L. Gao, P.-Y. Chen, and S. Yu. NbOx based oscillation neuron for neuromorphic computing. *Applied Physics Letters*, 111(10):103503, 2017.
- [76] A. A. Sharma, J. A. Bain, and J. A. Weldon. Phase coupling and control of oxide-based oscillators for neuromorphic computing. *IEEE Journal on Exploratory Solid-State Computational Devices and Circuits*, 1(1):58–66, 2015.
- [77] J. Torrejon, M. Riou, F. A. Araujo, S. Tsunegi, G. Khalsa, D. Querlioz, P. Bortolotti, V. Cros, K. Yakushiji, and A. Fukushima. Neuromorphic computing with nanoscale spintronic oscillators. *Nature*, 547(7664):428–431, 2017.
- [78] M. Itoh and L. O. Chua. Memristor oscillators. *International Journal of Bifurcation and Chaos*, 18(11):3183–3206, 2008.
- [79] G. B. Arfken and H.-J. Weber. *Mathematical methods for physicists*. Boston Elsevier, 6th ed. edition, 2005.
- [80] J. B. Chang, V. Liu, V. Subramanian, K. Sivula, C. Luscombe, A. Murphy, J. Liu, and J. Frechet. Printable polythiophene gas sensor array for low-cost electronic noses. *Journal of Applied Physics*, 100(1):014506, 2006.

- [81] H. C. Hao, K. T. Tang, P. H. Ku, J. S. Chao, C. H. Li, C. M. Yang, and D. J. Yao. Development of a portable electronic nose based on chemical surface acoustic wave array with multiplexed oscillator and readout electronics. *Sensors and Actuators B: Chemical*, 146(2):545–553, 2010.
- [82] H. S. Wasisto, S. Merzsch, A. Waag, E. Uhde, T. Salthammer, and E. Peiner. Airborne engineered nanoparticle mass sensor based on a silicon resonant cantilever. *Sensors and Actuators B: Chemical*, 180(1):77–89, 2013.
- [83] F. Tsow, E. Forzani, A. Rai, R. Wang, R. Tsui, S. Mastroianni, C. Knobbe, A. J. Gandolfi, and N. J. Tao. A wearable and wireless sensor system for real-time monitoring of toxic environmental volatile organic compounds. *IEEE Sensors Journal*, 9(12):1734–1740, 2009.
- [84] M. D. Valdes, I. Villares, J. Farina, and M. J. Moure. A FPGA-based frequency measurement system for high-accuracy QCM sensors. In *2008 34th Annual Conference of IEEE Industrial Electronics*, pages 1707–1712, 2008.
- [85] F. Aydemir and M. A. Ebeoğlu. A QCM sensor array-based electronic tongue with the optimized oscillator circuit using FPGA. *IEEE Transactions on Instrumentation and Measurement*, 67(2):431–438, 2017.
- [86] B. E. DeMartini, J. F. Rhoads, S. W. Shaw, and K. L. Turner. A single input–single output mass sensor based on a coupled array of microresonators. *Sensors and Actuators A: Physical*, 137(1):147–156, 2007.
- [87] A. Bietsch, J. Zhang, M. Hegner, H. P. Lang, and C. Gerber. Rapid functionalization of cantilever array sensors by inkjet printing. *Nanotechnology*, 15(8):873–880, 2004.
- [88] K. S. Van Dyke. The piezo-electric resonator and its equivalent network. *Proceedings of the Institute of Radio Engineers*, 16(6):742–764, 1928.
- [89] A. Khitun, G. Liu, and A. A. Balandin. Two-dimensional oscillatory neural network based on room-temperature charge-density-wave devices. *IEEE Transactions on Nanotechnology*, 16(5):860–867, 2017.
- [90] G. Dion, S. Mejaouri, and J. Sylvestre. Reservoir computing with a single delay-coupled non-linear mechanical oscillator. *Journal of Applied Physics*, 124(15):152132, 2018.
- [91] A. Velichko, M. Belyaev, V. Putrolaynen, and P. Boriskov. A new method of the pattern storage and recognition in oscillatory neural networks based on resistive switches. *Electronics*, 7(10):266, 2018.
- [92] F. C. Hoppensteadt and E. M. Izhikevich. Pattern recognition via synchronization in phase-locked loop neural networks. *IEEE Transactions on Neural Networks*, 11(3):734–738, 2000.
- [93] F. C. Hoppensteadt and E. M. Izhikevich. Oscillatory neurocomputers with dynamic connectivity. *Physical Review Letters*, 82(14):2983–2986, 1999.
- [94] A. Kumar and P. Mohanty. Autoassociative memory and pattern recognition in micromechanical oscillator network. *Scientific Reports*, 7(1):411, 2017.

- [95] D. Vodenicarevic, N. Locatelli, F. Abreu Araujo, J. Grollier, and D. Querlioz. A nanotechnology-ready computing scheme based on a weakly coupled oscillator network. *Scientific Reports*, 7(1):44772, 2017.
- [96] S. Tsunegi, T. Taniguchi, R. Lebrun, K. Yakushiji, V. Cros, J. Grollier, A. Fukushima, S. Yuasa, and H. Kubota. Scaling up electrically synchronized spin torque oscillator networks. *Scientific Reports*, 8(1):13475, 2018.
- [97] D. Miller, A. Blaikie, and B. J. Alemán. Nonvolatile rewritable frequency tuning of a nanoelectromechanical resonator using photoinduced doping. *Nano Letters*, 20(4):2378–2386, 2020.
- [98] S. T. Habermehl, N. Bajaj, S. Y. Shah, D. D. Quinn, D. Weinstein, and J. F. Rhoads. Synchronization in a network of coupled MEMS-Colpitts oscillators. *Nonlinear Dynamics*, 98(4):3037–3050, 2019.
- [99] B. W. Bahr, L. C. Popa, and D. Weinstein. 16.8 1GHz GaN-MMIC monolithically integrated MEMS-based oscillators. In *2015 IEEE International Solid-State Circuits Conference Digest of Technical Papers*, pages 1–3, 2015.
- [100] D. Fan, S. Maji, K. Yogendra, M. Sharad, and K. Roy. Injection-locked spin hall-induced coupled-oscillators for energy efficient associative computing. *IEEE Transactions on Nanotechnology*, 14(6):1083–1093, 2015.
- [101] H. Statz, P. Newman, I. W. Smith, R. A. Pucel, and H. A. Haus. GaAs FET device and circuit simulation in SPICE. *IEEE Transactions on Electron Devices*, 34(2):160–169, 1987.